Creep Resistance of Directionally Solidified Eutectic Ceramics: Experiments and Model

by

Jin Yi

B.S. Material Science and Engineering
University of Science and Technology Beijing, 1993
S.M. Material Science and Engineering
University of Science and Technology Beijing, 1999

Submitted to the Department of Mechanical Engineering
in partial fulfillment of the requirements for the degree of

Doctor of Philosophy

at the

MASSACHUSETTS INSTITUTE OF TECHNOLOGY

June 2004

Author .....
Department of Mechanical Engineering
May 18, 2004

Certified by .....
Ali S. Argon
Professor
Thesis Supervisor

Accepted by .....
Ain A. Sonin
Chairman, Department Committee on Graduate Students

Creep Resistance of Directionally Solidified Eutectic Ceramics: Experiments and Model

by

Jin Yi

Submitted to the Department of Mechanical Engineering
on May 18, 2004, in partial fulfillment of the
requirements for the degree of
Doctor of Philosophy

Abstract

The creep resistance of the directionally solidified eutectic ceramic of Al_2O_3/c-$ZrO_2(Y_2O_3)$ was studied in the temperature range of 1200-1520°C both exprimentally and by the mechanistic dislocation model. The topologically continuous majority phase of Al_2O_3 has a nearly perfect growth texture in the [0001] direction and encapsulates the minority c-$ZrO_2(Y_2O_3)$ phase in a variety of morphologies. This encapsulated minority phase, too, has a close to $< 110 >$ growth texture, regardless of morphology. The two phases are separated by well-structured interfaces.

The tensile creep of the eutectic in its growth direction exhibits an initial transient that is attributed to stress relaxation in the c-$ZrO_2(Y_2O_3)$ phase, but otherwise in steady state shows many of the same characteristics of creep in sapphire single crystals with c-axis orientation. The creep strain rate of the eutectic has stress exponents in the range of 4.5~5.0 and a temperature dependence suggesting a rate mechanism governed by oxygen ion diffusion in the Al_2O_3. Since the deformation is isolated in each phase and glide in any available slip systems is not possible, the recorded creep strain is derived from the diffusion-controlled climb of pyramidal edge dislocations in the Al_2O_3 phase, which is supported by TEM observations. The evidence suggests that the climbing dislocations in Al_2O_3 must repeatedly circumvent the c-$ZrO_2(Y_2O_3)$ domains acting as dispersoids, resulting in the stress exponents larger than 3. The mechanistic dislocation creep model is in very good agreement with the experiments. Low angel boundaries in the form of asymmetrical tilt boundaries are found between columnar colonies in the crept specimens. These could have formed by the reaction of basal dislocations and pyramidal dislocations, but generally were thought to result from aggregation of climbing pyramidal edge dislocations. The various possibilities of dislocation sources in Al_2O_3 are also discussed.

Thesis Supervisor: Ali S. Argon
Title: Professor

Acknowledgments

The years at MIT pursuing my doctorial degree have been a very challenging and rewarding experience. During these years, many have guided and helped me to overcome many obstacles to finish this thesis. I realize that my appreciation to those people can hardly be expressed in such a short acknowledgement.

With my sincere gratitude, I would like to thank Professor Ali S. Argon who has been my advisor and mentor for the past five years. His academic vision and knowledge have not only supported me through those years of long research "incubation" period, but also stimulated and guided me to many new aspects in materials and mechanics.

My appreciation also goes to Professor David M. Parks and Professor Yet-Ming Chiang for serving on my committee, and for providing valuable comments and insights on my research. I would like to acknowledge Professor John B. Vander Sande for his inspiring guidance on my TEM experiments, Dr. Ali Sayir at NASA John Glenn Research Center for his help on fabricating materials and research collaboration, Professor Arthur Heuer and Professor K.P.D. Largelöf at Case Western Reserve University for providing very thoughtful comments in this research. I would also like to thank Professor Mary Boyce, Professor Lallit Anand and Professor Simona Socrate for their advices.

I would like to acknowledge the financial supports from AFOSR, MIT Graduate Student Fellowship Program, and MIT Mechanics and Materials group of the Mechanical Engineering Department.

I am grateful to my colleagues at Mechanics and Materials Group, Gu, Tom, Yu, Steve, Heather, Mats, Ethan, Hang, Raj, Nici, Jeremy, Nuo, Franco, Ekrem, Ted, Mohit, Chris, Cheng, Yujie, Regina, Mike, Petch, Suvrat, Adam, Anastassia, Scott, Vaibhaw, Dora, Yin, Anu, Melis, Kristen. I shall thank them all for warm friendship which made my stay at MIT a cherishing and memorable one, and for fruitful discussions and help. I am also very grateful to Una, Ray and Leslie for their generous supports, and more than that, being so

friendly to me and all of my fellow graduate students.

I am deeply indebted to my parents who raised me and led me to be in love with science, and my wife, Yue, who provided endless support and love during my journey at MIT. I would like to dedicate this thesis to them.

Contents

List of Figures

List of Tables

Chapter 1

Introduction

In high temperature structural applications, such as gas turbines and rocket engines, the creep resistance remains as the primary screening property for selecting proper structural materials. Currently structural materials in high temperature service, such as single crystal superalloys in γ/γ' form, have a service limit of around 1000°C.

As Fleischer [1987] noted, presented in Fig 1-1, to reach beyond the capabilities of the present set of high-temperature superalloys and some intermetallic compounds, it is necessary to consider other compounds such as oxides, carbides, borides, etc. to reach service temperatures in the 1400-1600°C range. In this temperature range, especially for those applications in open air working environment, oxidation resistance becomes another key criterion. Oxides are the natural choice for their chemical stability in oxidation environment.

For some time single crystal sapphire fiber with [0001] axis orientation has been considered as an ideal material for high temperature application (Sayir and Farmer [2000]). In that orientation, with its principal basal and prismatic systems unstressed, sapphire single crystal fibers have remarkable creep resistance in the 1400-1600°C temperature range, where only the pyramidal slip system is stressed. Early experiments of Firestone and Heuer [1976] on [0001] axis-oriented-sapphire in the 1600-1800°C range produced evidence that

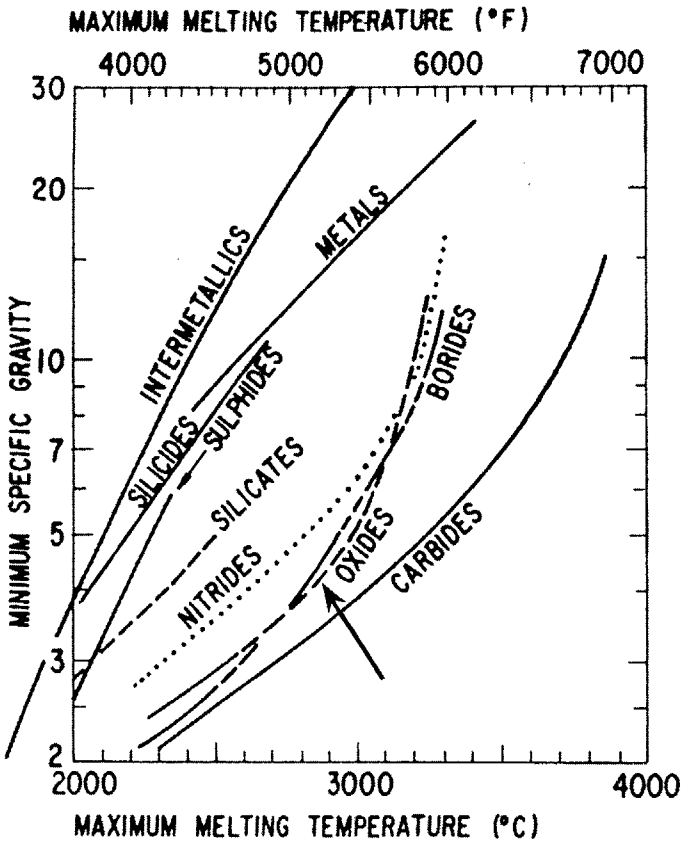

Figure 1-1: Density vs. melting temperature for various binary compounds. (Fleischer [1987])

such sapphire crystals creep entirely by the climb of the $1/3< \bar{1}101 >$ pyramidal edge dislocations, with no slip line or stereo-TEM evidence of glide of such dislocations on any of the possible pyramidal planes available. Those such dislocations are entirely sessile in glide has now been established in very recent MD simulations of the core structures of these dislocations (Chang *et al.* [2003], Bodur *et al.* [2004]). The stress dependence of the creep rates of [0001] oriented sapphire crystals and their governing activation energy of oxygen ion diffusion in Al_2O_3 have all been consistent with a pure climb mode of creep (Firestone and Heuer [1976]). This is extremely rare in the creep of metals, with the only similar occurrence having been reported by Edelin and Poirier [1973] in similarly oriented Mg crystals.

While oriented sapphire single crystal fibers have advantageous characteristies and have been considered with diffusion barrier coatings as reinforcing elements in polycrystalline Al_2O_3 matrixes for composite applications (Morgan and Marshall [1995], Lev and Argon [1995]), the practice has been costly and lacked flexibility. As an alternative to sapphire-fiber-reinforced ceramic composites, a series of directionally solidified ceramic eutectics, consisting largely of an Al_2O_3 component together with compatible stable oxides of ZrO_2 or YAG combine many of the advantages of sapphire fiber with morphological stability at elevated temperatures and relative ease of production. Of these the Al_2O_3-ZrO_2 system eutectic, with additional Y_2O_3 modification to create cubic ZrO_2, has received considerable attention (Sayir [1998]). This eutectic has demonstrated some attractive characteristics. In the Laser Heated Float Zone (LHFZ)-produced eutectic in the form of fibers or slender rods, the Al_2O_3/c-$ZrO_2(Y_2O_3)$[1] eutectics possess a sub-micron scale morphology in which the majority Al_2O_3 phase maintains a topologically continuous form with a remarkably tight [0001] growth texture (Fraser *et al.* [2001]). The c-ZrO_2 phase, in turn, in various morphological shapes ranging from aligned fibers or platelets in either well organized colonies or in less well ordered forms, usually has one narrow dimension in the 0.2μm range, and is

[1]It is noted in this thesis that about 4.2mol% of Y_2O_3 is required to form cubic zirconia in Al_2O_3-ZrO_2 eutectic system. Hereafter, cubic zirconia is referred as c-ZrO_2.

always fully encapsulated in the Al_2O_3 phase. This eutectic has fairly reproducible and reasonably attractive levels of fracture toughness (Pastor *et al.* [2001]) and possesses high quality, nearly coherent interfaces (Mazerolles *et al.* [1986]).

The eutectics contain significant levels of residual stress at room temperature, resulting from thermal misfit between the component phases. The Al_2O_3 was found to be in a state uniaxial tension parallel to the axis, at a level of 1.0 GPa, while the c-ZrO_2 was in some form of multiaxial compression, roughly at the same level (Dickey *et al.* [1999]). Such residual stresses that decrease in level at elevated temperatures could still be of importance in initial creep response (Dickey *et al.* [1999]) where they, however, should be rapidly relaxed with the onset of steady creep flow.

This thesis research is to examine the creep behavior of directionally solidified eutectic ceramic of Al_2O_3/c-ZrO_2 in the temperature range of 1200°C-1520°C under various levels of stress; and to identify the micro-mechanism of its high creep resistance by Transmission Electron Microscopy (TEM) observations along with a dislocation mechanistic model. Moreover, a general assessment of the fracture toughness of this eutectic material is necessary to be undertaken to complement its mechanical characteristics.

This thesis is organized in the following structure. A description of material fabrication and microstructure characterization of directionally solidified as-grown eutectic specimen are covered in Chapter 2. Chapter 3 and Chapter 4 report the creep experiment apparatus and creep behaviors of this eutectic material at high temperature under various levels of stress. The TEM observations of crept specimens are presented in Chapter 5. Based upon these experimental findings, a mechanistic dislocation model is discussed in detail in Chapter 6. Chapter 7 summarizes the defect chemistry of different types of doping and their influences on the diffusion process in sapphire (single crystal $\alpha-Al_2O_3$) and presents the corresponding creep experiments on sapphire. Its indication to improve the creep resistance of the eutectic material is discussed. Chapter 8 presents the fracture toughness evaluation of this eutectic material at room temperature and high temperature by applying several

different methodologies. Finally Chapter 9 summarizes the conclusions in the thesis.

Chapter 2

Directionally Solidified Eutectic Material: Al_2O_3/c-$ZrO_2(Y_2O_3)$

2.1 Material Fabrication

The eutectic Al_2O_3/c-$ZrO_2(Y_2O_3)$ have all been produced by the Laser Heated Float Zone (LHFZ) method at the NASA John Glenn Research Center. This process has been reported thoroughly by Sayir and Farmer [2000], Argon *et al.* [2001], and Yi *et al.* [2004b]. Source rods were prepared using 99.999% pure polycrystalline Al_2O_3 powder (CERAC/pure, Ceralox Corp., Tucson, AZ 08676). These powders were blended in acetone for 70 hours using high purity Y_2O_3 stabilized ZrO_2. The slurry was dried, mixed again and formed into cylindrical rods using cold isostatic pressing. These rods were then sintered at 1500°C in air for 4 hours. A laser heated float zone (LHFZ) process was used to produce the directional solidification of rods. The heating source was a coherent CO_2-laser beam (FH-1500-Carbon Dioxide Laser, PRC Corp., Landing, NJ 0785) split into four beams, 90° apart from each other. Each beam is focused onto the molten zone and converges at the top surface of a polycrystalline source rod located in the center of the processing chamber. These opposing beams are mechanically converted into opposing laser lines, and during

growth the source rod is moved vertically through the laser beam. The maximum available laser power is 600 W, but only a small fraction of this power was needed as the radiation from the CO_2-laser (wavelength=10.6 μm) is effectively absorbed in the oxides. The molten zone temperature was measured in the infrared radiation region with an Infrared Thermal Monitor (Vanzetti Systems, Stoughten, MA 02072) and the output was used to control the laser power. To initiate directional solidification of the eutectic, a seed of single crystal sapphire ($<$ 0001 $>$ direction) was lowered onto the molten liquid until wetting occurred. All growth experiments were conducted in air. Neither the seed crystal nor the source rod was rotated.

These rods were re-used as source rods to produce final samples. The objective of the second solidification was to minimize the entrapment of the gases at the liquid solid interface. The directional solidification rate was at 2mm/min for both processes. The directionally solidified rod had cross-sectional dimensions in the range of 1$\sim$1.5 mm in diameter, varying from rod to rod but showed only small thickness variations along their 200$\sim$220 mm length in any one rod. Some short rods with lengths of 70$\sim$80 mm and diameters of 0.5$\sim$0.8 mm were also grown initially with buttonhead ends to fit in an earlier design of specimen holder, as shown in Fig 2-1. Such forms of loading through button-head ends was generally unsuccessful and results in premature fractures.

2.2 Microstructure Characterization

The directionally solidified eutectic rods were composed of 67% Al_2O_3 and 33% c-ZrO_2 by volume. The typical as-grown microstructures, shown in Fig 2-2 and Fig 2-3, where the light phase, c-ZrO_2 and the dark phase, Al_2O_3, have well-defined columnar colony microstructure. Figure 2-4 on a lower magnification but with broader overview of the eutectic morphology on a transversal section of a rod shows clearly this colony structure in the interior of the rod. There is also a more plate-like morphology near the surfaces (Sayir and Farmer [2000],

Argon *et al.* [2001]). The micrographs also show that there are two forms of c-ZrO_2 different considerably in scale. In addition to the quite regular fine fibrillar structure of the c-ZrO_2 inside the colonies, there is a coarse scale component located in the colony borders having less regular shapes. The arrangements of the c-ZrO_2 fibrils in the colonies have a clear 3-fold symmetry which is a direct consequence of the stoichiometry of Al_2O_3 where in the alternating cation and anion layers normal to the c-axis only 2/3 of the sites in the cation layers are filled and the lattice of empty cation sites characterizes the basic basal 3-fold symmetry of the structure. Between the fiber colonies, the symmetry axes are relatively close to parallel to each other, with misalignments not exceeding $\pm 10^o$, as shown in Fig 2-4. The mean distance Λ in the Al_2O_3, between the c-ZrO_2 filaments or platelets that is of interest for mechanistic consideration in the model for creep resistance is typically between $0.5 \sim 2.0 \mu$m on the average.

A chemical composition analysis of an as-grown sample rod was conducted by Wavelength Dispersive Spectrometry (WDS) (JEOL JXA-733 Superprobes, JEOL). Fig 2-5 shows an area mapping of three different elements, Al, Zr and Y, along with its backscattering electron image. They prove that the light phase in Fig 2-2 is indeed c-ZrO_2, while the dark phase is Al_2O_3. There is also often a certain light-grey phase, which is identified as $Y_3Al_5O_{12}$(YAG) by the composition ratio, existing along the boundary of colonies. A large amount of YAG found in this analysis is due to a higher-than-necessary ratio of Y_2O_3 in the sample. In the samples with the correct Y_2O_3 doping level, the amount of YAG was insignificant.

An unavoidable level of porosity was found along the center line of many samples, often with substantial pore dimensions to constitute super-critical flaws for fracture. As shown in Fig 2-6 (a) and Fig 2-6 (b), these pores always had smooth surfaces indicating they resulted from inadequate wetting during melting and solidification of the initial charge. In some instances they resulted in premature fracture after the stress was applied during creep experiments, where these internal defects can be used to evaluate fracture toughness as

pre-existing critical cracks. This will be discussed in Chapter 8.

The crystallographic orientations of each phase were examined by x-ray diffraction. Fig 2-7 is an X-ray diffraction of the transversal section of the as-grown sample rod by Dickey [2001]. The diffraction on the transversal section shows that there is a strong concentration of (0001) planes parallel to the transversal section in the Al_2O_3 phase; while in the c-ZrO_2 phase, the major reflections are the same as the ones from a powder diffraction pattern of c-ZrO_2, which indicates that the c-ZrO_2 fibers have multiple orientations like a polycrsytal of c-ZrO_2 with a concentration on (110) planes. Another X-ray diffraction on the axial section of the as-grown sample rod, shown in Fig 2-8, gives a similar pattern of ZrO_2 without the (110) planes concentration; while the reflections of Al_2O_3 are from the prismatic plane of Al_2O_3 and have a single crystal character. Dickey [2002] has conducted a pole figure analysis on directionally solidified eutectic Al_2O_3/c-ZrO_2. It shows that Al_2O_3 has a strong texture of [0001] along the growth axis and c-ZrO_2 is highly [110] textured along the growth axis. These orientation evidences indicate that the topologically continuous majority phase of Al_2O_3 has a nearly perfect growth texture in the [0001] direction and encapsulates the minority c-$ZrO_2(Y_2O_3)$ phase in a variety of morphologies which has a close to $< 110 >$ growth texture, regardless of morphology.

Transmission Electron Microscopy (TEM) specimens from randomly spaced axial and transverse sections were made for conducting electron diffractions to examine the phase orientation relationship. Fig 2-9 gives the phase relationship between Al_2O_3 and c-ZrO_2 in both axial and transversal sections. The electron diffraction patterns show strong $[0001]_{Al_2O_3}//[11\bar{2}]_{c-ZrO_2}$ and $[2\bar{1}\bar{1}0]_{Al_2O_3}//[011]_{c-ZrO_2}$ reflections. High resolution direct lattice images shown in Fig. 2-10 also indicate a relationship in $[0001]_{Al_2O_3}//[110]_{c-ZrO_2}$ and $[1\bar{1}00]_{Al_2O_3}//[100]_{c-ZrO_2}$. Michel *et al.* [1984] and Mazerolles *et al.* [1986] have reported same phase orientation relationship. Sayir [1998] found another phase orientation relationship, $[0001]_{Al_2O_3}//[111]_{c-ZrO_2}$ and $[1\bar{1}00]_{Al_2O_3}//[110]_{c-ZrO_2}$. These phase orientation relationships with corresponding ideal lattice plane distances are summarized in Table

2.1. Considering only the crystal plane matching to minimize the corresponding plane distortion, all these pairs are possible to form semi-coherent phase boundary.

Planar interfaces and curved interfaces can be observed between Al_2O_3 phase and c-ZrO_2 phase. Extensive observations by TEM indicate that the interface boundary thickness is in the order of fractions of nanometer or less (a few atomic distances). It should be kept in mind that these boundaries are viewed in projection, and consequently the actual thickness of the interface might not be the thickness viewed under TEM micrograph. Two direct lattice imaging observations, of Fig 2-10, obtained from transversal and axial sections, show a typical interface that are semicoherent and atomically narrow. Incoherent phase boundary, such as shown in Fig 2-11 also exists in this eutectic material.

Table 2.1: Phase orientation relationship reported by various investigators

Research Group	Orientation Relationship	Shortest Plane Distance[a] (Å)
Present Research	$[0001]_{Al_2O_3}//[11\bar{2}]_{c-ZrO_2}$	$2.17_{Al_2O_3}//6.29_{ZrO_2}$
	$[2\bar{1}\bar{1}0]_{Al_2O_3}//[011]_{c-ZrO_2}$	$4.76_{Al_2O_3}//3.63_{ZrO_2}$
	and	
	$[0001]_{Al_2O_3}//[110]_{c-ZrO_2}$	$2.17_{Al_2O_3}//3.63_{ZrO_2}$
	$[1\bar{1}00]_{Al_2O_3}//[100]_{c-ZrO_2}$	$2.74_{Al_2O_3}//5.14_{ZrO_2}$
Mazerolles *et al.* [1986] and Michel *et al.* [1984]	$[0001]_{Al_2O_3}//[010]_{c-ZrO_2}$	$2.17_{Al_2O_3}//5.14_{ZrO_2}$
	$[1\bar{1}00]_{Al_2O_3}//[100]_{c-ZrO_2}$	$2.74_{Al_2O_3}//5.14_{ZrO_2}$
	and	
	$[0001]_{Al_2O_3}//[110]_{c-ZrO_2}$	$2.17_{Al_2O_3}//3.63_{ZrO_2}$
	$[1\bar{1}00]_{Al_2O_3}//[001]_{c-ZrO_2}$	$2.74_{Al_2O_3}//5.14_{ZrO_2}$
Sayir [1998]	$[0001]_{Al_2O_3}//[111]_{c-ZrO_2}$	$2.17_{Al_2O_3}//8.90_{ZrO_2}$
	$[1\bar{1}00]_{Al_2O_3}//[110]_{c-ZrO_2}$	$2.74_{Al_2O_3}//3.63_{ZrO_2}$

[a]The shortest plane distances of Al_2O_3 are calculated based on the ideal lattice unit cell structure by Kronberg [1957].

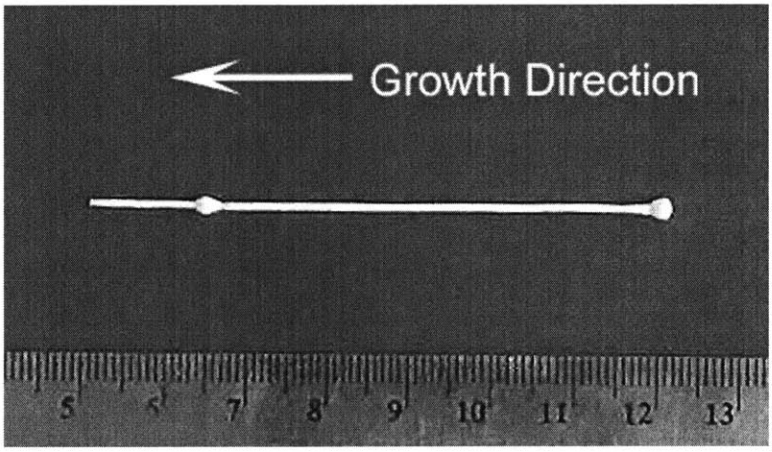

Figure 2-1: An as-grown directionally solidified eutectic Al_2O_3/c-ZrO_2 specimen fabricated by LHFZ, with two buttonhead ends.

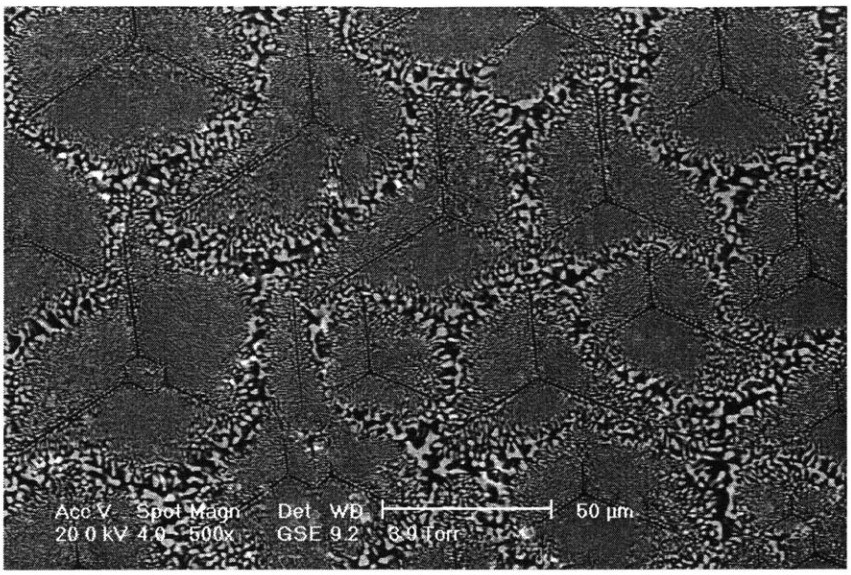

(a)

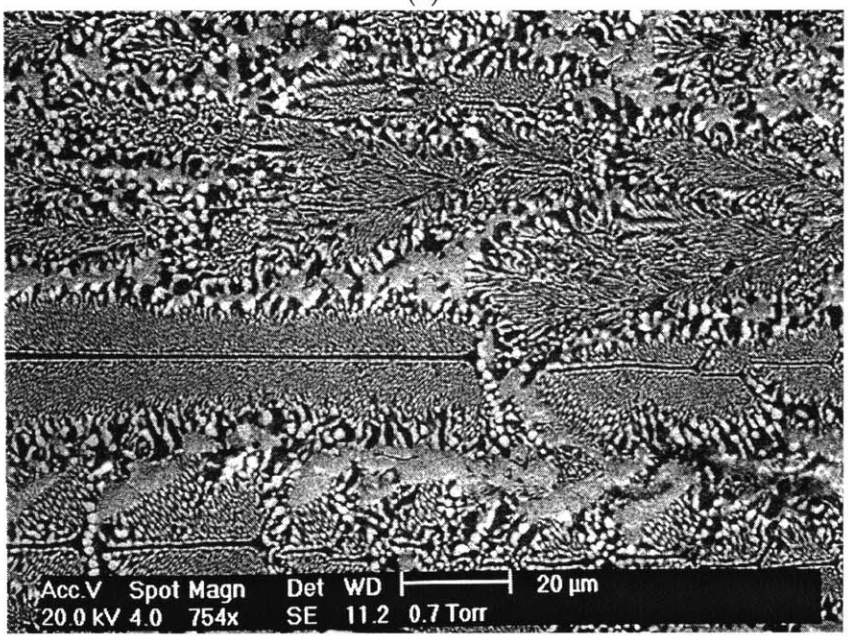

(b)

Figure 2-2: A typical microstructure of Al_2O_3/c-$ZrO_2(Y_2O_3)$ eutectic, (a) transversal section (b) axial section.

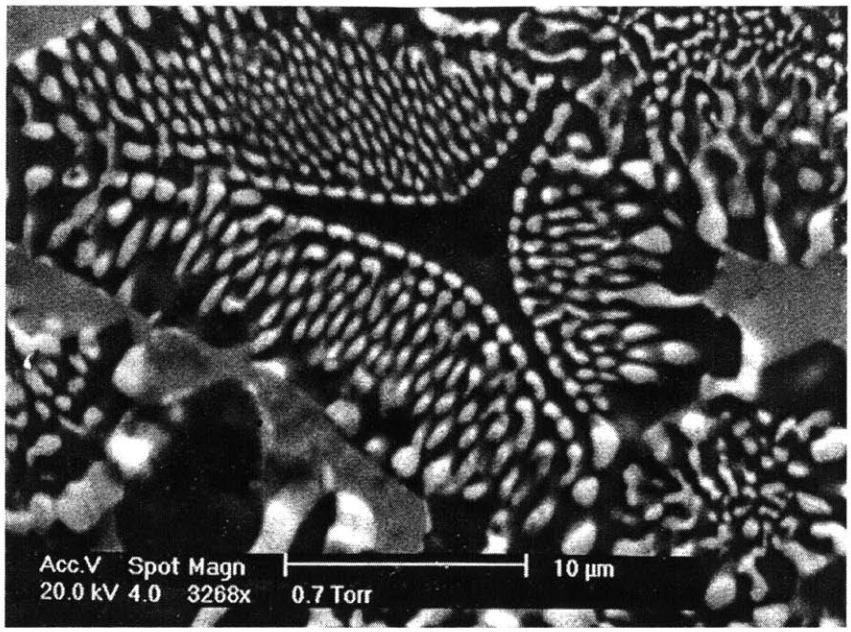

(a)

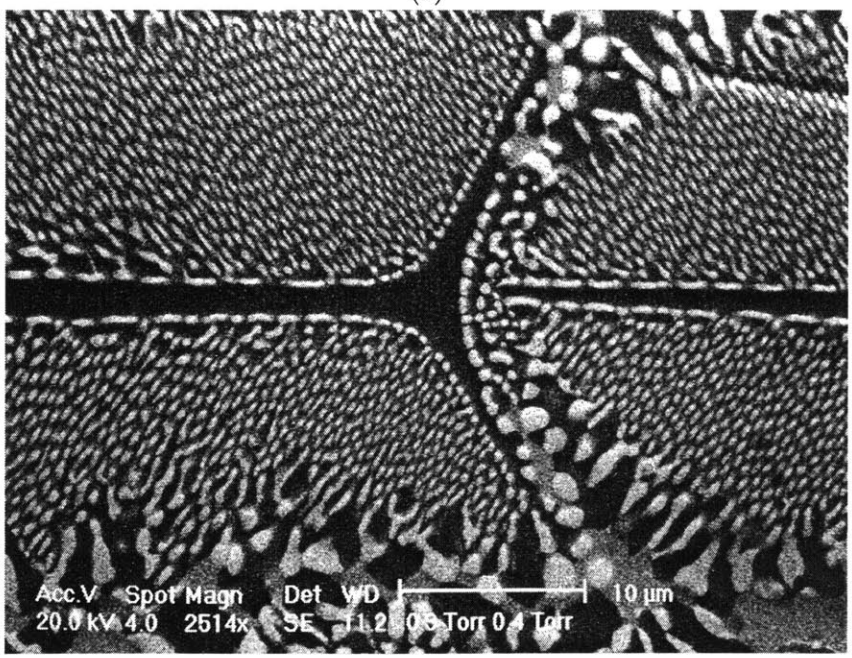

(b)

Figure 2-3: A higher resolution view of typical microstructure of Al_2O_3/c-$ZrO_2(Y_2O_3)$ eutectic, (a) transversal section (b) axial section.

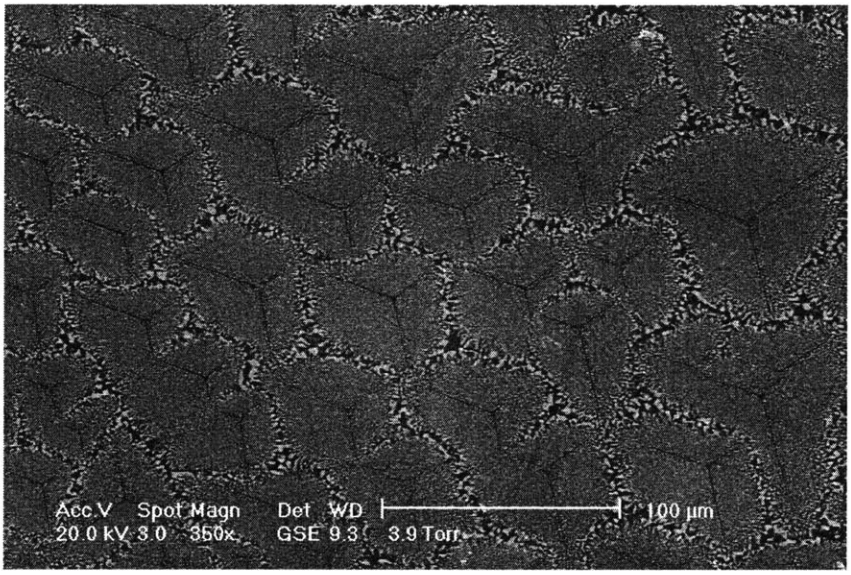

Figure 2-4: A lower magnification but with broader overview of the eutectic morphology on a transversal section of a rod shows clearly the columnar colony structures in the interior of the rod.

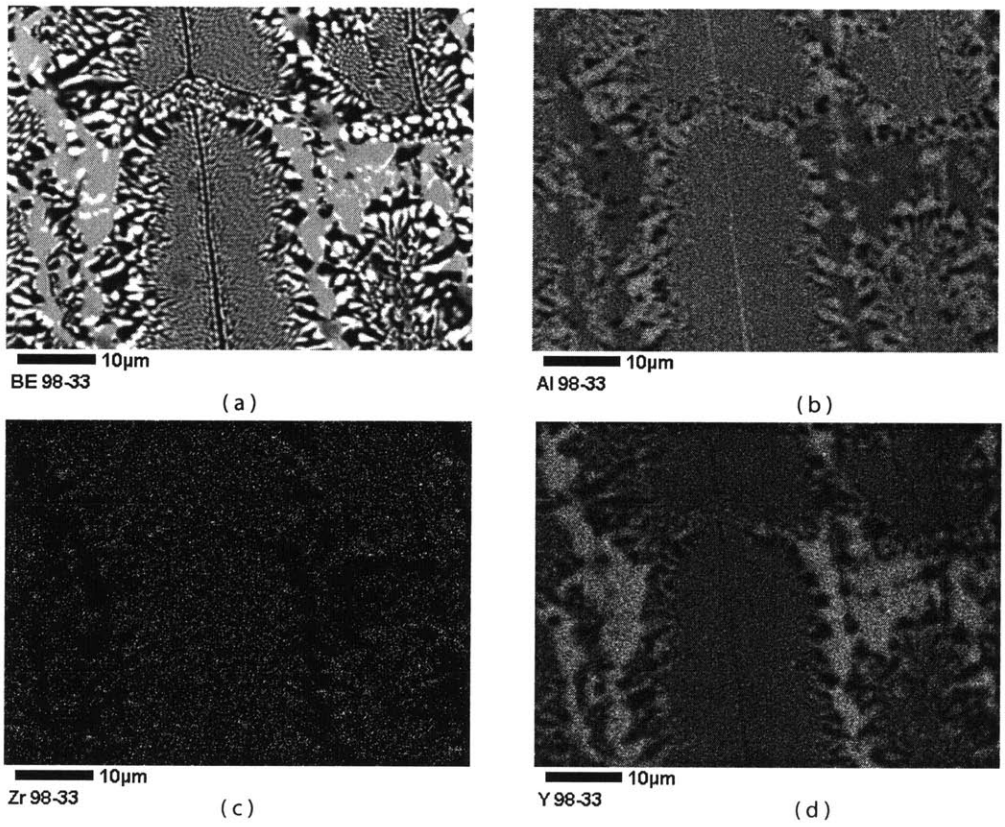

Figure 2-5: Element mapping by WDS (Wavelength Dispersive Spectrometry) of a transversal section of Al_2O_3/c-$ZrO_2(Y_2O_3)$ eutectic, (a) Backscattering electron image (b) Al element area mapping (c) Zr element area mapping (d) Y element area mapping.

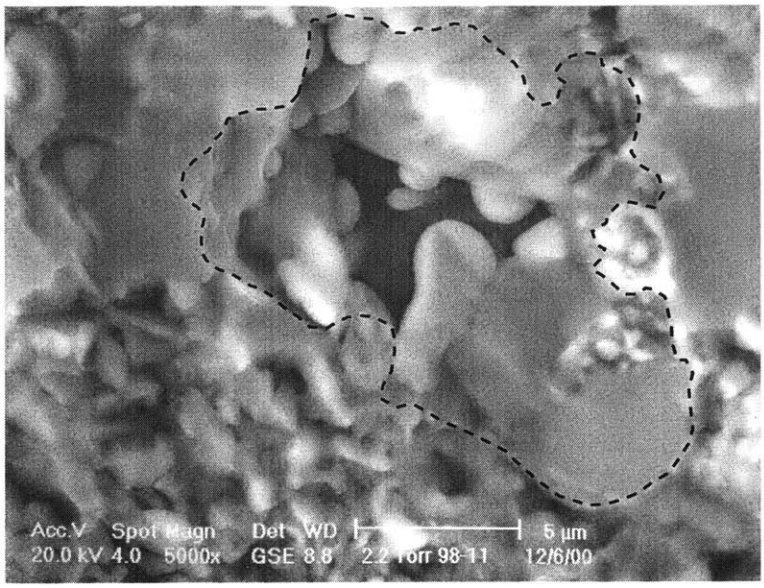

(a)

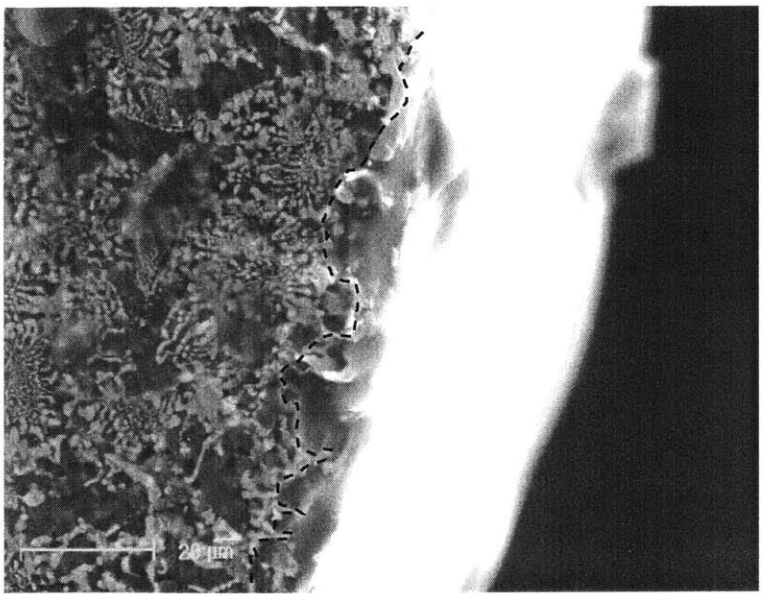

(b)

Figure 2-6: Growth pores in directionally solidified eutectic Al_2O_3/c-$ZrO_2(Y_2O_3)$ at (a) interior (b) surface.

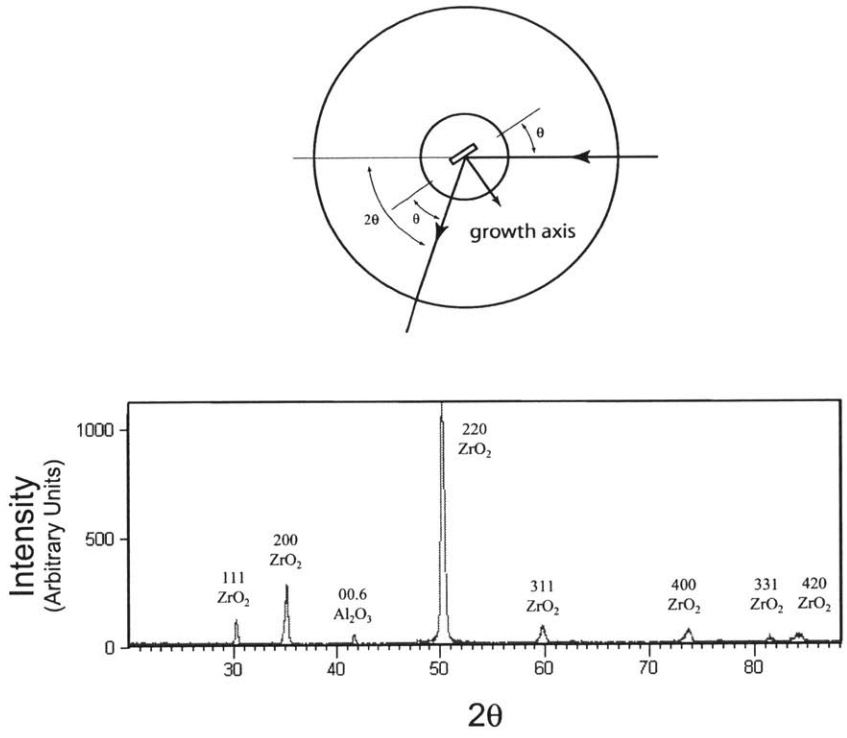

Figure 2-7: X-ray diffraction of transversal section of directionally solidified eutectic Al_2O_3/c-$ZrO_2(Y_2O_3)$. (Dickey [2001])

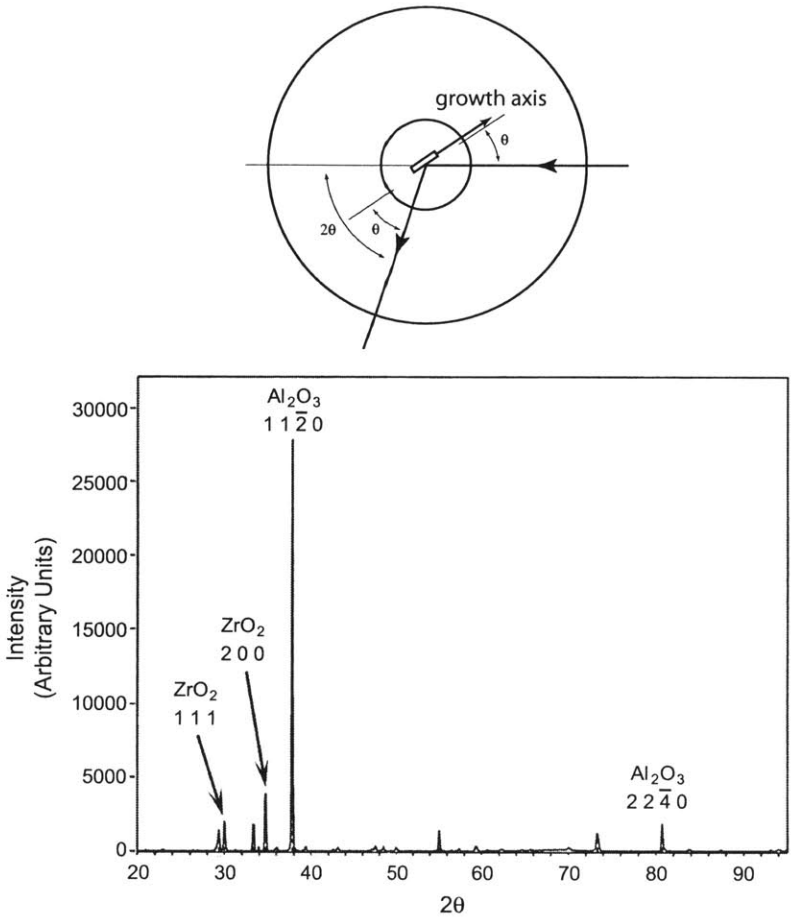

Figure 2-8: X-ray diffraction of axial section of directionally solidified eutectic Al_2O_3/c-$ZrO_2(Y_2O_3)$.

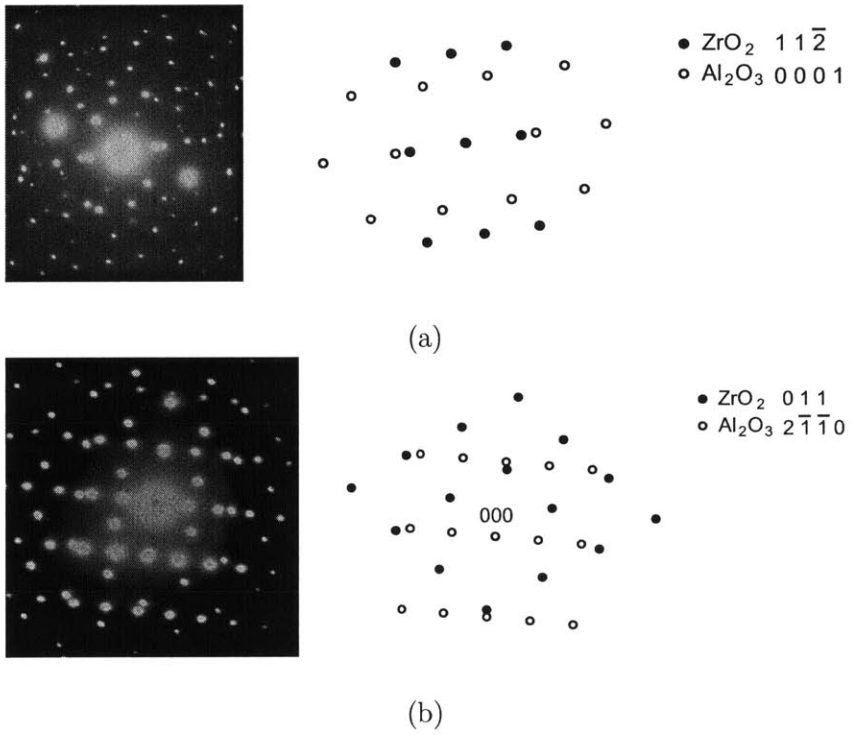

Figure 2-9: Phase orientation relationship by electron diffraction of Al_2O_3/c-$ZrO_2(Y_2O_3)$ (a) transversal section (b) axial section.

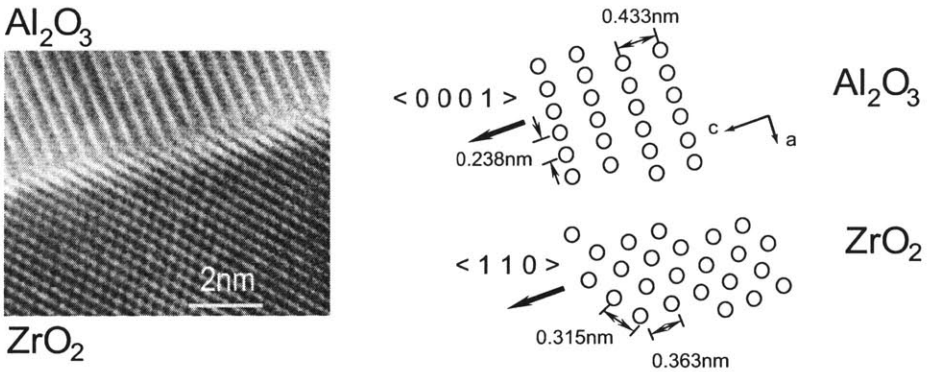

(a)

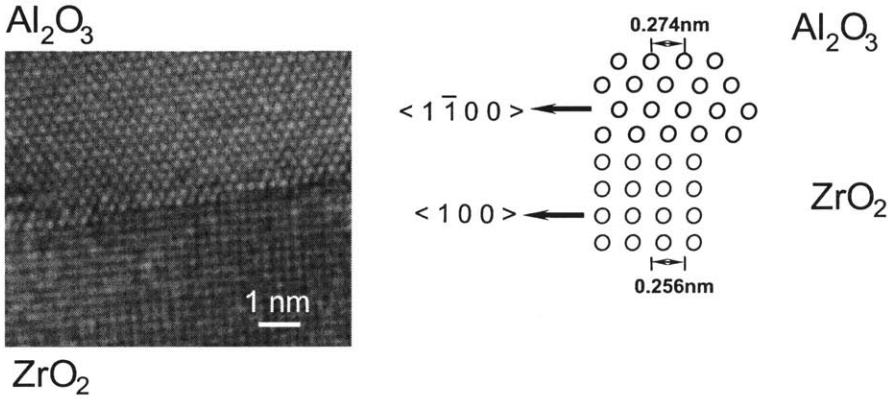

(b)

Figure 2-10: An incoherent interface between Al_2O_3 and c-ZrO_2 in an Al_2O_3/c-ZrO_2(Y_2O_3) eutectic. (a) axial section (b) transversal section.

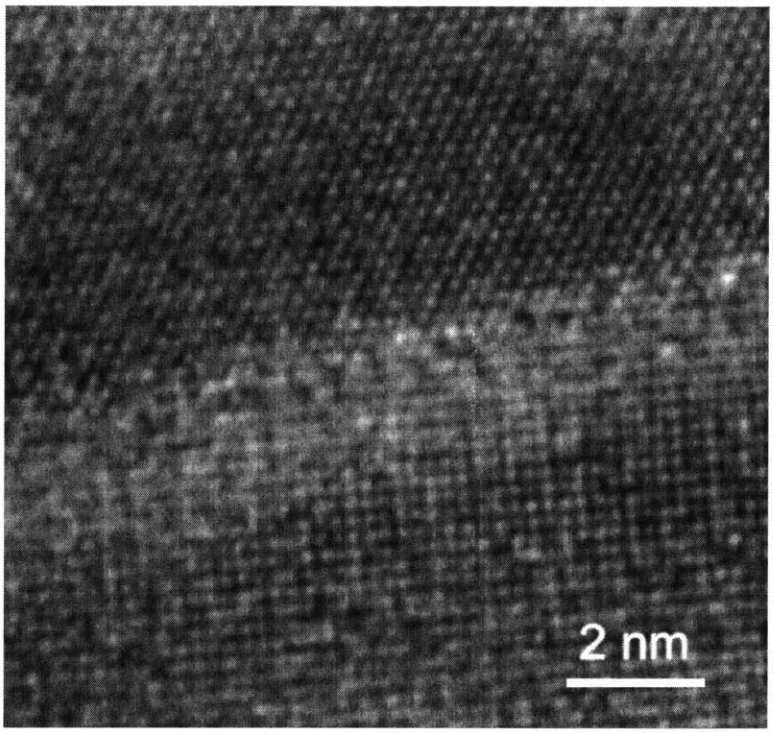

Figure 2-11: A direct lattice image of a typical interface between Al_2O_3 and c-ZrO_2 in an Al_2O_3/c-ZrO_2(Y_2O_3) eutectic shows an incoherent phase boundary.

Chapter 3

Tensile Creep Experiments

3.1 Tensile Creep Specimens

Creep specimen rods directionally solidified by LHFZ in this research had cross-sectional dimensions ranging from 1.0 mm to 2.0 mm from rod to rod but showed only small diameter variations along their 200~220 mm length in any one rod. An earlier version of specimens with buttonhead ends were of 80~100 mm in length and had diameters ranging from 0.5~0.8 mm. These specimens were all used in as-grown condition, without any surface grinding or other means of surface preparation and without any further heat treatment.

3.2 Tensile Creep Apparatus

The creep experiments were carried out in tension in a lever-loaded creep testing machine with a high temperature Centorr vacuum chamber (Centorr Vacuum Industries, Nashua, NH 03062), as shown in Fig 3-1. The load was smoothly applied by initially supporting the dead weight loads with a hydraulic jack. After reaching the desired test temperature, the jack was slowly lowered until the load was fully applied, in a time period of about 15 seconds. All the creep tests were conducted under constant load mode. Since very small creep strains (not exceeding 1%) were expected the conditions amounted to constant stress.

The vacuum was maintained at a pressure in the order of 10^{-6} torr (1 torr = 1.333224 millibar = 133.3224 Pa) for the purpose of protecting Ta or W heating elements.

There were two different types of heating zone design used in the research, which are referred here as test Configuration A and test Configuration B.

For test Configuration A, the furnace was equipped with a normal full-length W mesh heating element produced by Centorr Vacuum Industries, Nashua, NH. The eutectic specimens with buttonhead ends were mounted in slotted TZM grips. The upper and lower grips were then screwed on water-cooled upper and lower connecting bars of the load train, respectively. The TZM grips were surrounded by two layers of platinum radiation shield with a gap separating the two layers and the most inner layer from the grips. Considering the high-vacuum nature in the testing chamber and the low thermal conductivity of specimen rod, the heat transfer from heating element to the specimen is dominated by thermal radiation. Therefore, the water-cooling connecting bar to the grips and radiation shields were able to create a reasonable large thermal gradient along the specimen rod within the gripping portion. The creep deformation was then concentrated on the portion of specimen which is directly exposed to the heating element. Figure 3-2 gives a schematic drawing of test Configuration A.

For test Configuration B, the furnace was equipped with a specially designed heating zone, shown in Fig 3-3, of 50 mm in diameter and 58 mm in length made up of a split cylindrical configuration of a 1 mm thick Ta sheet with alternating up-and-down slits to increase the path length of the heating element. The heating zone was surrounded by a series of Mo radiation shields with gaps separating layers. The long specimens (200~220 mm in length) threaded through the heating zone and were gripped at their ends by metallic friction grips which had a hinge mechanism to accommodate the uneven shape of the as-grown rod, clamping down on the ends of the specimens through annealed soft nickel sheets to avoid high local contact forces on the rods that could have resulted in fracture. The metallic friction grips were then connected by universal joints to the water-cooled upper

and lower connecting bars of the load train, respectively. Two relatively massive water cooled OFHC *Cu* plates were placed between the two exits of the heating zone and the specimen grips to assure that the gripping conditions were, as much as possible, at low temperature not to exceed about 200°C to avoid slippage caused by thermal expansion in the grips. Since the temperature of the specimen inside the heating zone was higher by ~1200-1300°C above the portions of the sample outside the heating zone and the openings on the radiation shields through which the specimen rod threaded is fairly small, less than 4 mm, the gauge length was taken as the axial extent of the heating zone.

It has been proved that the test Configuration B was able to tolerate the misalignment caused by the loading train and the non-uniform shape of as-grown specimens very effectively. Because of the brittle nature of this eutectic material, test Configuration B was the one used in most of the creep experiments in this research. Although Configuration A and B had different gripping mechanisms, the creep deformation was concentrated in the gauge section and temperature distribution along the gauge section was uniform in both configurations. Therefore, the creep results generated from both configurations are not distinguished here.

An optical grade quartz window on the front side of vacuum chamber permitted viewing the hot specimen through a narrow axial slit in the heating elements to allow direct measurements of the specimen temperature by means of a two-wave-length pyrometer (from Omega Vanzetti, Sharon, MA.), providing emissivity-independent measurements. In addition to a control thermocouple inside the heating zone, another thermocouple placed close to the specimen without physically touching it was used to actually record the steady temperature in the thermal cavity. The temperature measured by this second thermocouple and that measured by the pyrometer on the specimen usually agreed quite well. The heating zone temperature was automatically controlled by a PID controller of the Centorr equipment.

Since the steady state creep extensions of the specimens under stress were generally quite small, to eliminate random flexures and motions of the massive creep frame from influencing

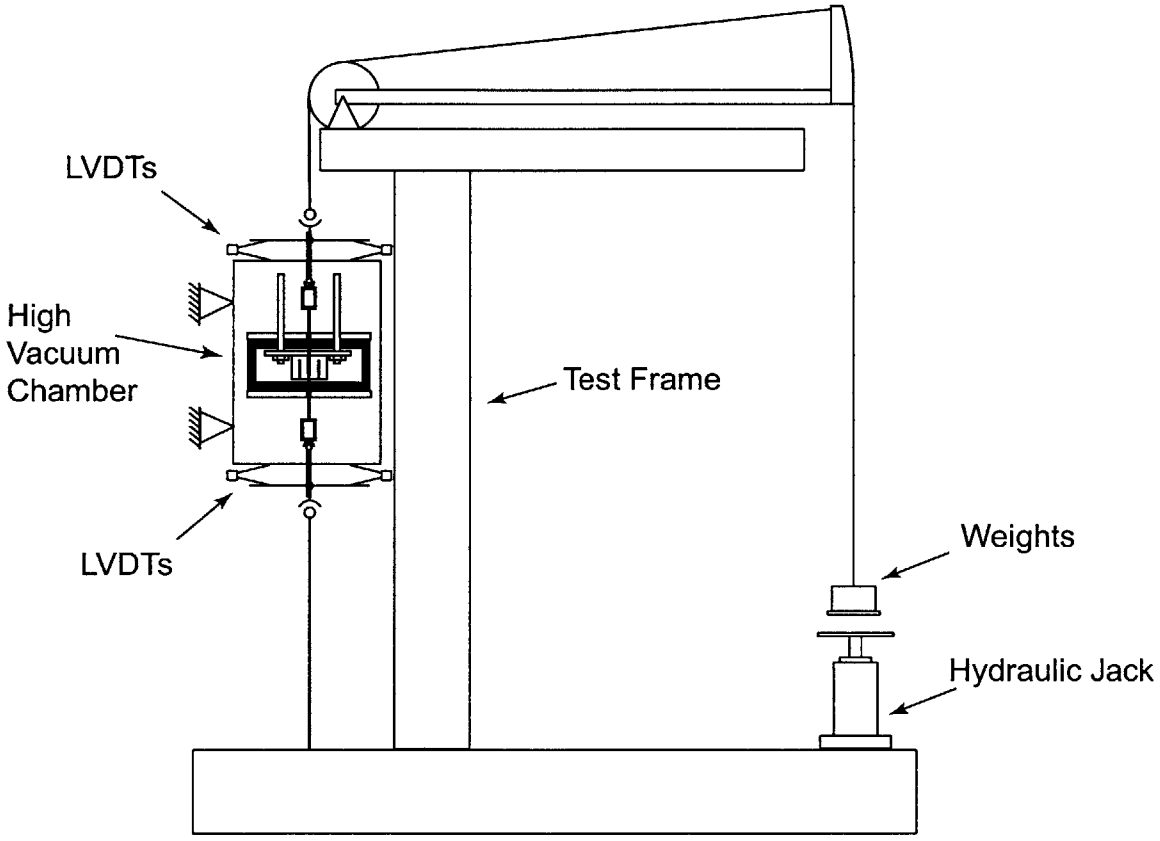

Figure 3-1: Tensile creep testing apparatus, with test Configuration B

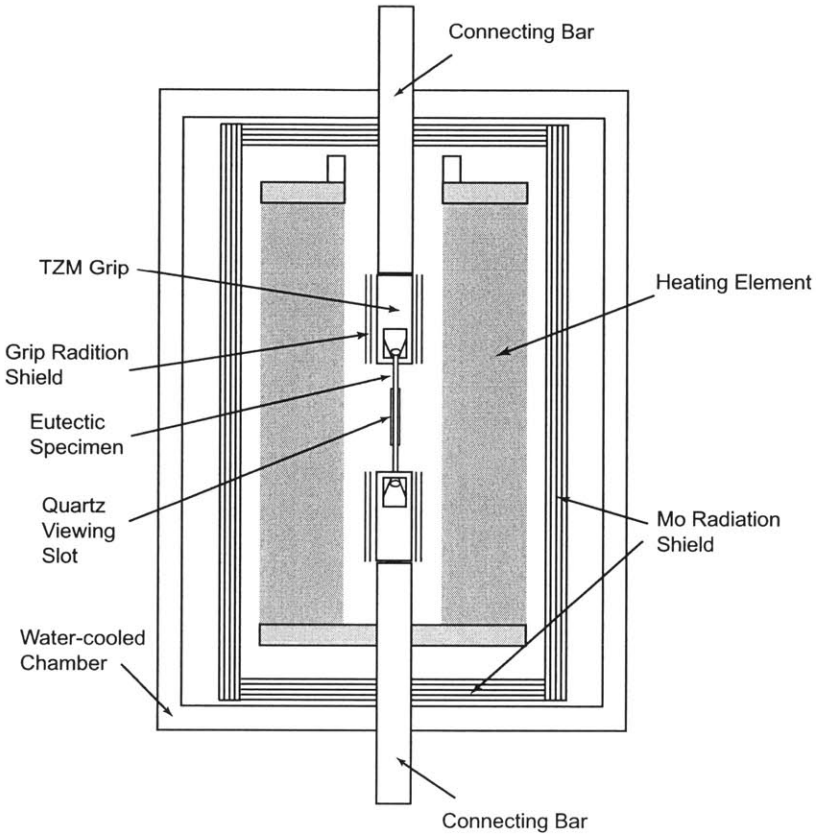

Figure 3-2: Test Configuration A having a full-length W mesh heating element and TZM grips.

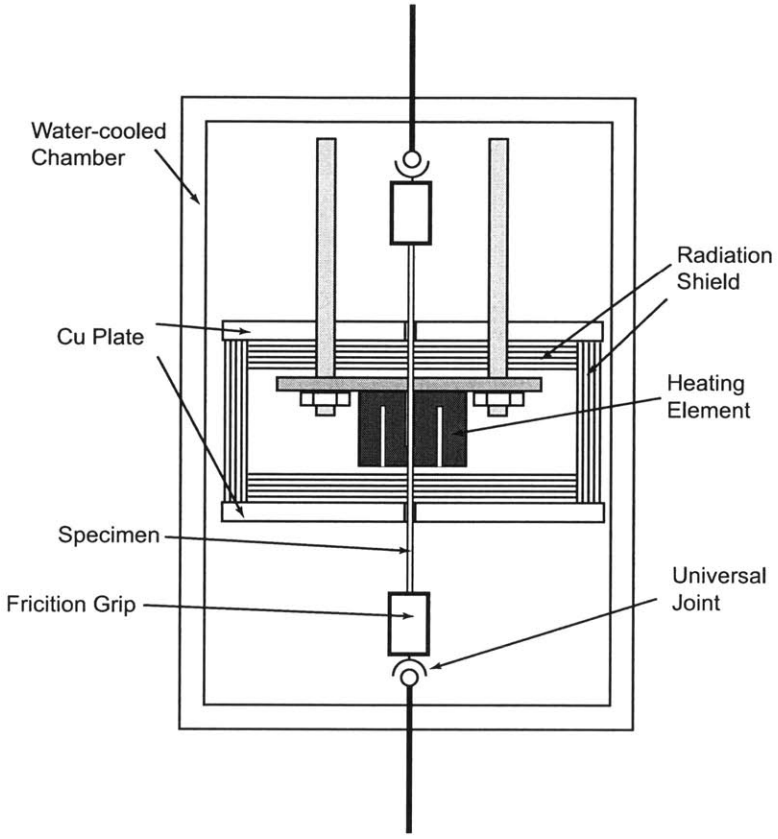

Figure 3-3: Test Configuration B having a customized Ta sheet heating element and metallic friction grips.

the measurements, the displacements of the two ends of the load train immediately outside the vacuum chamber were simultaneously measured by sets of four LVDTs at both the top and bottom ends of the Centorr chamber. The differences between these two measurements then corresponded to the extension of the specimen. Strain resolution of 1.4×10^{-5} was possible with this system. To evaluate the strain measurement system, a Ni-based superalloy CMSX-3 sample was tested at 800°C under a stress of 300 MPa. The creep strain measured was very close to that reported by Pollock [1990].

Even under ideal conditions the total creep strain was never too uniquely determinable. To overcome this difficulty all creep strains at steady state were always measured incrementally at a given temperature under two different applied stresses and often as loading and unloading cycles. This practice of relative measurements of creep strain did not only give more reliable determinations of the strain rates at the two different levels of stress but also demonstrated the nearly complete absence of transients in such incremental changes in steady state creep. A typical response of this type is shown in Fig. 4-5 for creep at 1520°C at stress levels of 150MPa and 200MPa. The random-appearing irregularities on the creep curves in Fig. 4-5 were attributed to be of instrumental origin. When determining actual increments of creep strain in any interval of time these variations were operationally smoothed out.

Chapter 4

Creep Behavior of Al_2O_3/c-$ZrO_2(Y_2O_3)$

4.1 Transient Effects

Upon initial application of stress to a virgin specimen a strain transient was always observed. One such transient recorded during an experiment at 1200°C under a stress of 300 MPa with test Configuration A is shown in Fig. 4-1. There is a strain overshoot at the initial stage of loading, followed by a short incubation period. These two phenomena are more clearly shown in a test with test Configuration B at 1400°C under a series of stresses of 125 MPa, 225 MPa and 275 MPa shown in Fig. 4-2, where in the early stage of creep experiment, under applied stresses of 125 MPa and 225 MPa, the strain decreasing is appeared; while for the later stage, under applied stress of 275 MPa, the strain decreasing is almost not happened.

The characteristic time constant of the transient in Fig 4-1 decreased with increasing temperature, e.g. from c.a. 3.4×10^3sec at 1200°C to 200 sec at 1400°C. The usual explanation of the transient to be due to initial work hardening in the creeping components prior to establishment of a steady state by recovery processes, similar in creep of homogeneous met-

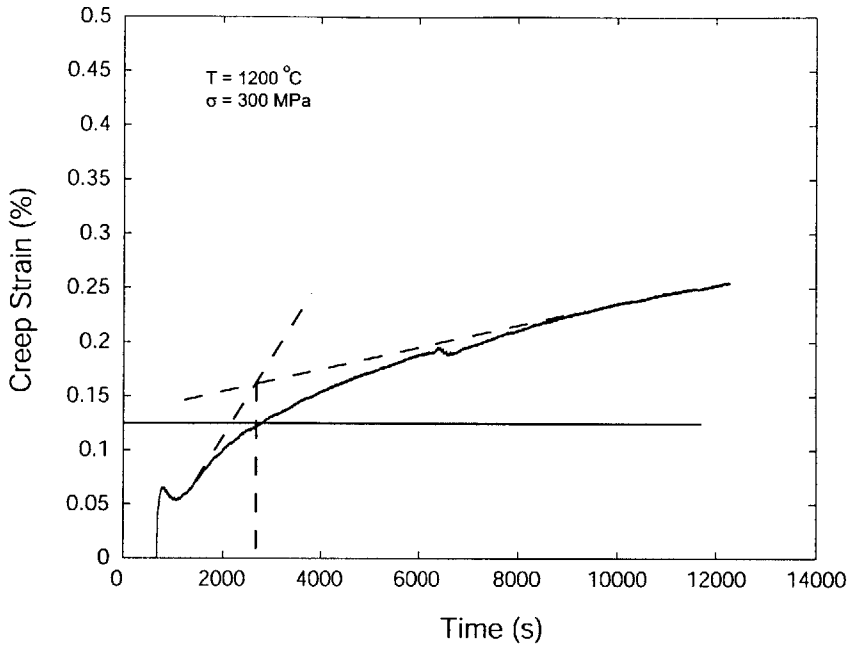

Figure 4-1: A transient creep strain vs. time curve at 1200°C under a stress of 300 MPa.

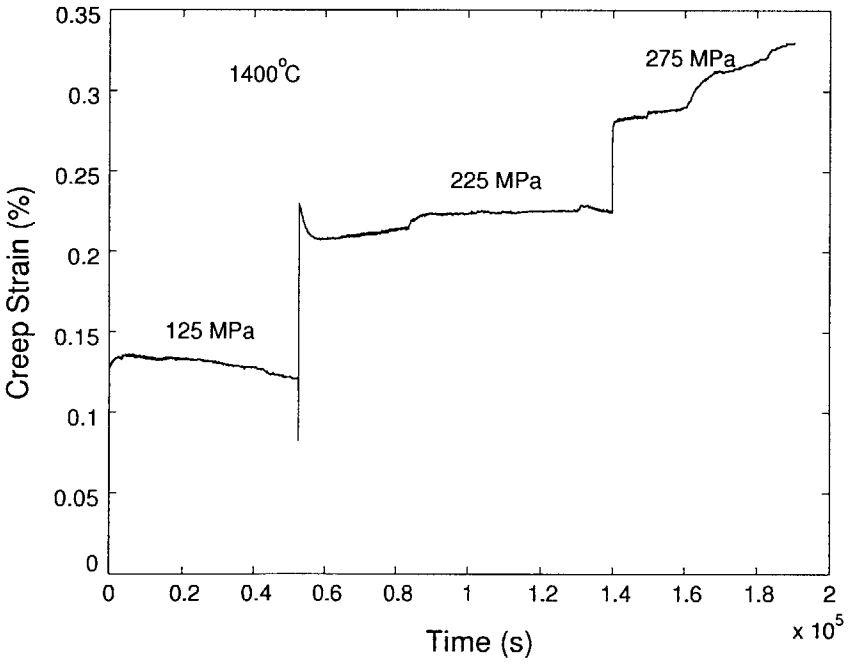

Figure 4-2: A transient creep strain vs. time curve at 1400°C under stresses of 125 MPa, 225 MPa and 275 MPa.

als, was discounted here since no prominent transients were found following stress increases at steady state creep. The most likely cause of the transient was the rapid stress relaxation in the coarse c-ZrO_2 component by creep since for the measured texture of that component there is an abundance of the $< 110 > \{100\}$ principal slip systems that are well oriented for slip, as shown in Fig 4-3 of the loading direction. Moreover, the creep resistance of c-ZrO_2 in this temperature range is known to be poor (Messerschmidt *et al.* [1998]). In more ideal morphologies, as presented in Section 2.2, the coarse component of the c-ZrO_2 is located on colony borders. In the usual less ideal morphologies where fibrillar c-ZrO_2 is still aggregated but does not form well structured colonies the coarse fraction was found to be less regularly distributed (see Fig. 4-4). An upper bound estimate of this effect could be assessed from a Finite Element (FEM) study that will be presented in Section 6.3 where it was found that for the complete relaxation of the deviatoric stresses in the entire c-ZrO_2 phase the volume average deviatoric stresses as well as mean normal stresses in the Al_2O_3, increase roughly by 25-30% which would result in an increment of additional elastic strain in the sample of about 6×10^{-4}. This level is illustrated in Fig. 4-1 by the horizontal line. The actual amount of stress relaxation in the c-ZrO_2, however, is difficult to determine since a substantial fraction of this component has phase dimensions in the range of $0.2 \sim 0.4 \mu$m and is likely to be dislocation-free and incapable of plastically deforming (as will be discussed in Chapter 6). These, and the difficulties in determining the absolute measures of strain derived from the heating zone portions of the specimen requires the de-emphasizing of this portion of the creep response.

4.2 Steady State Creep

As already mentioned in Section 3.2 the main information on steady state creep was obtained from incremental experiments of sudden stress increases and decreases at constant temperature as shown in the typical case of Fig. 4-5 of creep response. A simple check of the

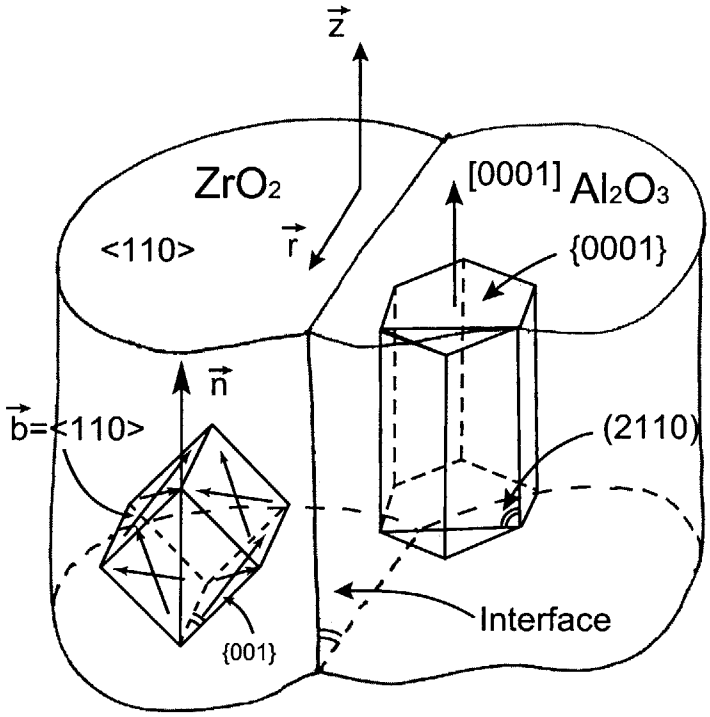

Figure 4-3: Schematic drawing of phase orientation relation of Al_2O_3 and c-ZrO_2 with the major slip systems in ZrO_2.

magnitude of the instantaneous stretches or contractions for stress increases or decreases, utilizing the appropriate information on the temperature dependent Young's modulus of Al_2O_3 (Wolfenden, Wolfenden [1997]) gave in all cases that the recorded jumps were all about a factor of 2 larger than what could be expected from the sample in the heating zone. Since this was well within the additional flexures and relaxations in the loading train the recorded strain rates were considered to be reliable.

Utilizing test Configuration B, several determinations of steady state creep rate were successfully made, all together at 3 temperatures of 1200, 1400, 1520°C at stress levels ranging from 150MPa to 275MPa, derived from incremental experiments similar to those in Fig. 4-5. These measurements are listed in Table 4.1 and are plotted in Fig. 4-6 together with the creep rates at 1400°C due to Sayir and Farmer [2000], also quoted in Sayir [1998][a]. The stress exponents of the creep rates at 1400°C and 1520°C, shown in Fig. 4-6, are 4.16 and 5.38 and are lower than that of Sayir at 6.00. As discussing in the creep model in Section 6.2, these exponents are relatively high and need to be explained.

Table 4.1 contains also sufficient information for the determination of the activation energy of the governing creep process. The plot of the creep rates at a stress of 200MPa for three temperatures of 1200°C, 1400°C and 1520°C in Fig. 4-7 gives an activation energy of Q = 299 kJ/mol for the rate controlling process in steady state creep which is considered to be due to oxygen ion diffusion which is known to be the slowest species in Al_2O_3. It is certainly lower than the activation energy in single crystal c-ZrO_2 governing its creep process, which is range from 539 to 857 kJ/mol from 1300°C to 1800°C compiled by Messerschmidt *et al.* [1998]. The value from eutectic is to be compared with 311 kJ/mol at 114 MPa and 340 kJ/mol at 75 MPa for 0° sapphire, both from 1600°C to 1800°C, measured by Firestone and Heuer [1976]. It also can be compared with 441 kJ/mol for temperatures above 1400°C and 109 kJ/mol for temperatures below 1400°C for the same process measured by Oishi

[a]The higher creep rates and the larger exponents in these early investigations are most likely a result of not reaching steady state but still being in a late stage of transient behavior.

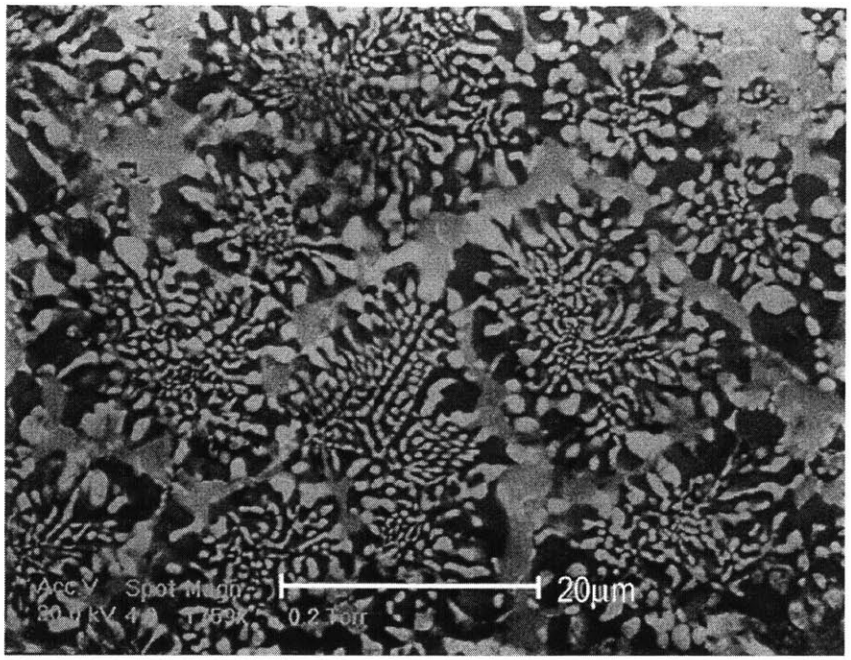

Figure 4-4: Not well structured colonies in transversal section of Al_2O_3/c-ZrO_2.

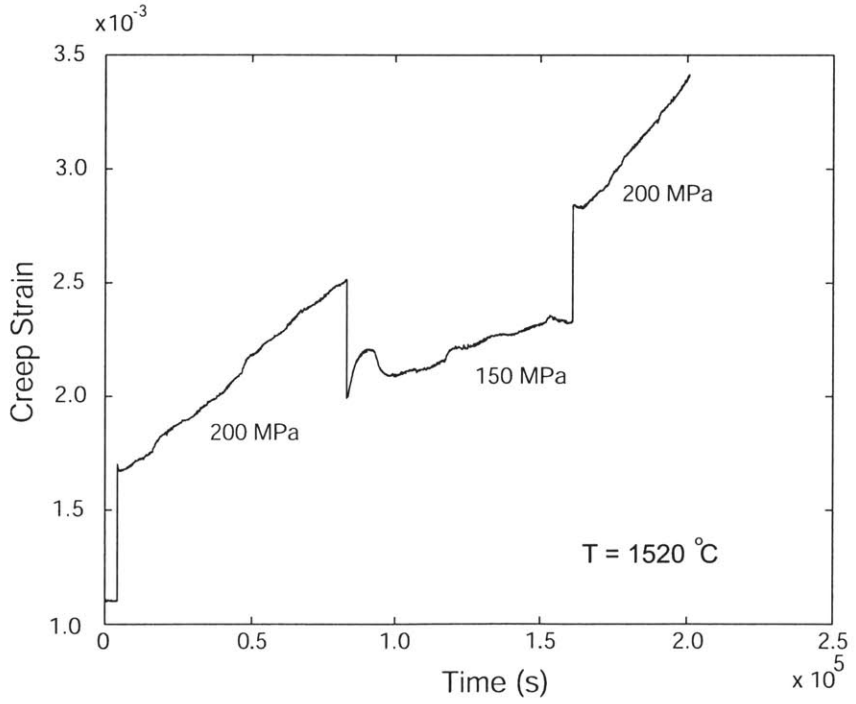

Figure 4-5: A typical creep strain vs. time curve at 1520°C under two different stresses of 150MPa and 200MPa

Table 4.1: Recorded Steady State Strain Rates

Stress (MPa)	Strain Rate $\dot{\epsilon}$(sample #) (sec^{-1})	$\dot{\bar{\epsilon}}$ average rate (sec^{-1})
	1200°C	
200	1.97×10^{-10} (142-18)	1.97×10^{-10}
	1400°C	
200	3.6×10^{-9} (187-29)	3.6×10^{-9}
225	2.26×10^{-9} (187-27-2); 8.16×10^{-9} (187-27-1)	5.21×10^{-9}
250	5.53×10^{-9} (187-29)	5.53×10^{-9}
275	9.95×10^{-9} (187-27-2); 1.10×10^{-8} (187-27-1)	1.05×10^{-8}
	1520°C	
150	1.57×10^{-9} (142-16); 4.40×10^{-9} (142-16)	2.98×10^{-9}
200	1.20×10^{-8} (142-16); 1.60×10^{-8} (142-16)	1.40×10^{-8}

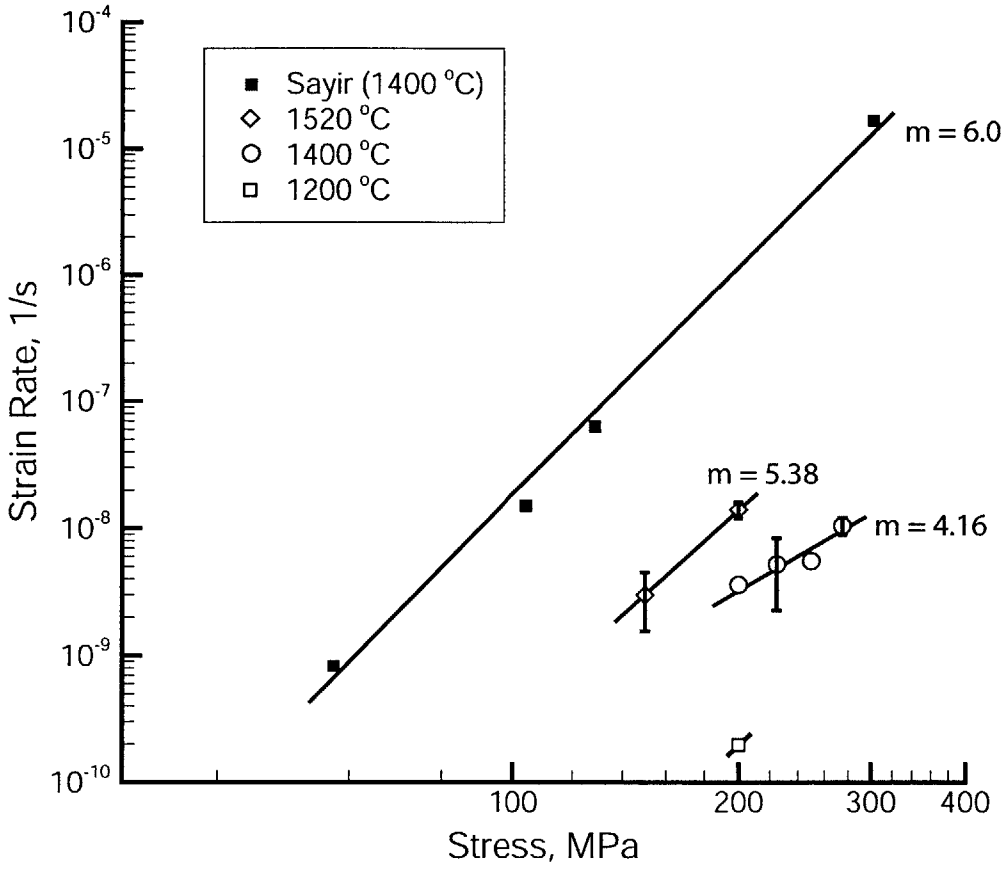

Figure 4-6: Plots of steady state creep rates as a function of stress for temperatures of 1200, 1400 and 1520°C compared with measurements reported by Sayir and Farmer [2000].

and Kingery [1960] in pure polycrystalline Al_2O_3. The somewhat lower magnitude of the measured activation energy for oxygen ion diffusion is attributed to the likelihood that a significant fraction of the diffusion current will be along the the incoherent interfaces.

4.3 Microstructure Coarsening Experiment

For materials serving at high temperature, microstructure coarsening is a common phenomenon for a large area of boundaries, where it becomes thermodynamically favorable to decrease the total boundary area per unit volume. The directional coarsening ('rafting') in nickel-base superalloy single crystals at high temperature has been widely reported in the past (Pollock and Argon [1994], Socrate and Parks [1993]). In nickel-base superalloy single crystals, the microstructure consists of an f.c.c nickel solid solution matric, γ, with Ni_3Al precipitates, γ', which are ordered and coherent with the matrix. After long term aging the precipitates are distributed in the matrix as a stable periodic array of <100> aligned uniform cuboids with (100) faces, with a size of $0.2\sim0.5\mu$m (Pollock [1990], Pollock and Argon [1992] and Socrate and Parks [1993]). At 900°C, the γ' cuboidal precipitates begin to link together to form plates (rafts), as shown in Fig 4-9 along with the as-aged (before rafting) microstructure shown in Fig 4-8.

The phase morphologies in directionally solidified eutectic Al_2O_3/c-ZrO_2 are similar to those of nickel-base superalloy. Although there is no report so far about such possible coarsening of eutectic microstructure, it should be carefully examined in the creep temperature range of 1200°C to 1520°C of interest in this investigation. If the phase morphology of c-ZrO_2 fiber indeed coarsens, the steady state creep behavior will be altered because of changed phase-spacing of c-ZrO_2 domain.

A eutectic Al_2O_3/c-ZrO_2 sample was exposed to 1400°C without applying stress for a series of time periods of 24, 72 and 168 hours. After each targeted time period, the sample was taken out, and a slice was cut and polished to examine the microstructure by SEM.

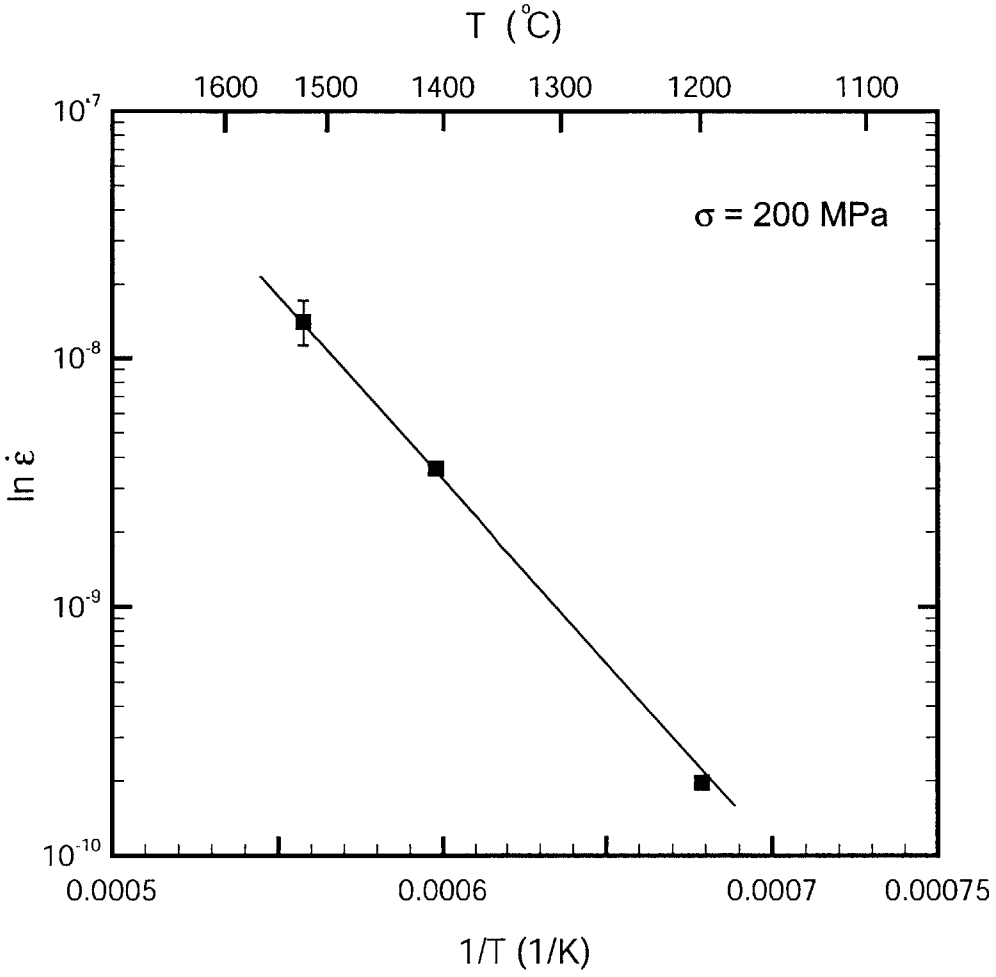

Figure 4-7: Determination of activation energy of steady state creep from temperature dependence of steady state creep rate.

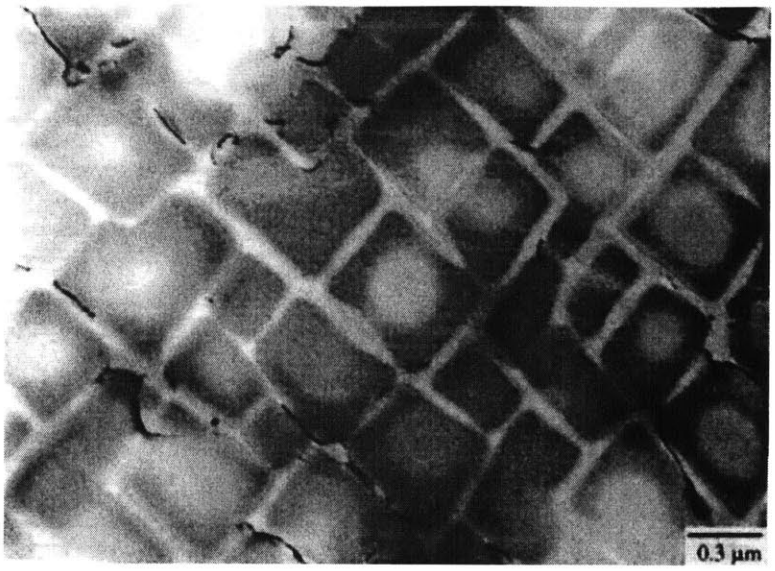

Figure 4-8: As-aged microstructure of superalloy single crystal, present at the beginning of the coarsening experiment. Some degree of precipitate coalescence is evident in the absence of externally applied stresses. (Pollock and Argon [1994])

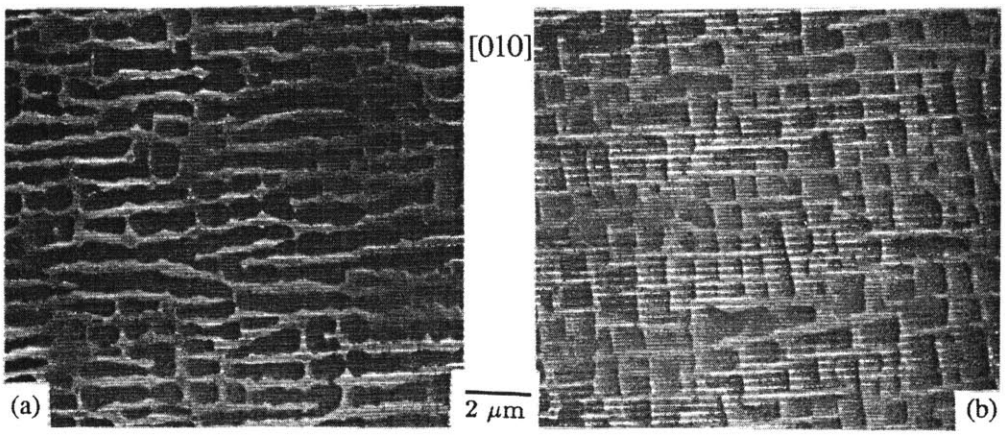

Figure 4-9: Coarsened inhomogeneous microstructure of superalloy single crystal within an individual sample following the 1050°C and 50MPa stressed coarsening experiment. The plane of the micrograph is parallel to the stress axis, which is in the vertical direction. (Pollock and Argon [1994])

Fig 4-10 and Fig 4-11 show the microstructure of each time period along with the one of the as-grown eutectic. The size and morphology of colonies and the c-ZrO_2 fibers within colonies have barely changed. The microstructure almost has no change at 1400°C for as long as 168 hours without stress.

The microstructure of a specimen subjected to 300MPa stress at 1400°C for about 168 hours is also shown in Fig 4-12 (a) and (b) comparing with those without stressing as in Fig 4-10 (d) and Fig 4-11 (d). The size and morphology of colonies and the c-ZrO_2 fibers within colonies show no difference with or without applied stress.

In this research, it became impossible to conduct microstructure coarsening experiments at higher temperature, such as 1600°C. It should be expected that at the temperature as high as 1600°C, which is close to the eutectic temperature, 1875°C, it is possible that there is some forms of microstructure coarsening happened similar to the rafting in Nickel-base superalloy single crystals as described by Pollock and Argon [1994].

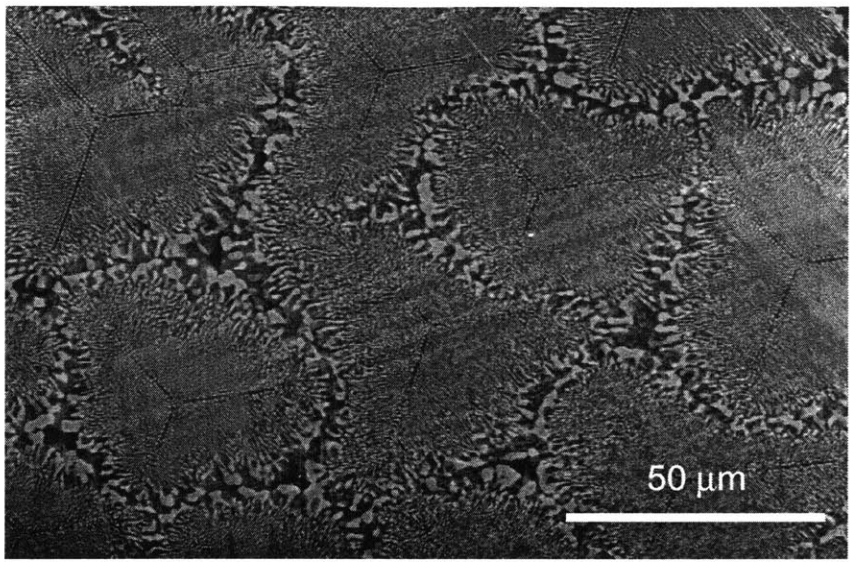

(a)

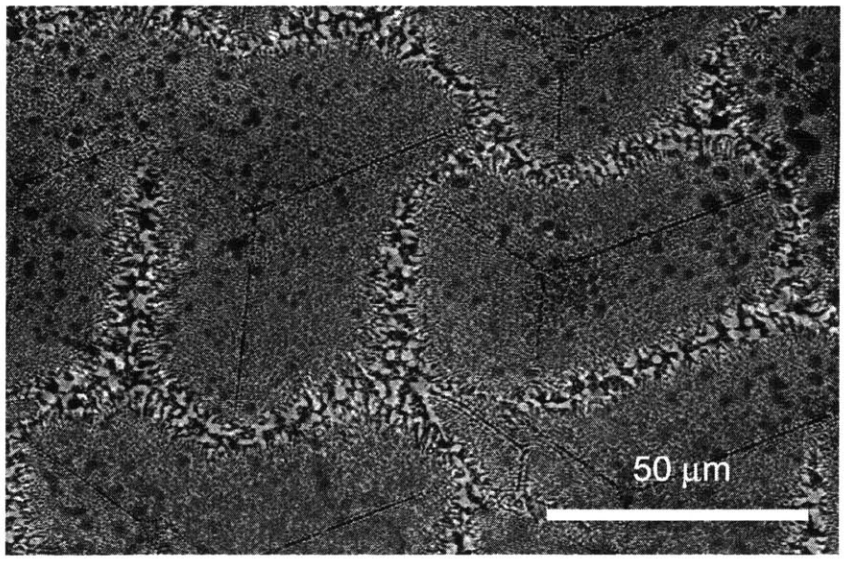

(b)

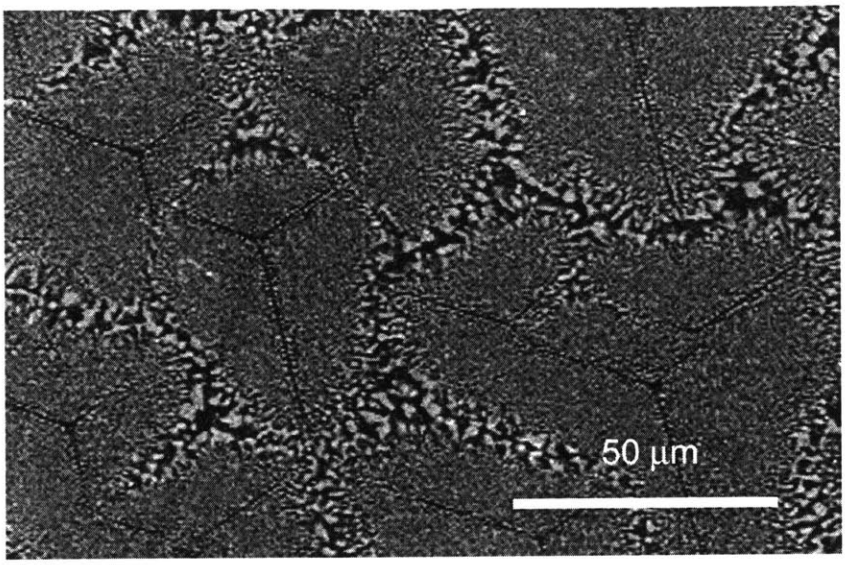

(c)

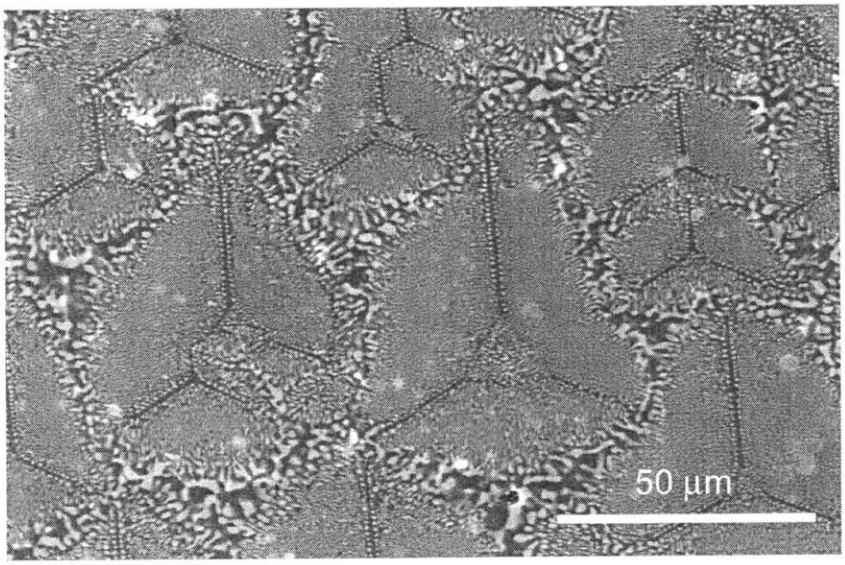

(d)

Figure 4-10: The microstructure of eutectic Al_2O_3/c-ZrO_2 specimen tested in 1400°C without applying stress for different time periods. (a) as-grown; (b) 24 hours; (c) 72 hours; (d) 168 hours

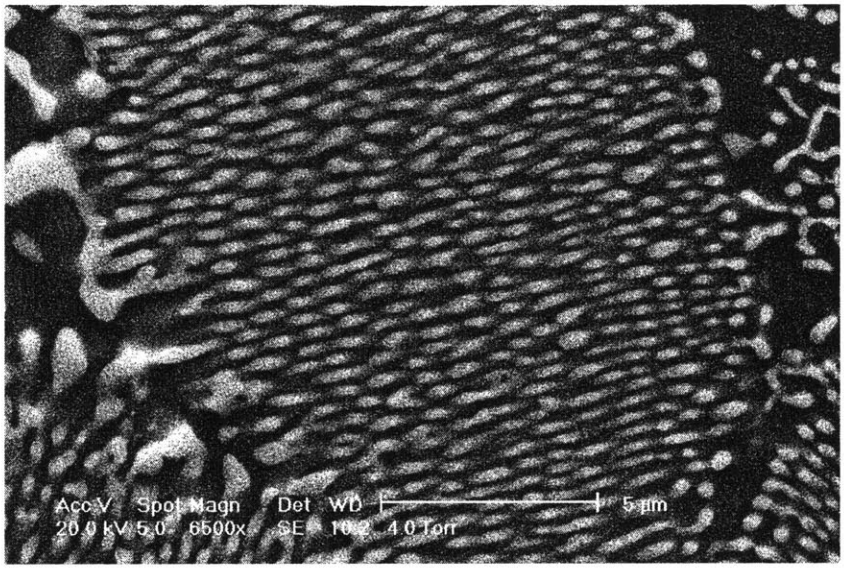
Acc.V Spot Magn Det WD 5 μm
20.0 kV 5.0 6500x SE 10.2 4.0 Torr

(a)

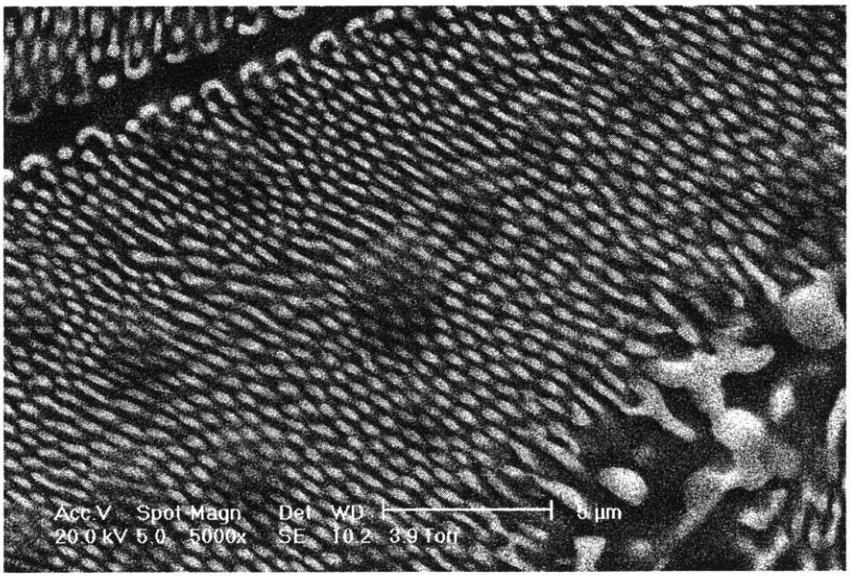
Acc.V Spot Magn Det WD 5 μm
20.0 kV 5.0 5000x SE 10.2 3.9 Torr

(b)

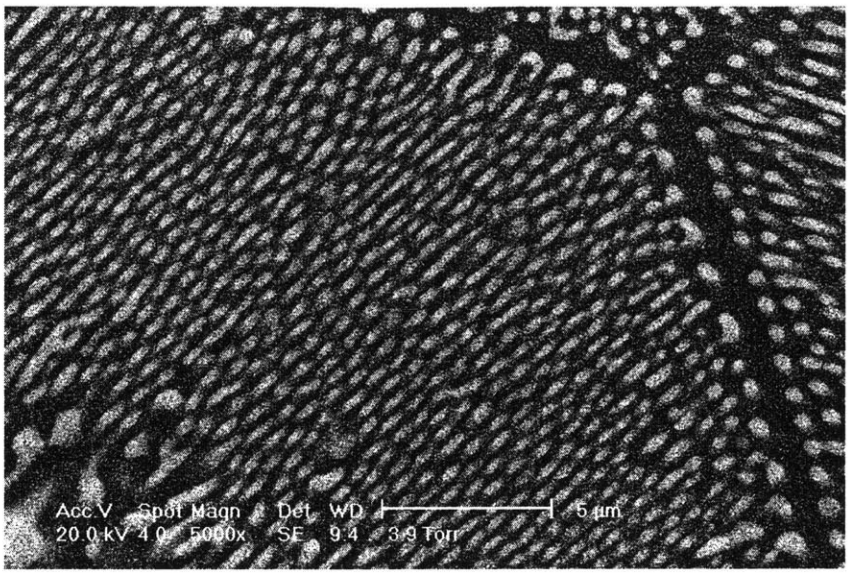

(c)

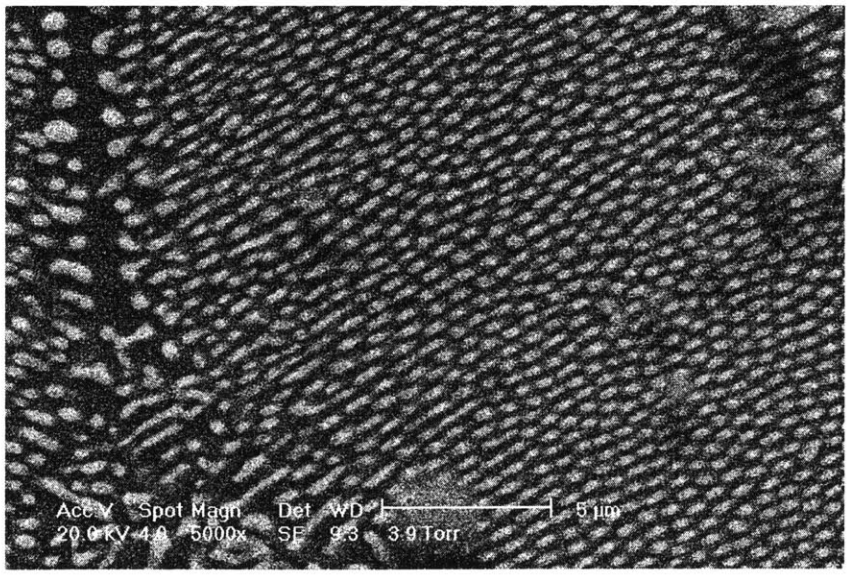

(d)

Figure 4-11: The microstructure of eutectic Al_2O_3/c-ZrO_2 specimen tested in 1400°C without applying stress for different time periods. (a) as-grown; (b) 24 hours; (c) 72 hours; (d) 168 hours

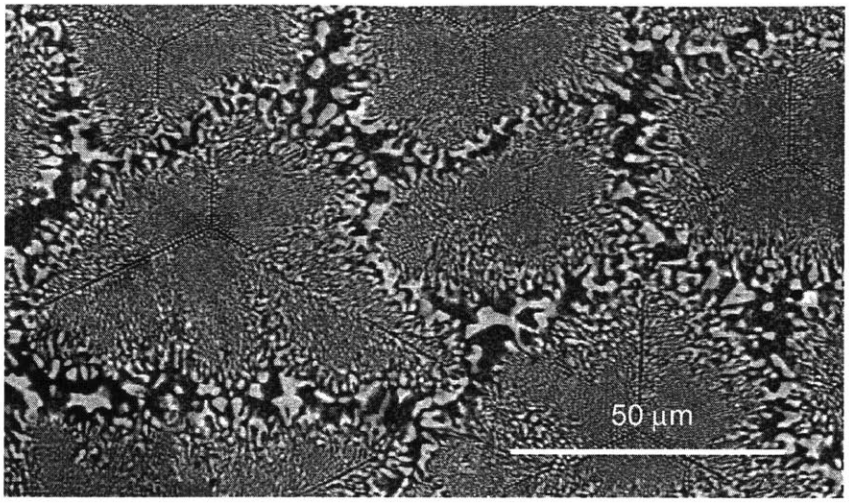

(a)

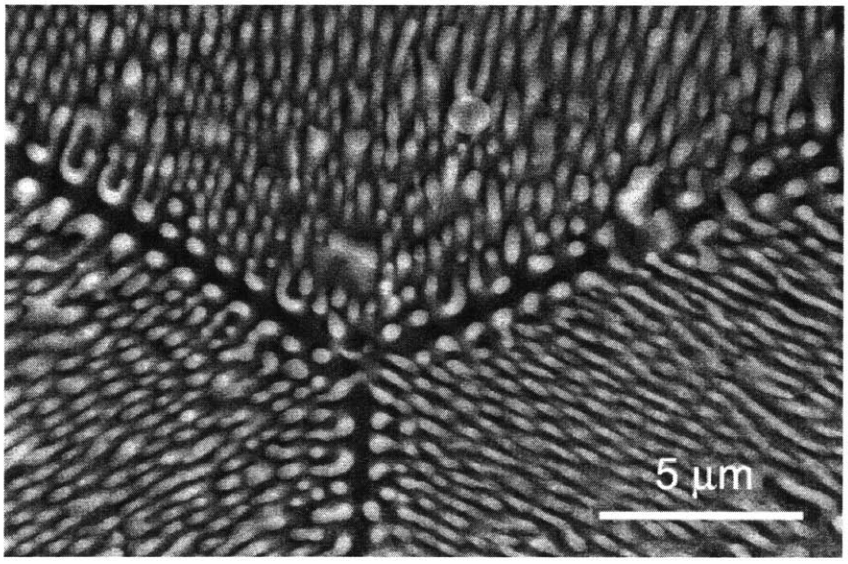

(b)

Figure 4-12: The microstructure of a eutectic Al_2O_3/c-ZrO_2 specimen tested in 1400°C with 300MPa stress for about 168 hours. (a) low magnification (b) high magnification

Chapter 5

Transmission Electron Microscopy

5.1 TEM Foil Preparation

After a specimen fractured by creep at high temperature, the cooling procedure started within 20~30 minutes and resulted in a cooling rate of ~1000°C in 30 mins. From either as-grown specimen or crept specimen, foils for transmission electron microscopy were prepared by initially cutting 1-2mm thick slices transverse to the specimen axis, or 2-3 mm thick slices parallel to the axis, using a SBT Model 660 low speed diamond saw (South Bay Technology, San Clemente, CA). These slices were then mounted on a SBT Model 590 Tripod Polisher (South Bay Technology, San Clemente, CA) vertically (for transversal section) or horizontally (for axial section). After mounting, slices were lapped and polished down to electron transparent thickness on that Tripod Polisher with a wedge angle of 1^{o} by diamond particle films. The foils were then detached from Tripod Polisher and glued to a 3mm copper TEM grid (from Ted Pella, Redding, CA) with a single 1×2mm slot. It was followed by 20~30 minutes of ion milling to remove surface mechanical polishing defects. The mechanical thinning by Tripod Polisher dramatically limited ion milling requirements which could cause preferential thinning, radiation damage, or creation of surface topography. Since the eutectic is brittle, the yield of useful TEM foils was usually fairly

low.

5.2 TEM Operations

Two different transmission electron microscopes were used in this research, a JOEL 2000 at an accelerating voltage of 200kV, and a JOEL 2010 High Resolution TEM at an accelerating voltage of 200kV. The first microscope was mainly used for general observation, such as, dislocation characterization; while the latter one was used for observations of phase interfaces and direct lattice images. In both microscopes, the double tilting sample holders were necessary.

Electron diffraction was used very often to identify the crystal orientation during general observation, dislocation characterization and many other cases. Convergent beam electron diffraction (CBED) (Williams and Carter [1996]) was also used to obtain 3D crystal information of single crystal Al_2O_3.

Stereo pairs (Pollock [1990] and Williams and Carter [1996]) were obtained by maintaining a two beam condition (constant $\mathbf{g}$ and $\mathbf{s}$) while sample was tilted by 6-20° (depending on the magnification). Stereo pair photos were printed with the emulsion side up. This shows the same image as if looking down on the specimen as it was oriented in the TEM column. Viewing with a special stereo viewer, the photos were oriented with the tilt axis vertical and the $\mathbf{g}$ vectors pointing away from the center of the stereo pair.

The usual strain contrast technique (Head *et al.* [1967] and Williams and Carter [1996]) was widely used to characterize dislocations. It gives the invisibility criteria of dislocation images of $\mathbf{g} \cdot \mathbf{b} = 0$ and $\mathbf{g} \cdot \mathbf{b} \times \mathbf{u} = 0$, where $\mathbf{g}$ is the reflecting vector, $\mathbf{b}$ is the Burgers vector, and $\mathbf{u}$ is a vector along the dislocation line. In the case of isotropic elasticity (Head *et al.* [1967] and Williams and Carter [1996]), the criteria $\mathbf{g} \cdot \mathbf{b} = 0$ has to be satisfied for a pure screw dislocation to be invisible; while $\mathbf{g} \cdot \mathbf{b} = 0$ and $\mathbf{g} \cdot \mathbf{b} \times \mathbf{u} = 0$ have to be satisfied for an edge dislocation to be invisible. In these cases, the electron beam is transmitted

as if through an undistorted crystal even with the presence of the dislocation, so there is no contrast from the dislocations. Because of the very small elastic anisotropy of Al_2O_3, these usual strain contrast techniques can be used to characterize the Burgers vector of dislocations (Cadoz *et al.* [1982]). The excitation error s, is usually set to be slightly larger than 0. In such case, the distortion due to the defect will bend the near-diffracting planes back into the Bragg-diffracting condition to give strong contrast.

5.3 Dislocation Systems in Al_2O_3

The crystallography of Al_2O_3 was lucidly described by Kronberg [1957], who described a simplified system of anion and cation layers in detail, and demonstrated that it was convenient to define the unit cell by the normally-vacant octahedral sites in the structure. Kronberg's idealization of the crystal structure of sapphire is shown in Fig. 5-1. It was then illustrated by Bilde-Sørensen *et al.* [1996] that the cations are displaced along the c-axis toward normally-vacant octahedral sites in the structure. Because of the cation displacements along [0001], the "cation sheets" are "staggered" rather than "flat". This in turn distorts the oxygen sublattice in that it gives rise to different oxygen-oxygen bond lengths within an "oxygen sheet".

The shortest Burgers vectors in Al_2O_3 are listed in Table 5.1. Considering the reported slip planes, Table 5.2 lists the possible slip systems in Al_2O_3. The Burgers vector of basal, prismatic and pyramidal system are shown in Fig 5-1.

5.4 Dislocations in Al_2O_3/c-$ZrO_2(Y_2O_3)$ Specimens

In general, no dislocation has been observed in the very few foils of as-grown (undeformed) specimens in either Al_2O_3 or ZrO_2 phase. This was expected, given the small area which can be viewed under TEM and very low dislocation density possibly in as-grown eutectic specimens. However, in general, solidification dislocations could exist in the as-grown

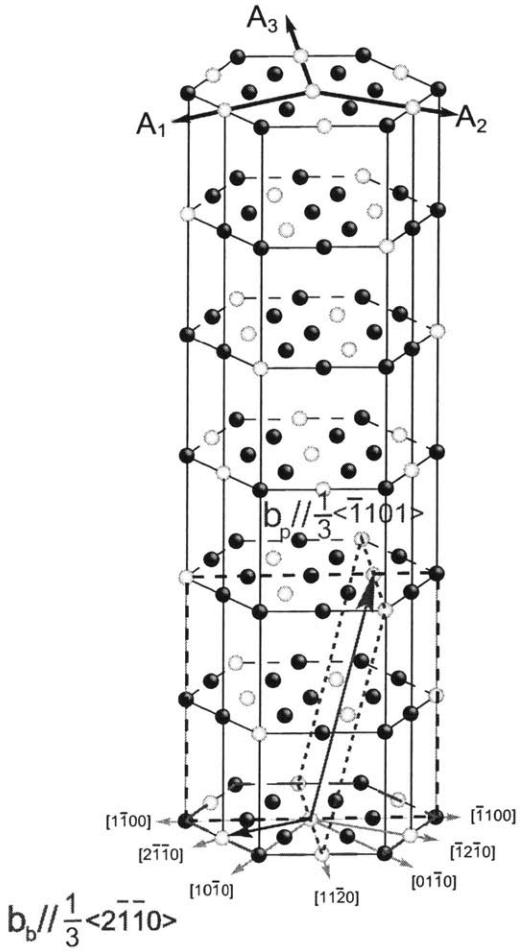

Figure 5-1: Crystal structure of sapphire, only filled and empty cation sites are shown; the anions lying in close-packed layers between the cation layers are not shown. The Burgers vectors of basal, prismatic and pyramidal systems are identified in the figure.

Table 5.1: Shortest Burgers Vectors in Al_2O_3 (Snow and Heuer [1973])

Burgers Vector, **b**	Magnitude of unit **b** (Å)
$1/3 < 11\bar{2}0 >$	4.75
$1/3 < \bar{1}101 >$	5.12
$1/3 < \bar{2}021 >$	6.98
$< 10\bar{1}0 >$	8.22
$1/3 < 21\bar{3}1 >$	8.44
$1/3 < \bar{1}012 >$	9.08

Table 5.2: Dislocation slip systems in Al_2O_3 (Snow and Heuer [1973])

Reported slip planes		possible slip systems
0001	(0001)	$1/3 < 11\bar{2}0 >, < 10\bar{1}0 >$
$10\bar{1}0$	$\{10\bar{1}0\}$	$1/3 < \bar{1}2\bar{1}0 >$
$11\bar{2}0$	$\{11\bar{2}0\}$	$1/3 < \bar{1}101 >, 1/3 < 2\bar{2}01 >, < \bar{1}100 >, 1/3 < 1\bar{1}02 >$
$01\bar{1}2$	$\{01\bar{1}2\}$	$1/3 < 2\bar{1}\bar{1}0 >, 1/3 < 0\bar{1}11 >, 1/3 < \bar{2}021 >$
$10\bar{1}1$	$\{10\bar{1}1\}$	$1/3 < \bar{1}2\bar{1}0 >, 1/3 < \bar{1}101 >$
$2\bar{1}\bar{1}3$	$\{2\bar{1}\bar{1}3\}$	$1/3 < \bar{1}101 >, < 01\bar{1}0 >$
$2\bar{1}\bar{1}2$	$\{2\bar{1}\bar{1}2\}$	$< 01\bar{1}0 >, 1/3 < \bar{1}012 >$
$4\bar{2}\bar{2}3$	$\{4\bar{2}\bar{2}3\}$	$< 01\bar{1}0 >$

eutectic specimens.

In a sample crept at 1400°C under an applied stress of 250 MPa with a creep strain of about 0.2% there are different forms of dislocation, such as, long dislocations and dislocation nodes in Fig 5-2, and an array of dislocation forming a low angle boundary in Fig 5-3.

A pair of dislocations in Al_2O_3 is shown in Fig 5-4. They are identified as those having Burgers vector of $1/3[10\bar{1}1]$ and $1/3[\bar{1}101]$. They are out of contrast for $(\bar{1}2\bar{1}0)$ and $(11\bar{2}0)$ operating reflections, respectively, as shown in Fig 5-4b and Fig 5-4c.

Dislocations in Al_2O_3 interacting with ZrO_2 phases are also found in the channels between ZrO_2 fibers, as shown in Fig 5-5. Most of these dislocations have $1/3 < \bar{1}101 >$ type of Burgers vector, which belongs to the pyramidal system.

Fig 5-6 is a typical Al_2O_3 region with dislocations between ZrO_2 domains. The dislocations in the figure have different types of Burgers vector. Dislocations C, D, E, and F were of basal type Burgers vector of $1/3[\bar{1}2\bar{1}0]$. They are out of contrast in an operating reflection of $\{\bar{1}010\}$, shown in Fig 5-7. Dislocations A, I and G were of pyramidal type Burgers vector of $1/3[\bar{1}101]$. They are out of contrast in operating reflection of $\{\bar{1}\bar{1}20\}$, shown in Fig 5-8. Dislocations B and H were of pyramidal type Burgers vectors of $1/3[0\bar{1}11]$. They are out of contrast at an operation reflection of $\{\bar{2}110\}$, shown in Fig 5-9.

There are several dislocations attached to the phase interfaces, as indicated in Fig 5-10 and Fig 5-11. They are identified as dislocations with basal type Burgers vectors of $1/3[\bar{2}110]$ (Fig 5-10 dislocation A) and $1/3[\bar{1}2\bar{1}0]$ (Fig 5-10 dislocation B), and $1/3[\bar{1}2\bar{1}0]$ (Fig 5-10).

Low angle boundaries were found in different form along the colony boundary, shown in figure 5-12, 5-13 and 5-14. In Fig 5-12, a close-up view of the low angle boundary shows the boundary has two sets of dislocations, and these two sets have split with the individual sets following separately along the interfaces of a c-ZrO_2 domain. Such separation and close association of the boundaries with the interfaces signifies a combination of minimization of boundary energy due to the different elastic properties of the Al_2O_3 and the c-ZrO_2

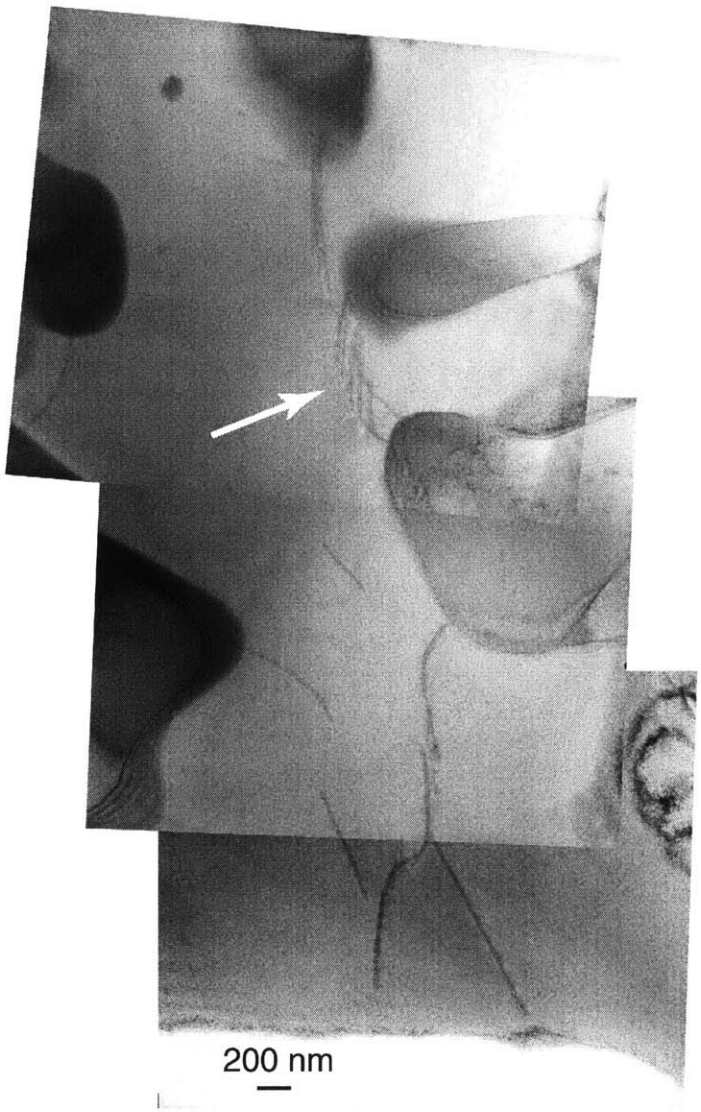

Figure 5-2: Dislocations in crept specimen by a basal plane foil in electron bright-field micrograph at 200kV. The dislocations in this micrograph are discussed in more detail in Fig 5-6.

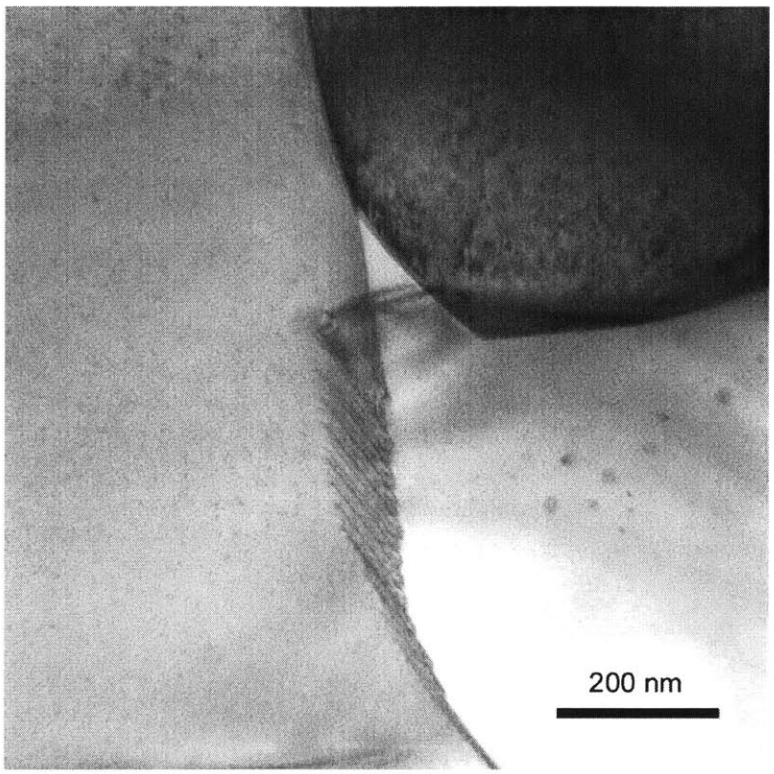

Figure 5-3: Low angle boundary formed between the columnar colonies. The boundary is split out to be merged with c-ZrO_2 phase.

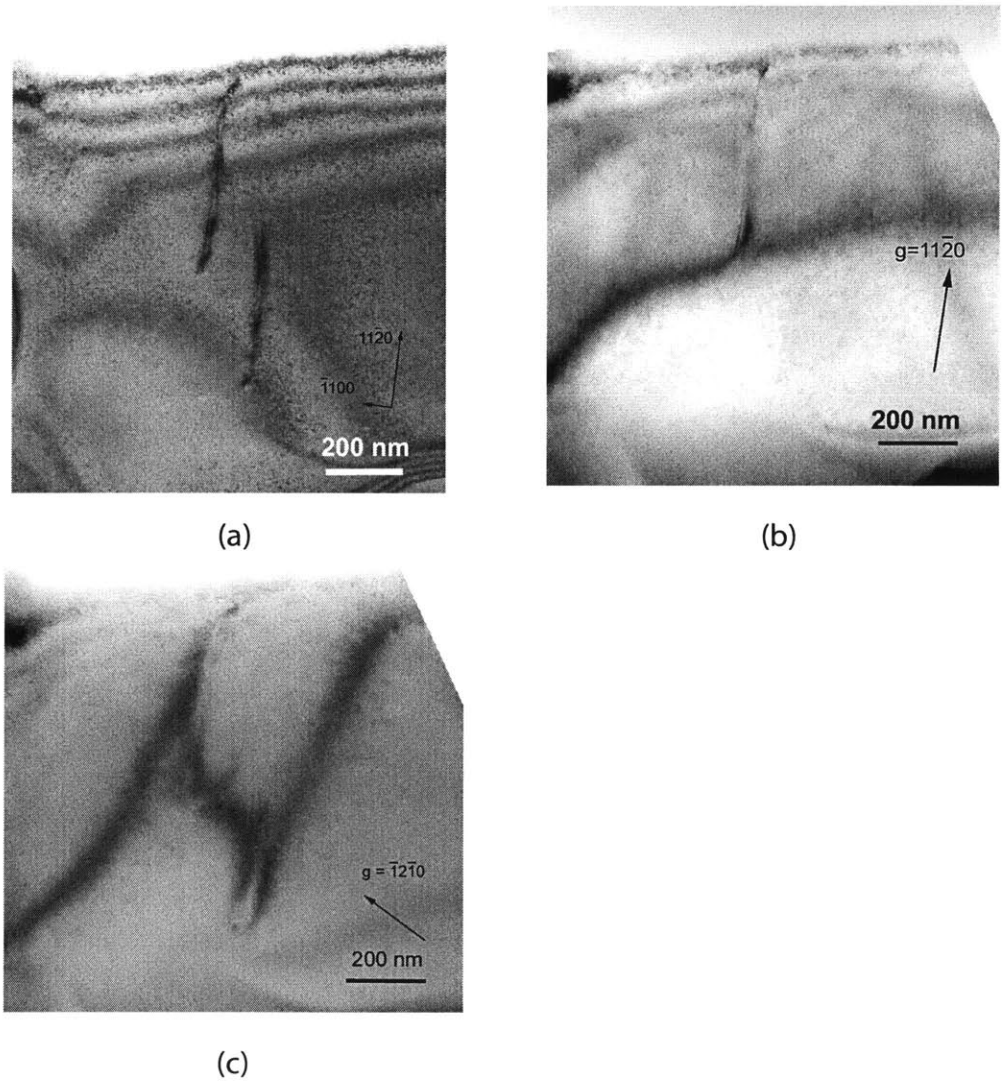

Figure 5-4: Dislocation in basal plane foil of crept specimen. (a) bright field; (b) bright field with $\{\bar{1}2\bar{1}0\}$ operating reflection; and (c) bright field with $\{11\bar{2}0\}$ operating reflection.

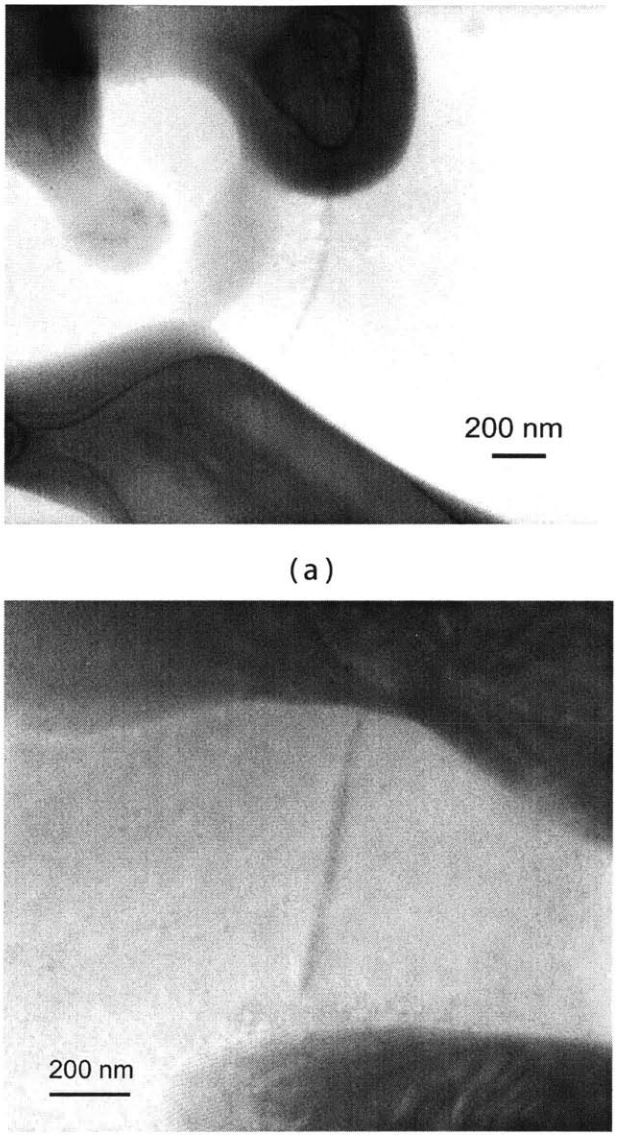

Figure 5-5: Dislocations in Al_2O_3 phase channeling through c-ZrO_2 domains.

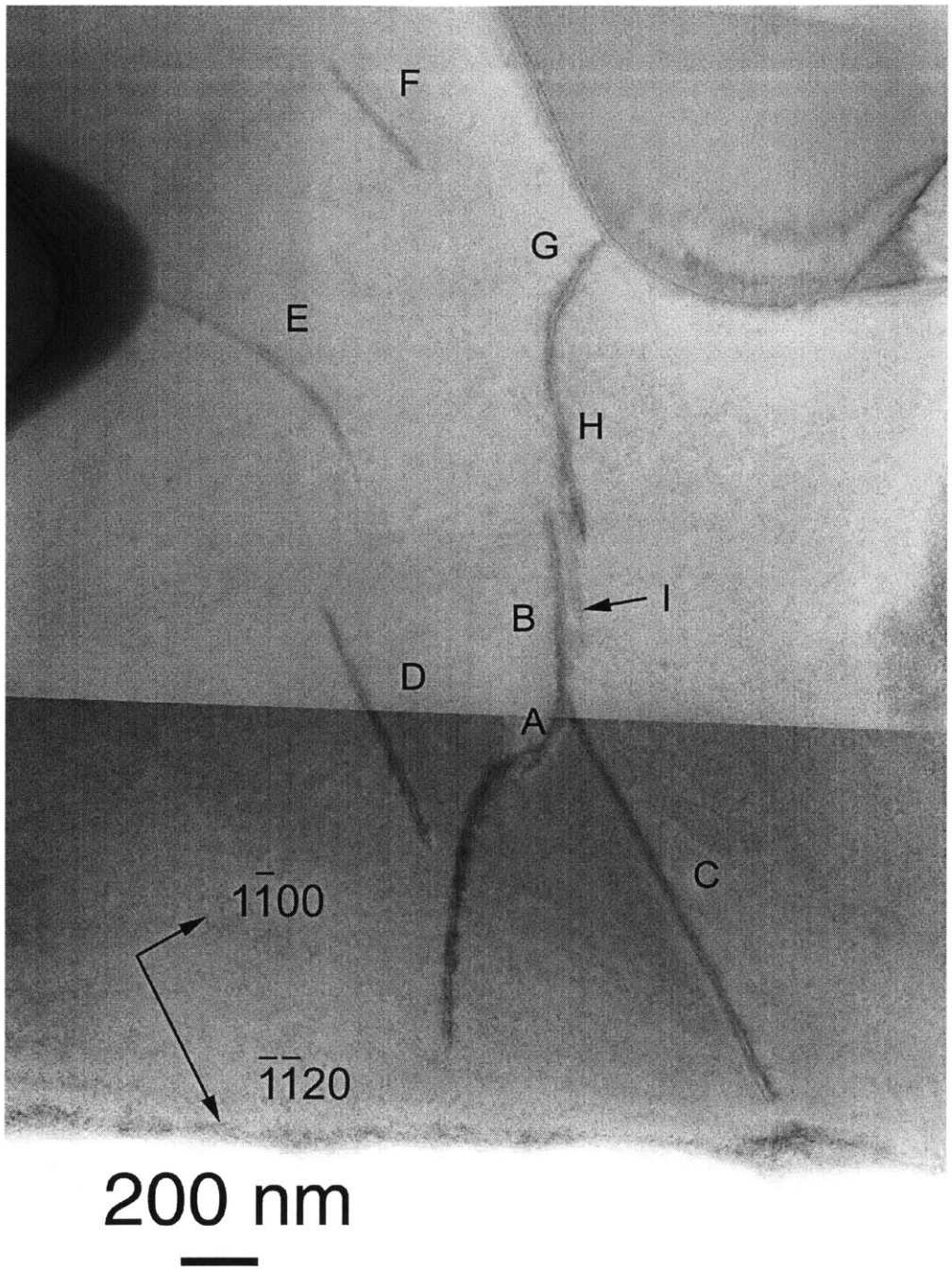

Figure 5-6: Dislocations in basal plane foil of crept specimen (bright-field electron micrograph, 200kV).

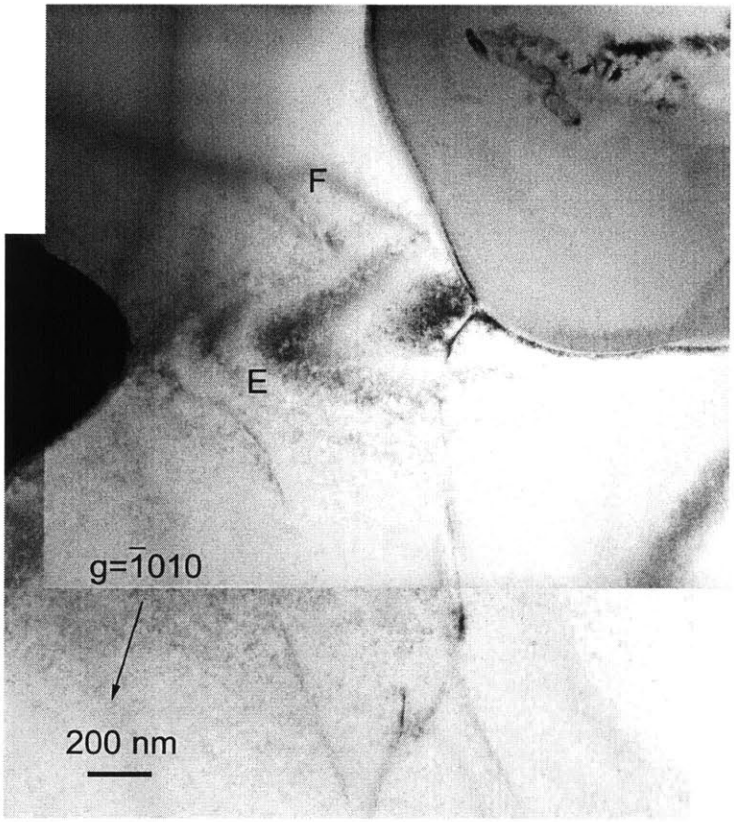

Figure 5-7: Dislocations in lower part of Fig 5-6 under operating reflection of $\{\bar{1}010\}$.

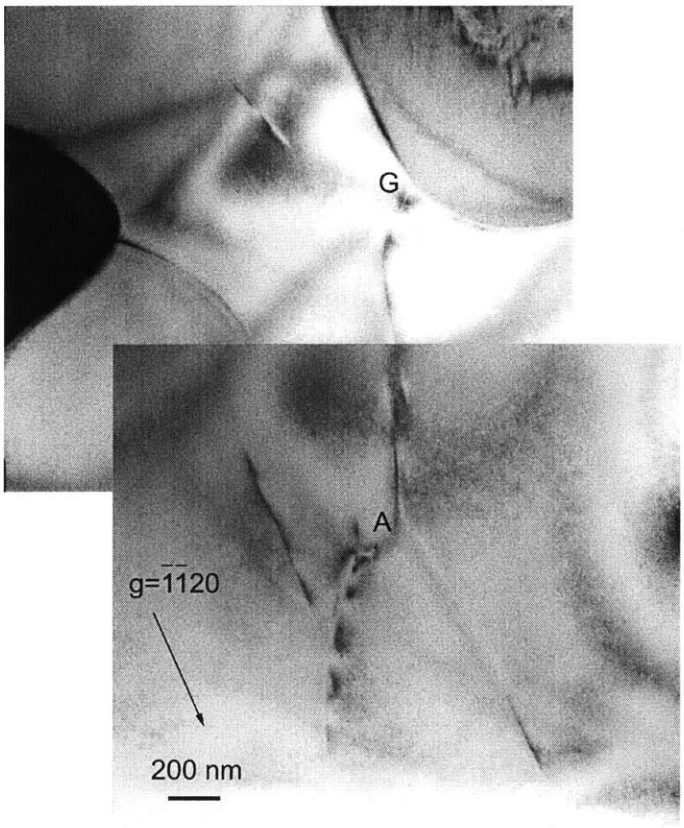

Figure 5-8: Dislocations in lower part of Fig 5-6 under operating reflection of $\{\bar{1}\bar{1}20\}$.

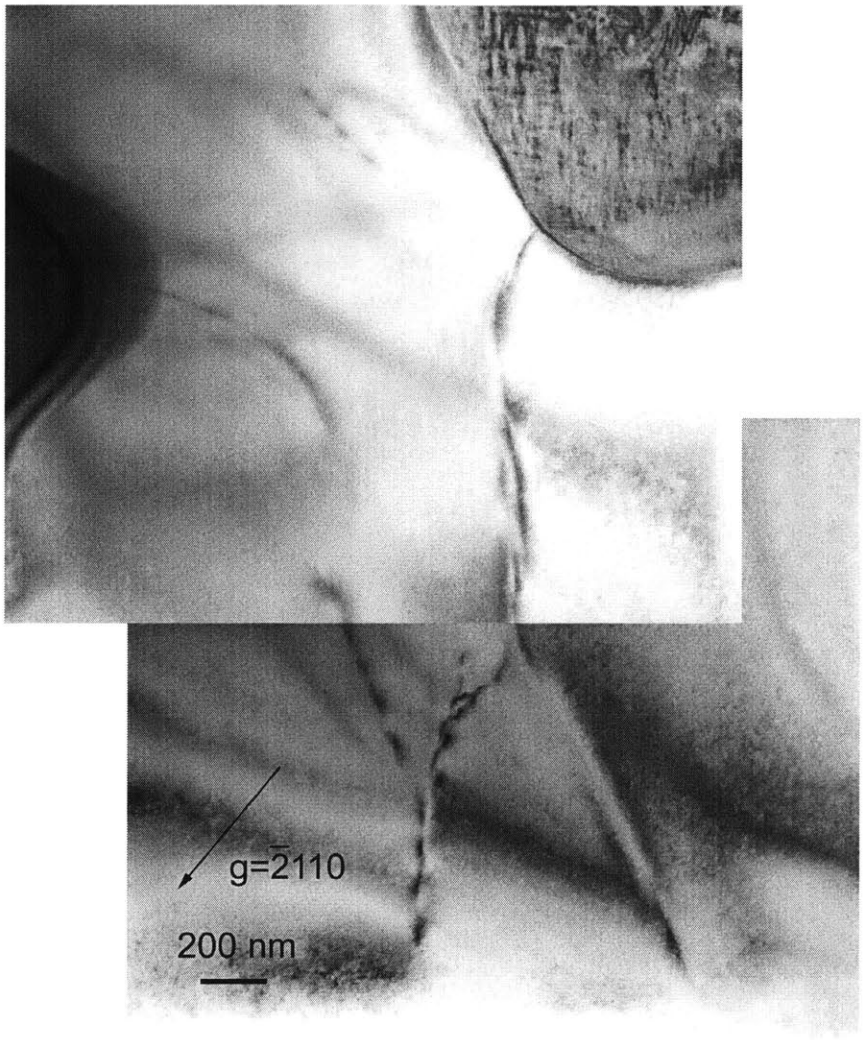

Figure 5-9: Dislocation in lower part of Fig 5-6 under operating reflection of $\{\bar{2}110\}$.

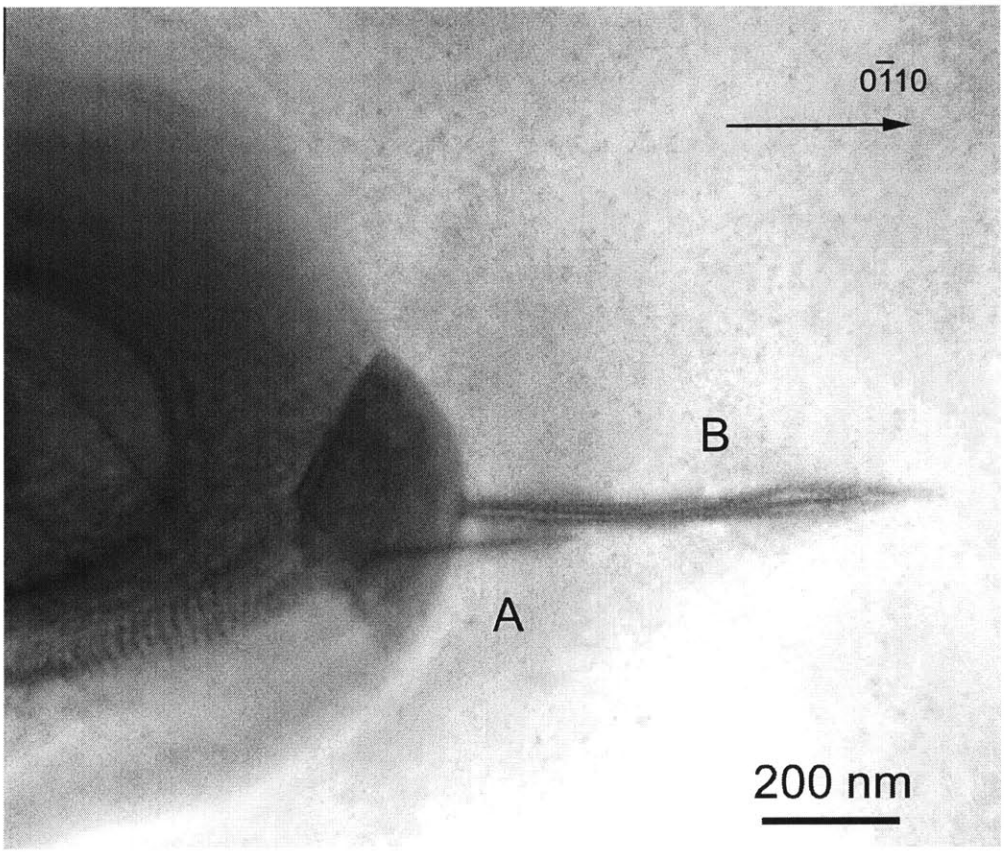

Figure 5-10: A pair of dislocation attached to a phase boundary.

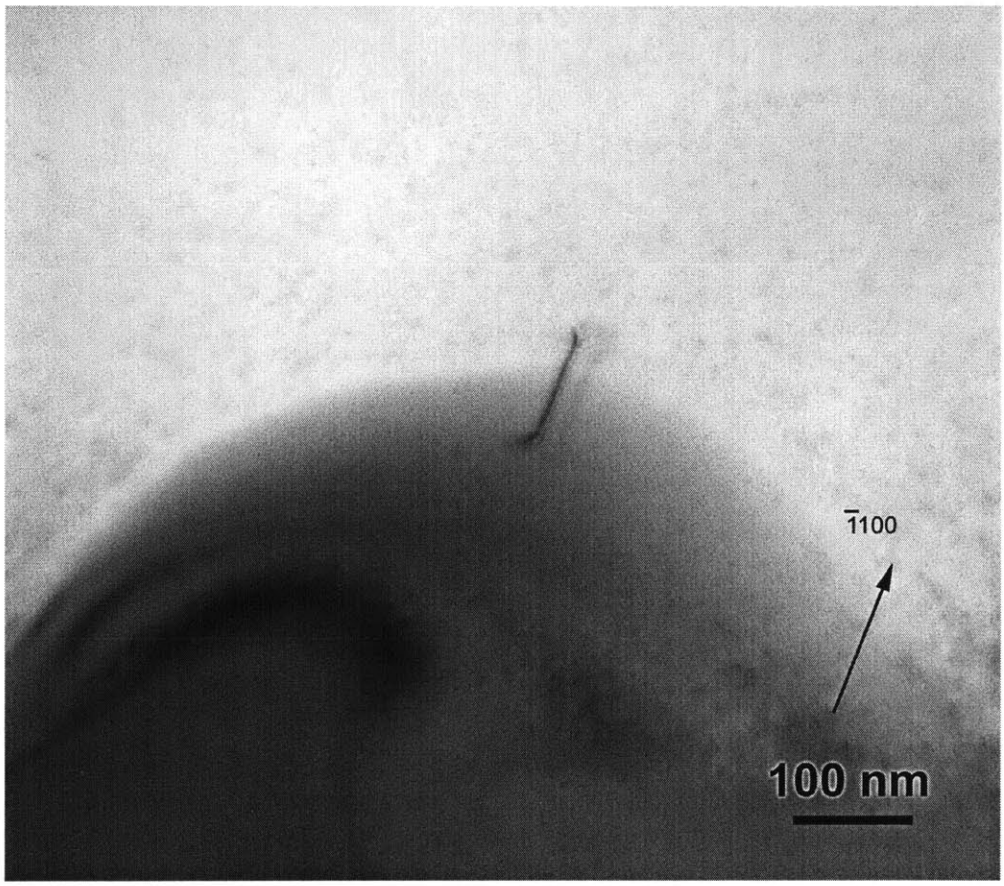

Figure 5-11: A single segment of dislocation attached to a phase boundary.

domains, as well as the the particular structure of the interfaces. In the close-up bright-field electron micrograph, one set of dislocation has thick line contrast, while the other set has thin line contrast existing between the 'thick' dislocations. These two sets were identified as dislocations with pyramidal type Burgers vector of $1/3[\bar{1}101]$ ('thick') and $1/3[0\bar{1}11]$ ('thin').

5.5 Discussion

The presence of basal dislocations is well expected. The pole figure of as-grown specimen shows a very sharp texture of [0001] along the growth axis (Dickey [2002]). However, there is still a small portion of [0001] orientations deviating from the growth c-axis which was also the direction of applied tensile stress. For a 1° misorientation, the resolved shear stress on the basal plane could be as high as 2 MPa. This stress should be sufficient to active basal slip in sapphire (Firestone and Heuer [1976]). The deviation could be enough to cause enough shear stress to active the basal slip system in Al_2O_3. Another evidence of [0001] off growth axis is the low angle boundary form by two sets of pyramidal dislocations found in crept specimen foil, which indicates that there possibly are [0001] orientations deviation from growth axis in some colonies. The observations in crept [0001] orientated sapphire by Firestone and Heuer [1976] has indeed reported that there was a high density of basal dislocations present in the TEM foil. Firestone and Heuer [1976] attributed the presence of such basal dislocations to the misorientation of the specimen from the ideal [0001] orientation and the motion of nonbasal dislocations which through reactions could generate basal dislocations. One case of such dislocation reaction generating basal dislocation was observed by Price [1960] during in situ deformation of 0° Zn foils in the electron microscope, where $1/3 < 11\bar{2}3 >$ Burgers vector dislocations were being generated. As they moved through the foil, they dissociated via the reaction

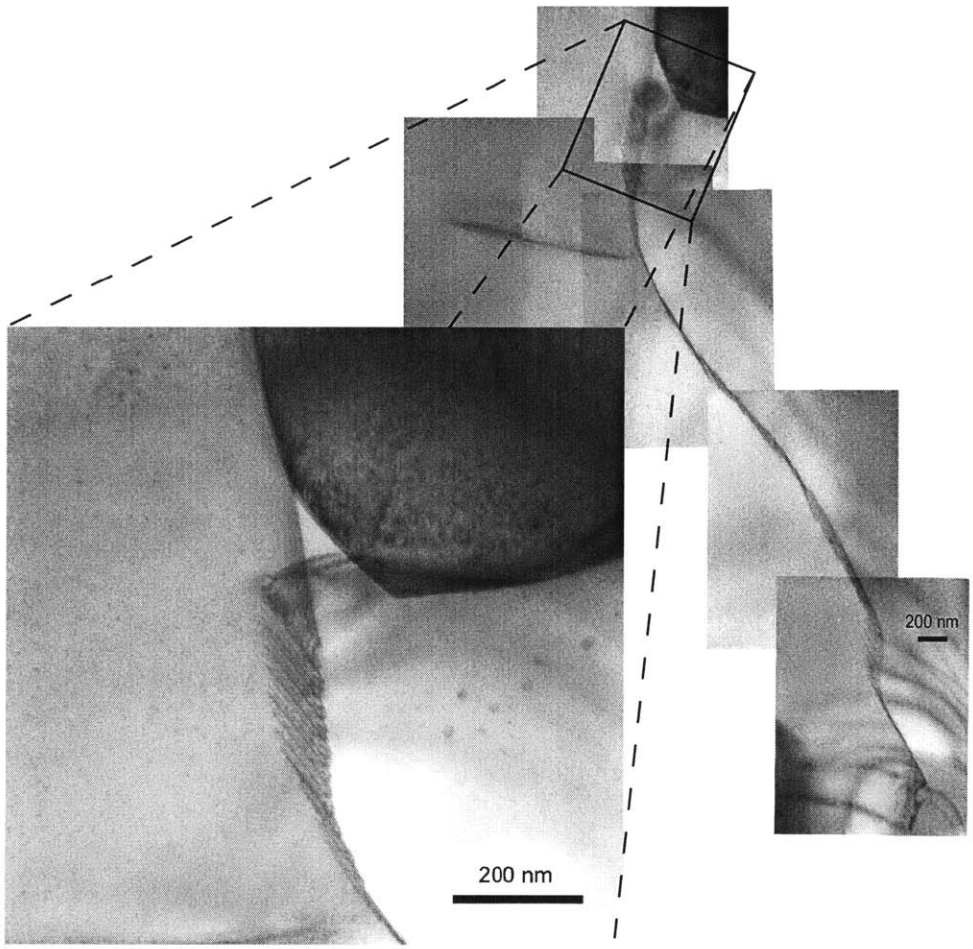

Figure 5-12: A low angle asymmetrical tilt boundary and the closer view of its upper part.

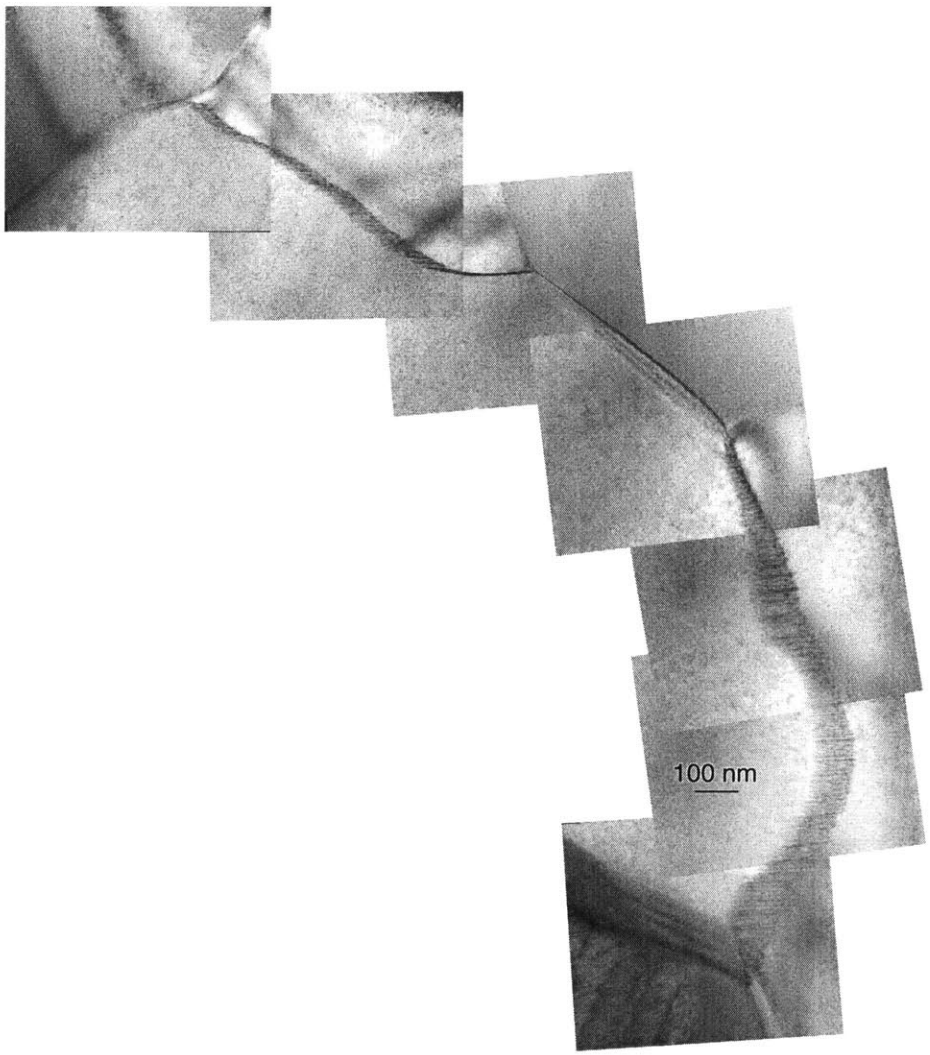

Figure 5-13: Another low angle asymmetrical tilt boundary in Al_2O_3.

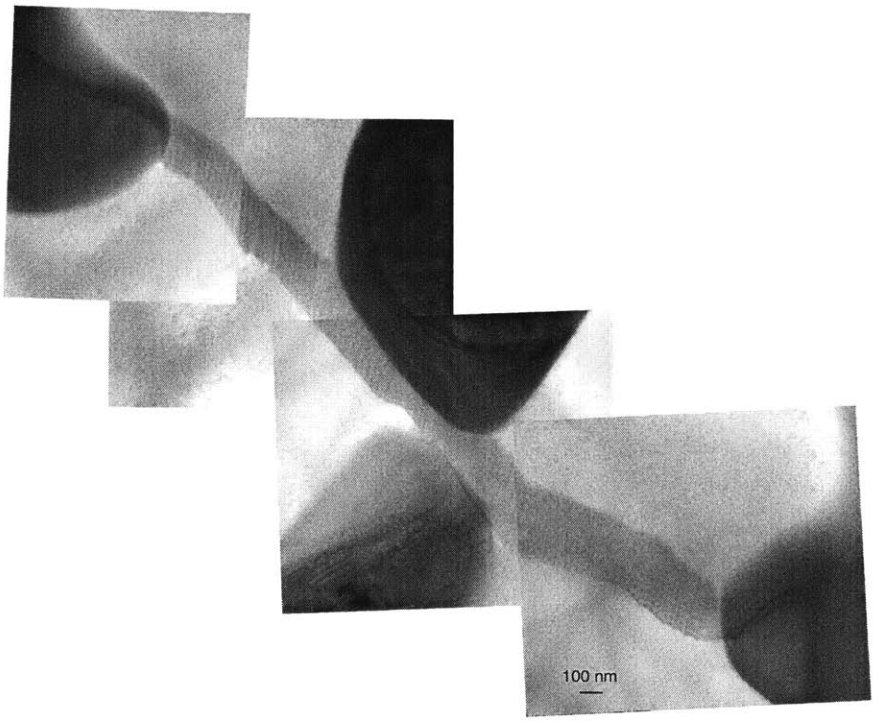

Figure 5-14: Another low angle asymmetrical tilt boundary in Al_2O_3.

$$1/3[\bar{1}\bar{1}23] = 1/3[\bar{1}\bar{1}20] + [0001] \quad (5.1)$$

and formed nodes and loops. Firestone and Heuer [1976] also pointed out that the basal dislocations formed by glide in sapphire may be rapidly immobilized by node formation. Their TEM observations show these sessile nodes formed between basal and nonbasal dislocations.

There is a large fraction of dislocations being of $1/3 < \bar{1}101 >$ pyramidal type Burgers vector present in the crept specimen. According to Table 5.2 these dislocations could possibly be on pyramidal or prismatic planes. Since in the tensile creep experiment the prismatic plane is unstressed, these dislocations belong most likely to the pyramidal dislocation set. Chang *et al.* [2003] and Bodur *et al.* [2004] demonstrated by a MD simulation of the sapphire pyramidal dislocation core structure that this type of dislocation should be entirely sessile for glide. So, climb becomes the only mode by which these pyramidal dislocations can move through the specimen within the Al_2O_3 domain and produce creep strain, given the deformation is isolated within each phase. As will discuss in Chapter 6, a feature the creep model used to explain the larger than 3 power of the stress exponent in the strain rate expression was the proposal that dislocations of the Al_2O_3 domains need to bow around the impenetrable c-ZrO_2 domains. The two micrographs of Fig 5-5 provide some support of this hypothesis, showing partially bowed out segments of pyramidal dislocations traversing the gap between the c-ZrO_2 domains. While the curvature of the segments is slight this is explainable by the fact that the trailing portions of the Al_2O_3 dislocations could be pulled into the interfaces where their energy might be lowered by the different elastic stiffnesses of the c-ZrO_2 domains. This effect is also, most likely, the basic reason why few Al_2O_3 dislocations in the crept material were found in the Al_2O_3 channels. A consideration weakening the significance of the observation of pyramidal dislocations of Fig 5-5 is that the principal planes of bow-out of these climbing dislocations should have been close to the plane of the foil while the dislocations appear to be primarily in the plane of the foil. A number of

attempts were made to obtain stereo pairs of dislocations to ascertain the spacial paths they took, such as those in Fig 5-5. None of these attempts, however, gave much useful depth perception.

Fig 5-12 is a good example showing how a low angle boundary is possibly formed. There are two sets of parallel dislocations alternatively lined up to form this asymmetrical tilt boundary. The rotation axis is in the plane of boundary and all lines are edge dislocations parallel to the rotation axis. These low angle tilt boundaries are most likely to be formed during creep deformation to accommodate the plastic deformation caused by pyramidal dislocation climbing within each columnar colony.

Fig 5-6 shows an area where the low angle boundary might be generating. There are basal dislocations and pyramidal dislocations. From the node shown in the figure, like the one between A, B and C, a possible dislocation reaction could be figured out as

$$1/3[0\bar{1}11] + 1/3[\bar{1}2\bar{1}0] = 1/3[\bar{1}101]. \tag{5.2}$$

Gooch and Groves [1973] have observed a similar reaction of the type

$$1/3[\bar{1}101] + 1/3[2\bar{1}\bar{1}0] = 1/3[10\bar{1}1] \tag{5.3}$$

Moveover, as pointed out by Firestone and Heuer [1976], nodes could have formed by these reactions between basal and nonbasal dislocations, making these dislocation nodes sessile. In the eutectic, it is possible that the basal dislocations in Al_2O_3 reacting with pyramidal dislocations to form sessile nodes. These sessile nodes could not glide but climb. Two sets of pyramidal dislocations may start to line up by climb and undergo a form of aggregation to form the low angle asymmetrical tilt boundary. Formation of A low angle boundary can be also seen in the upper part of Fig 5-2 where the arrow points at.

There are several possible sources for the dislocations in Al_2O_3. The dislocations formed in solidification can be one of them. However, since it is generally accepted that the density

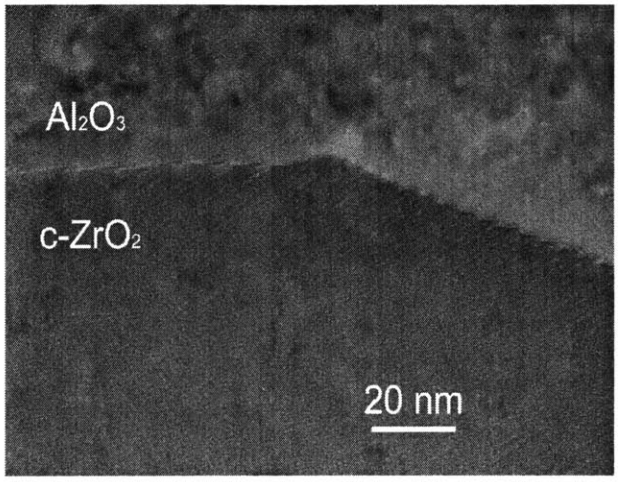

(a)

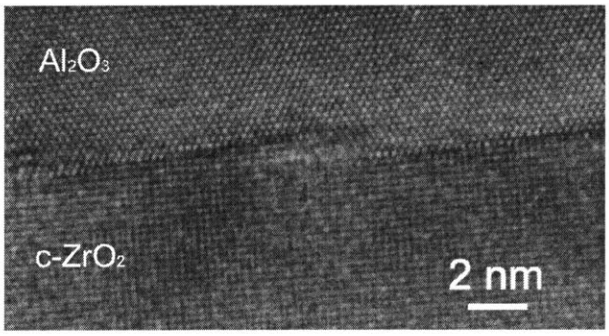

(b)

Figure 5-15: High resolution lattice images of Al_2O_3 and c-ZrO_2 interface where the serrations along the phase interfaces are clearly shown.

of growth defects are low, and there are no solidification dislocations observed in as-grown eutectic TEM foils, this is not likely to be the main source of the dislocation observed in Al_2O_3. Another dislocation source can be through the action of Bardeen-Herring sources (Hirth and Lothe [1968]), which is an analogous dislocation source of Frank-Read type operating in climb. However, no clear evidence for such sources were found in TEM. The third possibility of dislocation formation is associated with phase boundaries, as shown in Figures 5-10 and 5-11, where the dislocations are attached to the phase boundary. Since an abundant density of phase interface area per unit volume exists in the eutectic and much of this interface area is incoherent, it is likely that they might play a role in dislocation production (Yi *et al.* [2004c]). In the search for mechanisms that control the dislocation fluxes during creep various possibilities for nucleating pyramidal dislocations from interface as well as in other forms were considered here.

1. Nucleation of a pyramidal edge dislocation from an interface in the stress field of a dislocation of the c-ZrO_2 phase pressed against the other side of the interface, in a well known scenario discussed briefly in the Appendix A. The resulting activation energy ΔG^* and its dependence on the applied shear stress τ is roughly, (see Appendix A)

$$\Delta G^* \cong (\mu b_z^3)(\mu/3\tau) \tag{5.4}$$

where μ should be the average shear modulus of the two adjoining media and b_z(=0.363nm) is the Burgers displacement of the c-ZrO_2. Since pyramidal dislocations of alumina are sessile in glide (Chang *et al.* [2003] and Bodur *et al.* [2004]), this mechanism is inoperable in addition to the unrealistically large nature of the energy scale factor μb_z^3 which is of the order of 12.7 eV.

2. As a variant of the above case is the pyramidal dislocation nucleation from a basal dislocation in a climb mode, under high local vacancy mobility. The resulting activation energy expression is identical to Eq. (5.4) where, however μ is that of Al_2O_3 and

b_z is replaced with a basal dislocation Burgers displacement (=0.479nm), and finally the shear stress τ is to be replaced with the climb stress σ_1 (see Appendix A). Here the activation energy factor is nearly 45 eV, which is also unrealistically large.

3. Another possibility is the extraction of a pyramidal edge dislocation from a low angle symmetrical tilt boundary of pyramidal dislocations. Elementary analysis based on the shear stress field around a symmetrical tilt boundary gives the required shear stress τ to be

$$\tau \cong (0.25)\theta\mu, \tag{5.5}$$

where θ is the tilt angle of the boundary which is expected to be in the range of 0.05 - 0.10 giving τ to be in the range of 1 - 2% of the shear modulus of alumina. While this required stress level approaches a manageable level it would still require considerable stress concentration and requires multiplication of such torn-away dislocations by some Bardeen-Herring type dislocation climb source configuration (Bardeen and Herring [1952]).

4. Still another possibility could be emission of pyramidal dislocations from atomic size ledges on stressed stationary interfaces, as shown in Fig 5-15. A scheme of mobilization of a topological edge dislocation from a grain boundary ledge without a surrounding strain field as considered by Li [1963] would require stress levels only marginally less than the ideal shear strength as was considered in more detail by Brochard *et al.* [2001] more completely for surface ledges.

5. In all the above cases substantial additional stress concentrations would be required to bridge the gap between the prevailing nominal stresses during creep and the stresses required by the mechanisms to become operable. In this sense a more realistic possibility would be the emission of dislocations from stress concentrations due to the

arrest of sliding incoherent interfaces at larger-than-atomic size ledges where formation of climb embryos could also be assisted by condensation of vacancies. This is a variant of the intergranular cavity formation process discussed by Argon *et al.* [1980] and summarized by Argon [1982].

In summary, however, considering all the above possibilities the mode of maintenance of climb producing dislocation fluxes remains unclear.

Based on all observations of dislocations in the micrographs studied in the particular sample crept at 1400°C, the total dislocation density was $6\times10^{11}/m^2$. This is quite low in comparison with what the model in Chapter 6 may imply but might be explainable by the various possibilities of dislocation loss to interface and foil surface, as well as the difficulty in foil preparation.

Chapter 6

Dislocation Model of Al_2O_3/c-ZrO_2(Y_2O_3) Steady State Creep

6.1 Basic Assumptions

The fact that the c-ZrO_2 of considerably lower creep resistance is encapsulated everywhere by the topologically continuous Al_2O_3 with a very tight growth texture of [0001] along the axes of the directionally solidified eutectic rods indicates that steady state creep must be controlled by the Al_2O_3 phase, once any limited compliance increment due to the stress relaxation in c-ZrO_2 is complete. This suggests that the overall creep response must have the same characteristics of steady state creep in sapphire single crystals reported by Firestone and Heuer [1976], albeit with certain important added complexities derived from the presence of the c-ZrO_2 phase. A large fraction of the c-ZrO_2 has dimensions in the range of 0.2~0.4 μm and must be regarded as being too small to have the capability of undergoing plastic flow by independent internal processes of dislocation multiplication by glide or climb, as already remarked above. The c-ZrO_2 phase components of larger dimensions, as the ir-

regular shaped ones in Fig. 2-3 should undergo rapid stress relaxation in the 1200-1520°C temperature range of interest, as the transient creep curve of Fig. 4-1 suggests. Even so, as presenting in Section 6.3, FEM analysis shows that complete shear stress relaxation in the c-ZrO_2 still leaves the mean normal stress in it intact which prevents large average stress enhancement in the Al_2O_3 phase.

Since the best slip systems of the basal and prismatic type are largely unstressed in the Al_2O_3 phase for glide due to its tight texture, and since the pyramidal dislocations of $1/3 < \bar{1}101 >$ type are sessile in glide, due to a unique core restructuring process as has been recently demonstrated (Chang *et al.* [2003] and Bodur *et al.* [2004]), it is expected that creep in this component for eutectic fibers in tension, can only be a consequence of climb of the $(1/3) < \bar{1}101 >$ dislocations, whether they exist on the prism planes or on the pyramidal planes. This has already been recognized by Firestone and Heuer [1976] and is confirmed by the TEM observations in Chapter 5. Nabarro [1967] has presented an idealized model of creep derived from climb of dislocations of a Frank type network where material fluxes are between the actual climbing dislocations with Burgers vectors parallel to the stress axis and those of other types experiencing no climb forces. Firestone and Heuer [1976] found reasonable agreement of their results where the stress exponents were in the range of 3 as the Nabarro model predicts. In the case of this thesis research where the stress exponents are in the range of 4.5~6.0 it is expected that different conditions, requiring considerable modification of the Nabarro framework.

The TEM observations show that the $(1/3) < \bar{1}101 >$ dislocations might pre-exist in the Al_2O_3 phase, having been generated during the directional solidification process while the morphology is being established or can be formed from the phase interfaces, and will multiply by topological convolution processes in well known ways from sources, and will be available for climb under stress during creep as discussed in section 5.5. It is expected that the mean free path lengths of climbing dislocations in Al_2O_3 will involve several multiples of the interphase dimensions, i.e. be of the order of microns, requiring the

climbing dislocations to repeatedly bow and straighten-out as they thread through the small c-ZrO_2 domains that will remain impenetrable to them. Such repetition of transient line shapes will be viewed as the primary source of the elevation of the creep stress exponents to become larger than 3 (Li [1968]). It is assumed that the climbing pyramidal dislocations can multiply by topological processes (Bardeen and Herring [1952]). As for the climb of these dislocations, it is assumed that this will be diffusion controlled with adequate jog concentrations being present along the dislocations. It is expected to these jogs to be produced by nodal emission processes from network junctions rather than being of a thermal equilibrium nature which preliminary analysis show to be far too difficult. It is assumed that the diffusional transport will be between dislocation cores and the large concentrations of incoherent or semi-coherent interfaces, and along these interfaces. It is assumed also that the interfaces will be completely opaque to the transmission of dislocations from c-ZrO_2 to Al_2O_3 or vice versa. Analysis indicates that such transmission would be subject to extremely large energy barriers, that can not be overcome. It is expected that the residual stresses due to initial thermal misfit between the components will be relieved during the transient phases of the creep and provide another contribution to the recorded amounts of extension shown in Fig. 4-1, but that steady state creep will be governed by the climb forces resulting entirely from the applied stress.

Finally, it is expected that as the topologically continuous framework of the Al_2O_3 creeps and extends, while the c-ZrO_2 largely remains either dormant or is merely stress-relaxed, global back stresses will develop in the Al_2O_3, gradually slowing down the creep rate (Brown and Stobbs [1975]). Since the creep ductilities of the eutectics are quite modest, it is not expected this back stress to develop fast enough to be of consequence, and ignore it.

6.2 The Creep Rate

Consider a round tensile creep bar of an Al_2O_3/c-ZrO_2 eutectic as sketched in Fig. 6-1 where local axes 1, 2, 3, are chosen in a pyramidal glide system with axis 1 chosen parallel to the $1/3 < \bar{1}101 >$ Burgers vector, axis 2 normal to the pyramidal plane making an angle ϕ with the bar axis, and axis 3 parallel to the line vector of a positive edge dislocation. Under a uniform stress σ_1 a positive edge dislocation will climb in the negative 2 direction with a velocity v_c to contribute to a uniaxial tensile creep strain rate parallel to the 1 direction. This velocity, if it were governed by diffusion controlled climb would be given by Friedel [1964] (see Appendix E for the derivation)

$$v_c = \frac{2\pi D(\sigma_1 - \sigma_T)b^2}{kTln(r_s/r_c)} \tag{6.1}$$

where $D = D_0 exp(-Q/RT)$ is the diffusion constant of Al_2O_3 where oxygen is recognized to be the slow diffusing species, σ_T is the triaxial component of the applied stress ($= \sigma_z/3$) that does not promote equilibrium climb, r_s is the distance from the dislocation core to vacancy sinks along the interfaces, r_c the core radius from which point defect emission is considered, b the magnitude of the Burgers vector, D_0 the pre-exponential factor of the diffusion constant, Q the activation energy of O ion diffusion in Al_2O_3 and R and T have their usual meaning. The kinematics of shape change due to climb alone of dislocations has been considered more broadly by Groves and Kelly [1969]. In the case of this thesis research a more specialized consideration will be adequate. Thus, considering that there will be three equivalent pyramidal systems that can contribute to the axial strain rate equally, as is explained in the Appendix B, the axial creep strain rate $\dot{\epsilon}_z$ along the bar and the accompanying radial contractile strain rates $\dot{\epsilon}_r$ are given respectively as:

$$\dot{\epsilon}_z = (2 - 3cos^2\phi)\dot{\epsilon}_0 \tag{6.2}$$

and

$$\dot{\epsilon}_r = -(1 - \frac{3}{2}cos^2\phi)\dot{\epsilon}_0 \tag{6.3}$$

where

$$\dot{\epsilon}_0 = b\rho_m v_c \tag{6.4}$$

is the main local creep rate in the pyramidal system coordinates without regard to overall volume preservation, which is considered to result in Eqs 6.2 and 6.3 (see Appendix B). Relating the actual climb-producing tensile stress σ_1 to the axial stress σ_z and considering the volume-average effect of the local variation of stress due to the presence of the c-ZrO_2 components by a factor (see below) q then

$$\sigma_1 - \sigma_T = \frac{2}{3} q \sigma_z (1 - cos^2\phi) \tag{6.5}$$

If the mobile dislocation density, ρ_m, of climbing dislocations at steady state is governed by mutual interactions in a self adjusting basis (see Appendix F for the derivation); i.e.

$$\rho_m \cong (\frac{2\pi\sigma_z}{\mu b})^2 q^2 (1 - cos^2\phi)^2 \tag{6.6}$$

by finally combining Eqs (6.6), (6.2), (6.5) and (6.6) the axial steady state creep strain rate:

$$\dot{\epsilon}_z = A(\frac{D}{b^2})(\frac{\sigma_z}{\mu})^3(\frac{\mu\Omega}{kT})\frac{(1 - cos^2\phi)^3(2 - 3cos^2\phi)}{ln(r_s/r_c)} \tag{6.7}$$

where

$$A = \frac{2}{3}(2\pi)^3 \frac{q^3}{\beta} \tag{6.8}$$

and

$$\beta = \Omega/b^3 = 0.079 \tag{6.9}$$

where Ω is the ionic volume of oxygen in the Al_2O_3 lattice and q is a factor which relates the local volume average climb stress to the axial stress σ_z as is determined from a FEM analysis of the stress distribution in the Al_2O_3 phase under an applied tensile stress as discussed in Section 6.3 below.

Eq. 6.7 gives the creep rate due to the climb of quasi-straight dislocations in a homogeneous stress field. As discussed in Section 6.4 this is not the case in the Al_2O_3/c-ZrO_2

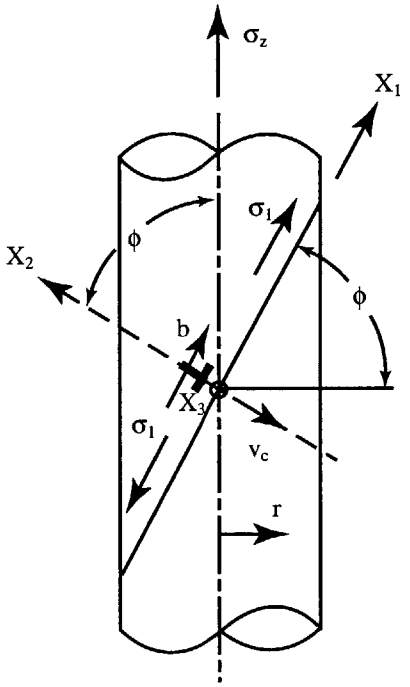

Figure 6-1: Sketch of a round bar of a Al_2O_3/c-ZrO_2 eutectic with z axis parallel to the [0001] direction of the Al_2O_3. The plane at angle ϕ outlines a pyramidal glide plane. A local tensile stress σ_1 will make a positive edge dislocation climb in the negative X_2 direction.

eutectics where the climbing dislocations need to thread through the non-deforming c-ZrO_2 domains acting as dispersoids and are required to alternately bow around these domains and be released to straighten out, acting effectively as if straight dislocations were moving through a strongly varying internal stress field which will increase the stress exponent in predictable ways and decrease the actual creep rate (Li [1968]).

6.3 Distribution of Stresses in the Eutectic Al_2O_3/c-$ZrO_2(Y_2O_3)$

A very important way in which creep in the eutectics differs from creep in single crystal sapphire is that in the former the stresses are distributed in a complex manner. In addition to residual stresses arising from the different thermal expansions of the two components, the applied stresses result in complex internal local stress distributions due to different elastic properties of the Al_2O_3 and the c-ZrO_2 component phases. Thus, to develop some necessary understanding of this phenomenon on a broad basis, a linear-elastic FEM analysis was carried out in a 2-D plane strain setting of the eutectic in the ordered regions of Fig. 2-2. Here the c-ZrO_2 domains in 2-D are taken as elliptical cylinders occupying a volume fraction of 0.33, shown in RVE (representative volume element) of Fig. 6-2 (See Appendix C for the derivation of the geometry of RVE). The chosen representative computational volume is indicated in this figure. It has been considered the c-ZrO_2 to be always fully relaxed of all shear stresses but with an unrelaxed appropriate bulk modulus of 83GPa. This is accomplished operationally in the FEM code for purely elastic behavior by choosing the Young's modulus as 0.05MPa and the Poisson's ratio as 0.4999999. All other chosen material constants are listed in Table 6.1. In the broader analysis it is considered the aspect ratios of ellipsoidal rods, a/b of c-ZrO_2 as 1,3,4 and 5. Of these results it is presented here only the distributions for $a/b = 3.0$ as most representative. All analyses were limited to the elastic range. In this FEM framework it is considered several process simulations: a) an applied tensile stress σ_z alone; b) cooling the morphology from a stress-free condition at

1875°C down to 1400°C to determine residual stresses among components and; c) cooling as in (b) plus an applied tensile stress of σ_z = 300MPa. Of these, it is discussed here only the case of the internal stress distribution under an applied stress σ_z = 300MPa (Since behavior is linear-elastic, results for all other stress levels can be determined by re-scaling).

Fig. 6-3a shows the distribution of the Mises deviatoric stresses for the case of σ_z = 300MPa and T=1400°C[a], in the Al_2O_3 region. As expected, the states of stress inside the ellipsoidal regions of the c-ZrO_2 are close to constant. Figure 6-3b gives the more important distribution of the climb stress σ_1, parallel to the pyramidal dislocation Burgers vector at an angle of $\phi = 57.7^o$ as shown in Fig. 6-1. The volume-average level of this important climb producing stress was found to be σ_1 = 216.3MPa which gives the factor q to be 0.721. This value appears surprisingly low in view of the assumed complete relaxation of the deviatoric stresses in the c-ZrO_2, until it is recognized that the c-ZrO_2 still supports fully a mean normal stress which limits the stress enhancement in the Al_2O_3 component. Table 6.2 lists this volume average resolved climbing stress acting on pyramidal system in Al_2O_3 by different aspect ratios and under three processes mentioned above. The thermal stress and different geometries only have minor influence on the volume average resolved climbing stress, which is major stress consideration in the mechanistic model.

6.4 Effect of Internal Resistance Variations

As stated in Section 6.2 the creep response of the Al_2O_3/c-ZrO_2 eutectics differ significantly from the creep behavior in homogeneous sapphire single crystals studied by Firestone and Heuer [1976]. First because of the non-uniform stress distribution in the morphology of Al_2O_3 and c-ZrO_2 discussed in Section 6.3 above but even more importantly by the large perturbations that the climbing dislocations encounter threading through the isolated and largely non-deforming c-ZrO_2 domains. Thus, consider the convolutions that a climbing

[a]See Appendix D for more results of stress distribution FEM simulation.

Table 6.1: Material Properties for Linear Elastic FEM Analysis

	Al_2O_3	c-ZrO_2
Young's Modulus	190GPa at 1400°C	0.05MPa at 1400°C [a]
Poisson's ratio	0.3	0.4999999 [a]
Yield Stress	5.0GPa [b]	5.0GPa
Coefficient of Thermal Expansion, $°C^{-1}$	9.1×10^{-6} (a) 9.9×10^{-6} (c) (Dickey *et al.* [1999])	12.9×10^{-6} (Dickey *et al.* [1999])

[a]These values were chosen in the FEM code result in a negligible shear modulus for c-ZrO_2 to obtain a state of near complete shear relaxation while leaving the bulk behavior intact.

[b]These high yield stresses were chosen in the FEM code to guarantee pure elastic response.

Table 6.2: Volume Average Resolved Climbing Stress Acting on Pyramidal System in Al_2O_3

Aspect Ratio	a/b=3	a/b=4
Applied Stress (300 MPa @ 1400°C)	216.35 MPa	206.7 MPa
Thermal Stress		
1875°C -> 1400°C	17.668 MPa	26.65 MPa
Thermal and Applied Stress		
1875°C -> 1400°C then 300 MPa	235.0 MPa	234.4 MPa

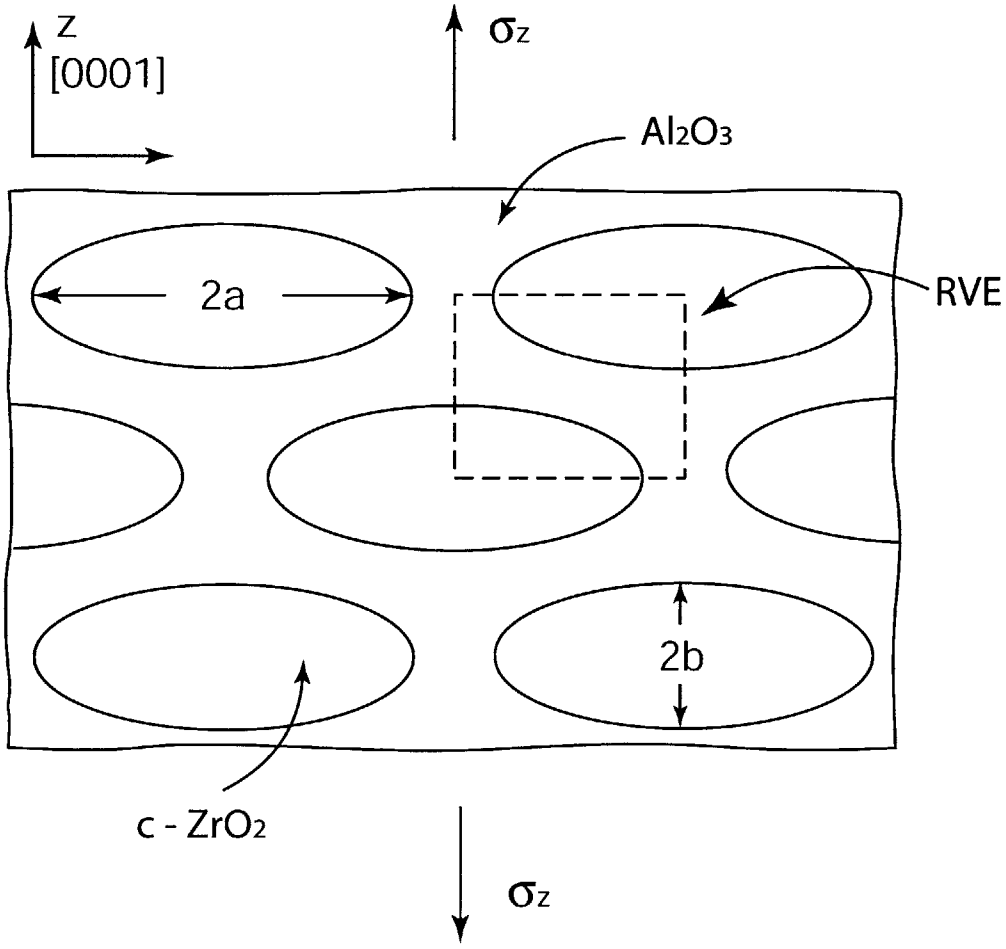

Figure 6-2: Sketches of an idealization of the c-ZrO_2 domains as ellipsoidal cylinders in the topologically continuous Al_2O_3 component, for the purpose of a FEM study of the internal stress distribution in the Al_2O_3 when a tensile stress σ_z is applied.

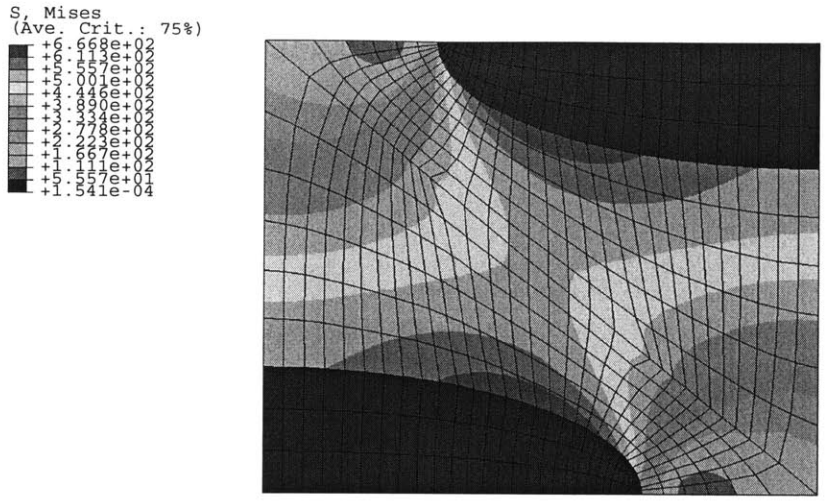

(a)

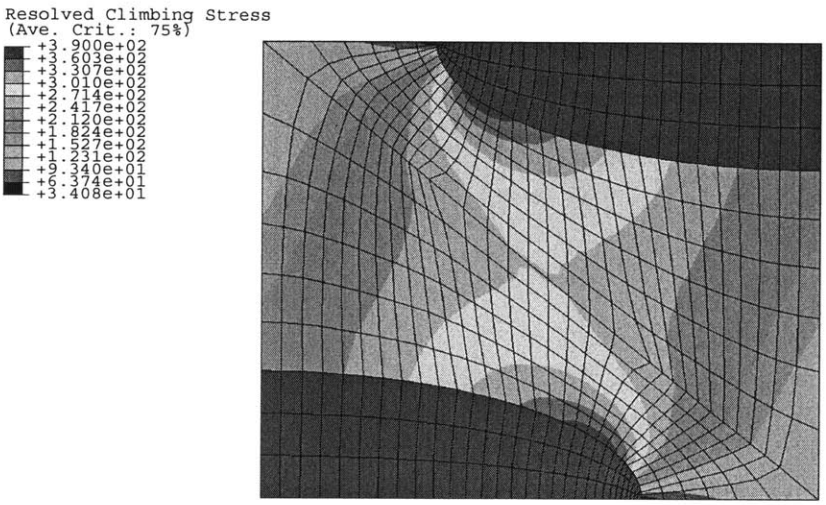

(b)

Figure 6-3: Stress distribution results of the FEM study; a) deviatoric (Mises) stresses in the two components of the eutectic; b) the distribution of the climb stress σ_1 in the Al_2O_3.

dislocation has to go through as it threads through the gaps of the c-ZrO_2 domains as depicted in Fig. 6-4. First, the climbing dislocation must squeeze into the gaps between the domains as depicted in Fig. 6-4a to a critical configuration much like the Orowan bowing process for non-shearable dispersoids. The peak stress that is required for this configuration to be achieved is

$$\sigma = \sigma_i = \frac{2\mathcal{E}}{b\Lambda} = \frac{\mu b}{\Lambda} \tag{6.10}$$

where $\mathcal{E}$ is the dislocation line tension ($= \mu b^2/2$) and Λ is the size of the inter-domain gap. Clearly, here the process is not one of glide but climb where σ is the climb stress. Once the critical configuration is reached and the climbing dislocation surrounds the impenetrable domain and pinches off as shown in Fig. 6-4b, the separated dislocation has acquired a definite cusp where this shape of the dislocation will undergo accelerated climb due to the advantageous line tension effects. These required contortions of the dislocations can be viewed as if they were the same as positive and negative internal stresses σ_i, retarding and then accelerating climb, very much like the corresponding cases of favorable and unfavorable internal stresses that a glide dislocation needs to go through between dispersoids. Such problems were treated in great detail by many investigators, but particularly thoroughly by Li [1968], which illustrated that a gliding dislocation (in the case of this thesis research a climbing dislocation) loses more time in the region of adverse internal stress than the time it gains in moving through regions of favorable internal stress. The effect is illustrated in Fig. 6-5 where Fig. 6-5a shows the sinusoidally varying internal stress σ_i and the prevailing climb stress σ. The most important consequence of such deceleration and acceleration of dislocation motion is an increase in the effective stress exponent m of the dislocation velocity, scaled by the ratio of σ_i/σ is shown in Fig. 6-5b. A secondary effect is a factor $C = \bar{v}/v$ that gives the decrease in the average dislocation velocity relative to the velocity in unhindered climb shown in Fig. 6-5c, also scaled with the ratio of σ_i/σ. To assess a measure of the effect, note from Fig. 2-2 that in much of the morphology the inter-domain distance

Λ would appear to be between 0.5~2.0μm. Taking the small dimension to determine the maximum level of this effect, together with $b = 5.12 \times 10^{-10}$ m and $\mu = E/2(1+\nu) = 73$ GPa (Wolfenden [1997]) at 1400°C, $\sigma_i = 125$ MPa can be determined. This, for an applied stress $\sigma_z = 300$ MPa, in the range of interest, that would give a volume average climb stress $\sigma = q\sigma_z(1 - cos^2\phi)$ of 153 MPa, and a ratio $\sigma_i/\sigma \approx 0.815$, Fig 6-5b indicates that the effective exponent of the stress in the velocity expression should increase to nearly $m = 3$ from unity as the maximum effect. Moreover, Fig. 6-5c gives $C = \bar{v}/v = 0.6$. Clearly, larger distances Λ should result in smaller effective internal stresses while smaller applied stresses should give increased ratios σ_i/σ. The overall net effect will be rather complex to assess. Here, it is considered that, under the conditions described, the net effect on the overall stress exponent of the creep rate will be to elevate it from $n = 3$ for the model presented above to $n = (m + 2) = (2.5 + 2) = 4.5$ to $n = (3 + 2) = 5$. This consideration and the factor C, when incorporated into the creep model of smooth climb given by Eq. 6.7, will change it finally to

$$\dot{\epsilon} = AC(\frac{D}{b^2})(\frac{\sigma_z}{\mu})^n(\frac{\mu\Omega}{kT})\frac{(1 - cos^2\phi)^3(2 - 3cos^2\phi)}{ln(r_s/r_c)} \tag{6.11}$$

It is this expression that will compare with the experimental results in Section 6.5 below.

6.5 Evaluation of the Creep Model

The final creep model of Eq. 6.11 is now to be evaluated and compared with experimental results. In the comparison the expression for both 1400°C and 1520°C will be evaluated. The following model parameters and material properties will be used here:

$\mu = \frac{E}{2(1+\nu)} = 73$ GPa at 1400°C and 63.4 GPa at 1520°C (Wolfenden [1997])

$b = 5.12 \times 10^{-10}$ m

$\Omega = 1.06 \times 10^{-29}$ m^3

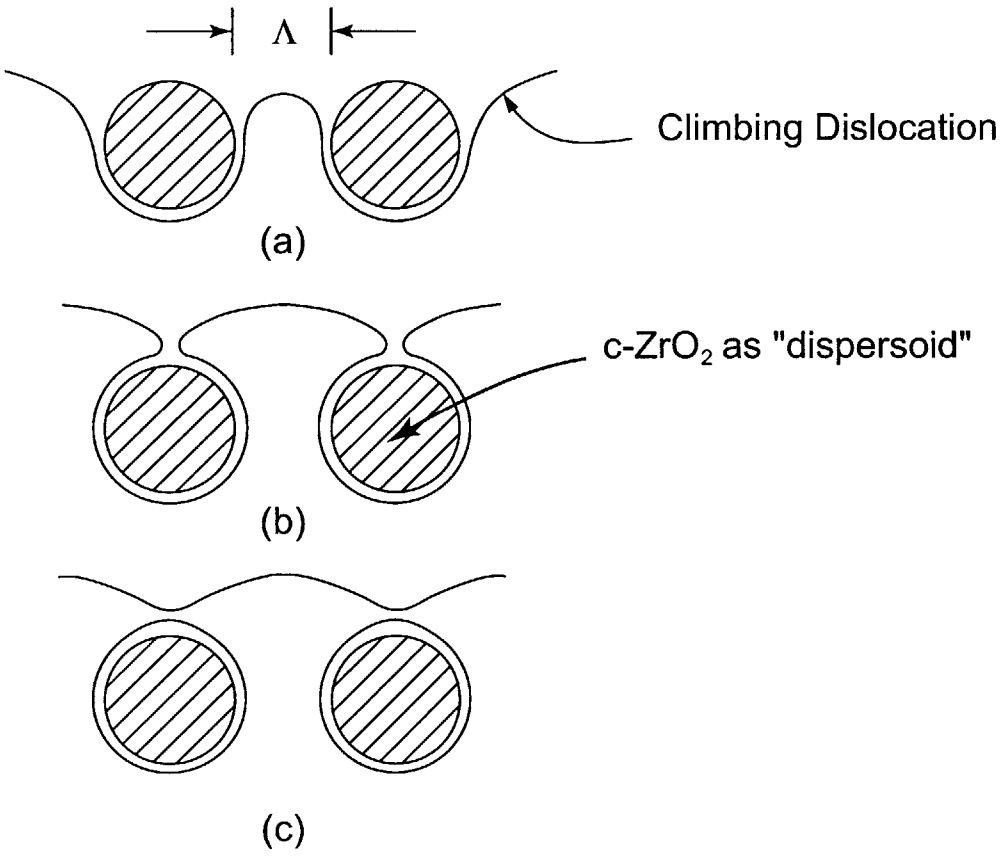

Figure 6-4: Sketch depicting the required contortions that a climbing edge dislocation need to suffer in bowing through the gaps between the c-ZrO_2 domains that consider to be impenetrable: a) critical climb configuration to bow through the gap between two c-ZrO_2 dispersoids at a spacing Λ; b) at the point when the climbing dislocation is just about to pinch off; c) the cusped dislocation line straightening out under the application of line tension.

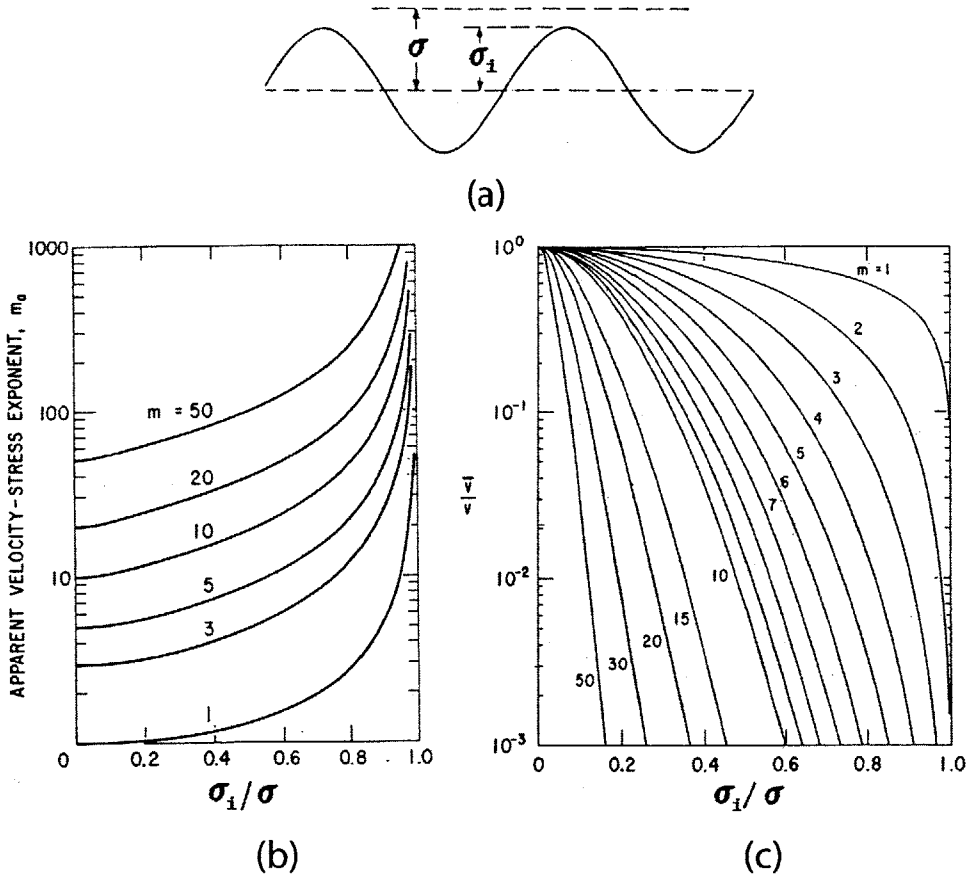

Figure 6-5: Consequence of the repeated bowing out and straightening of the climbing dislocation considered as a set of internal resistance σ_i alternately retarding and speeding up the climbing dislocation: a) retardation and speeding up considered as unfavorable and favorable internal stresses σ_i in the presence of a climb stress σ; b) effect of σ_i/σ on the overall stress exponent m of the dislocation velocity; c) effect of σ_i/σ on the attenuation factor C on the average climb velocity. (figures reproduced from Li [1968], courtesy of J. Wiley & Sons)

$q = 0.721$ as determined in Section 6.3

$\beta = \Omega/b^3 = 0.079$

$A = \frac{2}{3}(2\pi)^3(q^3/\beta) = 7.85 \times 10^2$

$\phi = 57.7^o$

$r_s = 0.5 \sim 2.0$ μm, as estimated from micrographs (Fig. 2-2)

$r_c \approx b$

$D = 10^{-14}$ cm^2/sec at 1400°C and 9×10^{-14} cm^2/sec at 1520°C determined from Oishi and Kingery [1960] directly for their polycrystalline material for which, parenthetically the activation energy was $Q = 441$ kJ/mol, considerably larger than the value in this thesis research.

$n = 4.5$ is taken as suggested from the analysis in Section 6.4

$C = 0.6$.

The calculated steady state creep relations for 1400°C and 1520°C are presented in Fig. 6-6 as the broken lines in comparison with the experimental data.

Considering the several uncertainties in the model and material parameters, the agreement between model and experimental results is pleasing, more so in the relative order of the creep rates and somewhat less so in the actual magnitudes (Yi *et al.* [2004a], Yi *et al.* [2004b]).

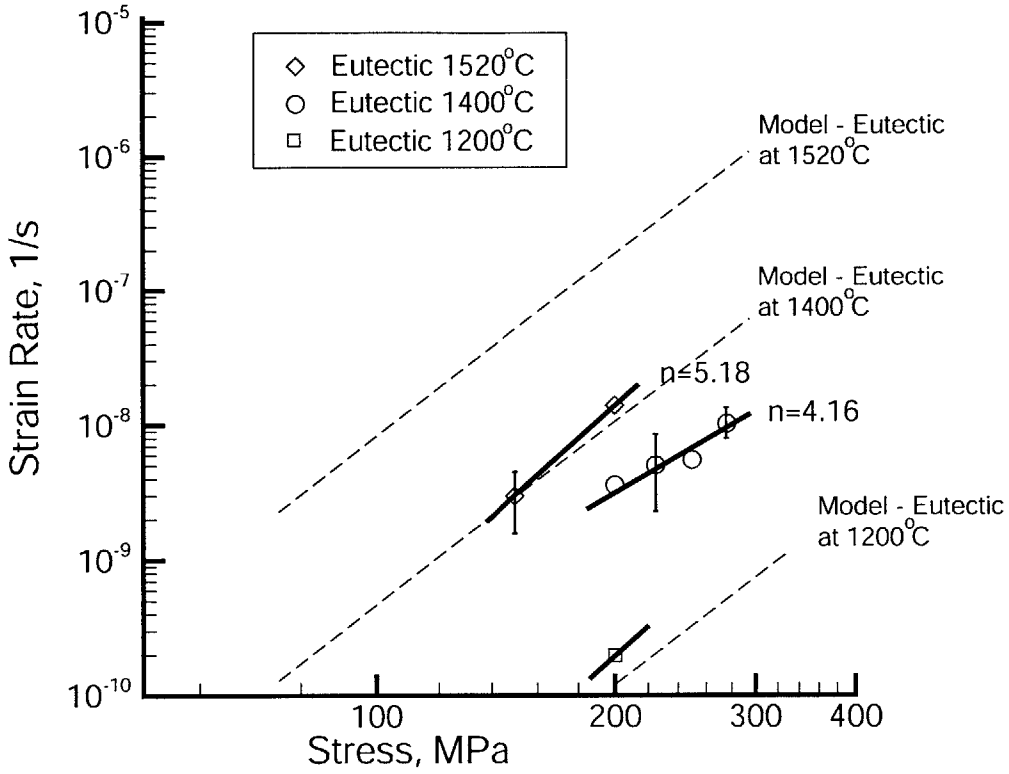

Figure 6-6: Plots of steady state creep rates as a function of stress for temperatures of 1200, 1400 and 1520°C. Broken lines represent predictions of creep model for Al_2O_3/c-ZrO_2 at corresponding temperatures.

Chapter 7

Creep Resistance of Sapphire and Eutectic Ceramics with Doping

7.1 Diffusion in Undoped Sapphire and Doped Sapphire

Diffusion controls the kinetics of many processes in ceramics such as solid-state reactions, sintering, grain growth, and creep. Measuring and understanding oxygen diffusion in $\alpha-Al_2O_3$ (undoped sapphire) is a problem of long standing in ceramic science. The oxygen self-diffusion process in α-Al_2O_3 that was reviewed by Heuer and Lagerlöf (1999) occurs by a vacancy mechanism. In sapphire, oxygen vacancies appear to be 2$\sim$2.5 times more mobile than oxygen interstitials, whereas aluminium interstitials appear to be 10^3 to 10^4 times more mobile than oxygen vacancies (Heuer and Lagerlöf [1999]). Therefore, in undoped sapphire, the diffusion process will be dominated by oxygen vacancies because of charge neutrality. The presence of dopants (in many cases, impurities), especially those aliovalent species such as Ti^{4+} and Mg^{2+}, will change the concentration of defects (Reddy and Cooper [1982]; Lagerlöf *et al.* [1989]; Haneda and Monty [1989]; Heuer and Lagerlöf [1999]; Lagerlöf and Grimes [1998]). The presence of these divalent or tetravalent dopants in greater abundance will decide whether oxygen vacancies and aluminum interstitials, or oxygen interstitials and

aluminium vacancies will dominate the oxygen and aluminium diffusion.

Figure 7.1 by Heuer and Lagerlöf [1999] shows the oxygen diffusion data for undoped sapphire from many researchers and sapphire doped with either 500 at. ppm MgO or 600 at. ppm TiO_2 by Lagerlöf *et al.* [1989]. The diffusion data from various researchers in the period of 1980~1996 shown in this figure, even with variations to some degrees, are more or less within an order of magnitude. This variation is expected (Heuer and Lagerlöf [1999]) because of 1) experimental difficulties; 2) several different techniques employed in these studies; 3) the diverse origins of sapphire used; 4)different impurities levels. The effects of dopants, such as in this case Ti^{4+} and Mg^{2+}, do have clearly measurable influences (13-50 times) on oxygen diffusion kinetics but involve only modest changes (1eV or less) in the activation energies for oxygen diffusion. For example, the experiments by Lagerlöf *et al.* [1989] show that the addition of 500ppm of MgO elevates the diffusion constant of sapphire by a factor of 40 at 1400°C and the addition of 600ppm of TiO_2 lowers it by a factor of close to 20 at the same temperature.

As described in Lagerlöf *et al.* [1989], the diffusion data for undoped, MgO-doped and TiO_2-doped sapphire can be represented as

$$D_{\text{undoped}} = (6.8^{+2.0}_{-1.5}) \times 10^{-4} \exp(-\frac{6.1 \pm 0.2\text{eV}}{k_B T})\text{m}^2\text{s}^{-1} \tag{7.1}$$

$$D_{\text{undoped}} = (4.7^{+0.3}_{-0.3}) \times 10^{-3} \exp(-\frac{5.8 \pm 0.4\text{eV}}{k_B T})\text{m}^2\text{s}^{-1} \tag{7.2}$$

$$D_{\text{undoped}} = (2.6^{+0.2}_{-0.2}) \times 10^{-2} \exp(-\frac{7.0 \pm 0.4\text{eV}}{k_B T})\text{m}^2\text{s}^{-1} \tag{7.3}$$

Analysis of these diffusion data reveals the activation energies for migration for both oxygen vacancies and oxygen interstitials are very large, 4.5-5.9 eV. Heuer and Lagerlöf [1999] suggested improved theoretical calculations were required to determine whether these values have any physical significance.

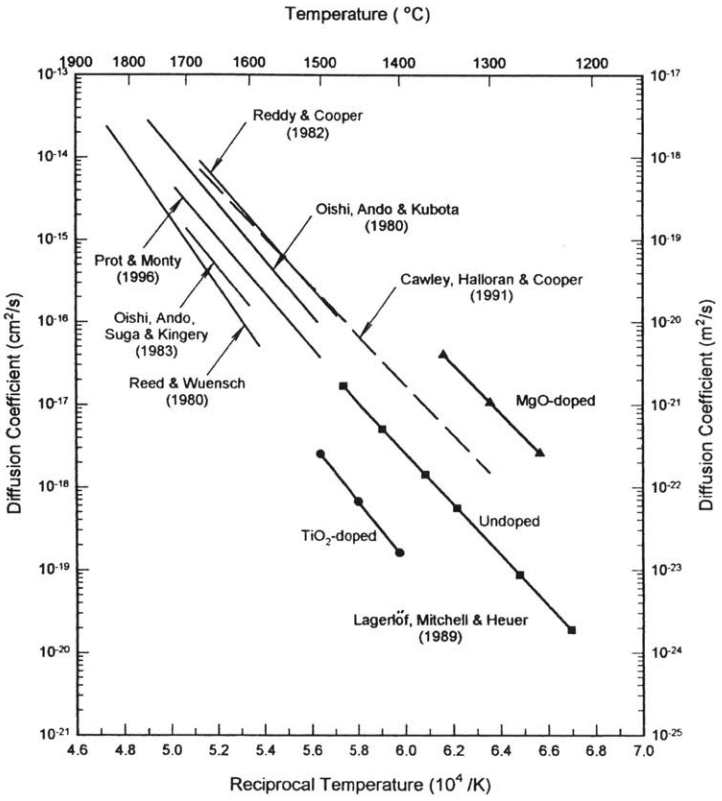

Figure 7-1: Oxygen diffusion data for undoped, MgO-doped and TiO_2-doped α-Al_2O_3 from Lagerlof *et al.* [1989], together with data for undoped α-Al_2O_3 from other researchers in period 1980$\sim$1996. See Heuer and Lagerlof [1999] for further details.

The relationship of aliovalent dopants with their effects on diffusion can be better understood through the defect chemistry (Lagerlöf *et al.* [1989]). If oxygen diffusion occurs by a vacancy or interstitial mechanism, then the Schottky, anion Frenkel, and cation Frenkel reactions must all be considered (Kroger-Vink notation is used here, Chiang *et al.* [1997]).

Schottky reaction

$$\text{null} \xrightarrow{Al_2O_3} 2V'''_{Al} + 3V^{\cdot\cdot}_{O} \tag{7.4}$$

anion Frenkel reaction

$$O^{\times}_{O} \xrightarrow{Al_2O_3} O''_{i} + V^{\cdot\cdot}_{O} \tag{7.5}$$

cation Frenkel reaction

$$Al^{\times}_{Al} \xrightarrow{Al_2O_3} Al^{\cdot\cdot\cdot}_{i} + V'''_{Al}. \tag{7.6}$$

The charge neutrality condition can then be written as

$$3 \cdot [V'''_{Al}] \cdot 2 + 2 \cdot [O''_{O}] \cdot f_O = 2 \cdot [V^{\cdot\cdot}_{O}] \cdot 3 + 3 \cdot [Al^{\cdot\cdot\cdot}_{i}] \cdot f_{Al} \tag{7.7}$$

where the number before the brackets represents the effective charge of the defect. Because the defect concentrations are defined with respect to the anion and cation sublattices, the number after the brackets represents the number of available sites per formula units; f_O and f_{Al} are respectively the number of available oxygen and aluminium interstitial sites per formula unit. The brackets represent the concentration of corresponding species.

The most likely incorporation reactions for dissolution of MgO in sapphire are

$$2MgO \xrightarrow{Al_2O_3} 2Mg'_{Al} + 2O^{\times}_{O} + V^{\cdot\cdot}_{O} \tag{7.8}$$

$$3MgO + Al^{\times}_{Al} \xrightarrow{Al_2O_3} 3Mg'_{Al} + 3O^{\times}_{O} + Al^{\cdot\cdot\cdot}_{i} \tag{7.9}$$

and another likely incorporation reaction of

$$3MgO \xrightarrow{Al_2O_3} 2Mg'_{Al} + 3O^{\times}_{O} + Mg^{\cdot\cdot}_{i} \tag{7.10}$$

The reactions of 7.8 and 7.9 both have those types of charge compensation which increase the concentration of oxygen vacancies [a]. Reaction 7.10 is self-compensating and would not affect defects on the cation and anion sublattices. Thus, it should not perturb the oxygen vacancy concentration in MgO-doped sapphire.

The most likely incorporation reactions of TiO_2 in sapphire are

$$2TiO_2 \xrightarrow{Al_2O_3} 2Ti_{Al}^{\cdot} + 3O_O^{\times} + O_i^{''} \tag{7.11}$$

$$3TiO_2 \xrightarrow{Al_2O_3} 3Ti_{Al}^{'} + 6O_O^{\times} + V_{Al}^{'''} \tag{7.12}$$

Both 7.11 and 7.12 would increase the concentrations of oxygen interstitials or aluminum vacancies, thus decrease the concentration of oxygen vacancies.

The presence of grain boundary could change the oxygen and aluminum self-diffusion behavior by acting as short circuits for diffusions through phase boundaries. Oishi and Kingery [1960] in their seminal work of oxygen self-diffusion in Al_2O_3 reported an increase of about two orders of magnitude in diffusion coefficient of oxygen in polycrystalline Al_2O_3 comparing to that of the single crystal samples. The diffusion coefficient data from Paladino and Coble [1963] also demonstrated the enhancement of oxygen ion diffusion in polycrystalline Al_2O_3.

However, in polycrystalline Al_2O_3 with doping, the dopants can preferentially segregate to the grain boundaries. The segregated ions will create a local elastic strain field within and around the grain boundary area because of the size mismatch. This contributes a significant beneficial factor to decrease the oxygen self-diffusion process. Harmer and co-workers (Cho *et al.* [2001], and Cho *et al.* [1999]) reported that p.p.m. levels of rare-earth dopant ions (e.g. Y, La, Nd) apply a beneficial and highly potent influence on the creep properties of ploycrystalline alumina, and codoping with ions of disparate sizes (Nd, Zr) resulted in even further enhancement of the creep behavior. They indicated that the dopant ions were found to strongly segregate to grain boundaries (Wang *et al.* [2000]), and there is no direct

[a] reaction 7.9 must be considered together with the cation Frenkel and Schottky disorder reactions

evidence of the influence of second phase precipitates on the creep rate. While they were not able to establish a definitive mechanism of the creep-inhibition, they proposed that those oversized segregant ions improve creep resistance by reducing the grain boundary diffusion through a site-blocking mechanism.

7.2 Creep Resistance of Undoped Sapphire and Doped Sapphire

The steady state creep model discussed in Chapter 6 is derived from a dislocation model on steady state creep of single crystal sapphire of [0001] orientation by Firestone and Heuer [1976], where the climb motion of the dislocations is expected to be quasi-smooth. Based on similar derivation, a steady state creep expression of single crystal sapphire can be given as

$$\dot{\epsilon}_{sapphire} = A'(\frac{D'}{b^2})(\frac{\sigma_z}{\mu})^3(\frac{\mu\Omega}{kT})\frac{(1-cos^2\phi)^3(2-3cos^2\phi)}{ln(r_s/r_c)} \tag{7.13}$$

where $A' = \frac{2}{3}(2\pi)^3/\beta = 2.09 \times 10^3$ (for q=1.0) and D', the diffusion constant, must be chosen for sapphire single crystals not having the benefit of diffusion short circuits along interfaces. From Oishi and Kingery [1960] one obtains $D' = 3.5 \times 10^{-17}\text{cm}^2/\text{sec}$ at 1400°C, or a factor of 3.5×10^{-3} lower than for polycrystalline material or for the eutectic with a large volume concentration of interfaces. For these alterations, but for all other factors remaining the same a steady state creep rate can be determined for sapphire crystals of [0001] orientation at 1400°C and 1500°C which is shown as the dashed line in Fig. 7-2.

Tensile creep experiments on c-axis oriented sapphire rods have been carried out to verify its steady state creep behavior. These sapphire rods were fabricated by LFHZ (Laser Heated Float Zone) method in NASA John Glenn Research Center as for those eutectic Al_2O_3/c-ZrO_2 discussed in Chapter 2.1. The creep experiments that were carried out yield a limited number of steady state creep rate data of single crystal sapphire at 1400°C and 1500°C, shown in Fig 7-2 with solid symbols. The steady state creep rates of 1500°C

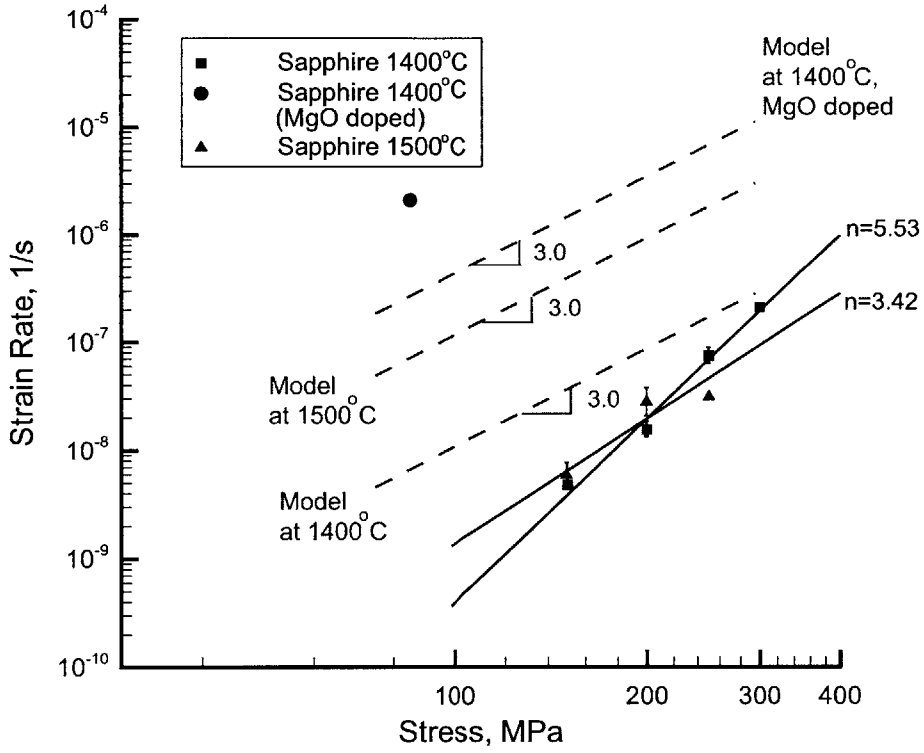

Figure 7-2: Plots of steady state creep rates of single crystal sapphire as a function of stress for temperatures of 1400, and 1500°C. Broken lines represent predictions of creep model for Al_2O_3 at 1400°C and 1500°C.

indicates a stress exponent, n=3.42, which is very close to 3 as in Eq. 7.13 and the data from Firestone and Heuer [1976] in a temperature range of 1600°C to 1800°C. The steady state creep rate data at 1400°C indicate a rather high stress exponent, n = 5.53, higher than expected. Moreover, comparing the 1400°C results with those at 1500°C, the creep rate at 250 MPa at 1400°C is higher than the creep rate at same stress at 1500°C, which should not be the case in general. To determine if the anomalous behavior was a result of an axial orientation significantly different from [0001] the orientation of the principal optical axes of the sample was checked in a polarizing microscope utilizing a full Euler angle tilt and rotation stage. Moreover, surfaces were also examined carefully by Normaski contrast microscopy to detect possible slip traces of basal glide. Both checks were negative. Since no additional samples were available the 1400°C experiment could not be repeated leaving the findings in doubt.

Diffusion process has a critical role in the steady state creep process of sapphire, since the steady state creep strain of sapphire at high temperature is derived from the climbing of a pyramidal dislocation network. If the diffusion process can be slowed down to some extents, as discussed in Section 7.1, with proper doing, such as, Ti^{4+}, the steady state creep strain rate will be reduced correspondingly.

A MgO-doped sapphire rod was tested at 1400°C to verify the influence of oxygen diffusion altered by dopants to the creep resistance since a higher oxygen diffusion coefficient from the doping of MgO is expected. Because of un-controllable reasons, the exact content of MgO dopant is unknown in this sample. An X-Ray Fluorescence Spectrometry (XRF) (by SPECTRO X-LAB 2000, Kleve, Germany) examination was applied to the surface of several pieces of rods cut down from the sample rod. The result reveals a concentration of Mg ion around 2,000 ppm with a major impurity of Si ion having a concentration around 1,000 ppm. It has to be emphasized that these numbers can only be taken as a rough reference about the concentration of dopants, not as an indication of the exact concentration, since the XRF only examines a small area of the non-flat rod surfaces in this specific test. The

steady state creep rate from this MgO-doped sapphire is shown in Fig 7-2. The MgO-doped sapphire has a much higher steady state creep comparing to those of un-doped sapphire at 1400°C, even with the relatively high concentration of tetravalent Si ion present. Since only one creep rate of doped sapphire is available, it only serves as a qualitative indication on its effect on the creep resistance of doped sapphire.

All of the steady state creep rate data of eutectic Al_2O_3/c-ZrO_2 and single crystal Al_2O_3 along with the predictions from dislocation models are shown in Fig 7-3. The creep rates of un-doped sapphire and those of eutectic Al_2O_3 are relatively close, although in most cases, undoped sapphire having a slightly higher steady state creep rate. For both specimens, the creep model overpredicts the creep rates. Clearly, the weak element in the analysis is the unavailability of accurate information on the diffusion constant.

7.3 Creep Resistance of Eutectic Al_2O_3/c-$ZrO_2(Y_2O_3)$ with Doping

As discussed in section 7.2, the doping of aliovalent species such as Mg^{2+} and Ti^{4+} have measurable influences (13-50 times) on oxygen diffusion kinetics of sapphire, and then change the steady state creep rate of sapphire. The creep deformation of eutectic Al_2O_3/c-ZrO_2 is from the climbing of Al_2O_3 pyramidal dislocations which convolute through the c-ZrO_2 domains. Obviously, there is a possibility that if doped appropriately with tetravalent species, such as Ti^{4+}, eutectic Al_2O_3/c-ZrO_2 can have a higher creep resistance by slowing down the oxygen diffusion kinetics in Al_2O_3 phase. In this research, unfortunately, no such experiment has been able to be carried out because of some limitations.

There are very few studies on doping in eutectic ceramics and its function of changing diffusion behavior reported so far. Clearly, it is possible that some dopants will be preferentially segregated to one eutectic phase or onto the phase interface, such as that, in Al_2O_3-ZrO_2 system, Y will be first segregated to ZrO_2 to form cubic zicornia. For the

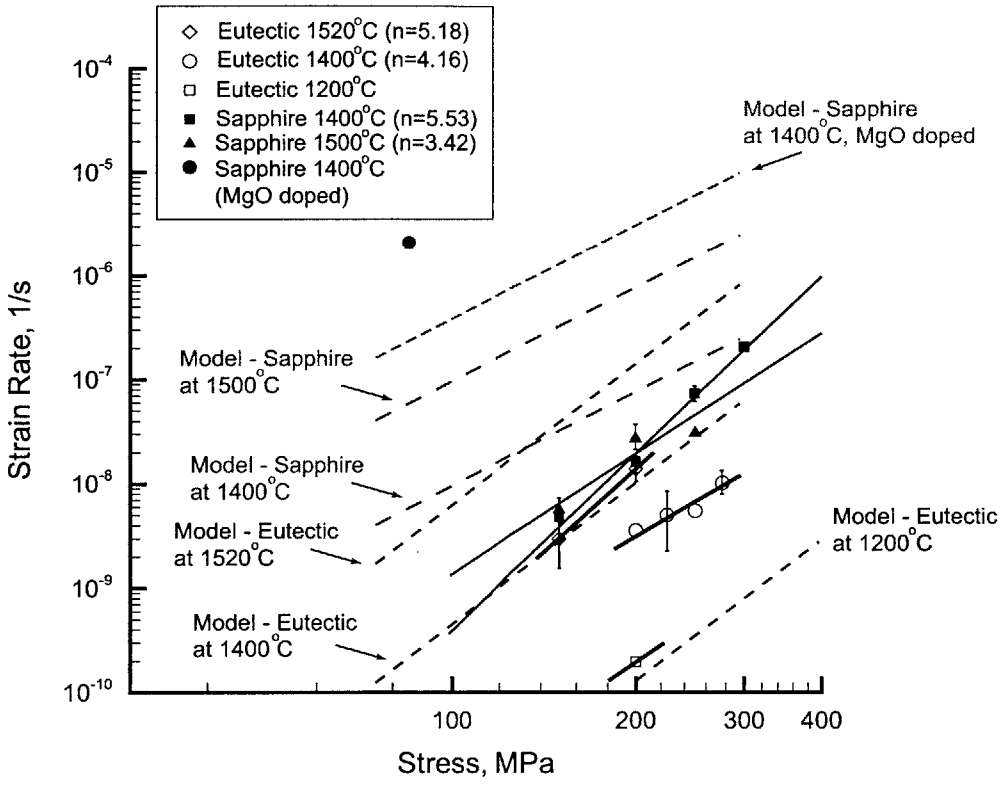

Figure 7-3: Steady state creep rate data of eutectic Al_2O_3/c-Zr_2 (Fig 6-6) and single crystal Al_2O_3 (Fig 7-2) along with the predictions from mechanistic dislocations models

segregation to interface, there are some researches has been done in doping of polycrystal Al_2O_3, such as Harmer and co-workers (Cho *et al.* [2001], Cho *et al.* [1999], Wang *et al.* [2000]). They found the some dopant ions strongly segregate to the grain boundaries, such as La-doped alumina shown in Fig 7-4, because it is energetically favorable for oversize ions to segregate to grain boundary sites. These segregated ions improve Coble creep resistance by blocking a few critical diffusive pathways. Similarly, the energetically preferable segregation could also happen in directionally solidified eutectic Al_2O_3/c-ZrO_2. The dopant ions segregate to the phase boundaries which have a high volume concentration in eutectic. These phase boundaries act as the fast diffusion channels for oxygen vacancies, in parallel to their lattice diffusion, in the dislocation creep regime which is the focus in this thesis research. The favorable doping species, Ti^{4+}, has a size of 0.68 Å, larger than 0.53 Å of Al^{3+}. Although Ti^{4+} is slightly smaller than other common dopants, such as Nd^{3+} (1.00 Å), La^{3+} (1.06 Å), Zr^{4+} (0.72 Å) and Y^{3+} (0.89 Å), it is possible to have the site-blocking effects on the oxygen vacancies diffusion at phase boundaries. Thus, in addition to the effect of lowering oxygen vacancies concentration if properly distributed in Al_2O_3, the doping with Ti^{4+} will raise the creep resistance of the eutectic Al_2O_3/c-ZrO_2 by its segregation to phase boundaries. Creep experiments of the doped eutectic and in-depth microanalysis of the phase interface structure need to be conducted in the future to verify these arguments.

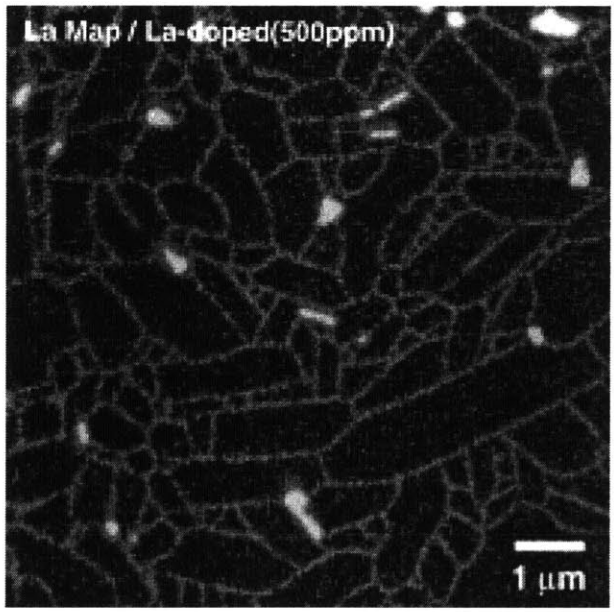

Figure 7-4: Secondary Ion Mass Spectrometry (SIMS) map showing the La distribution in the as-hot pressed 500 p.p.m. La-doped alumina. (Cho *et al.* [1999])

Chapter 8

Fracture Toughness of Directionally Solidified Eutectic Al_2O_3/c-$ZrO_2(Y_2O_3)$

Among several different eutectic ceramic oxides, the Al_2O_3/c-ZrO_2 system is one of the most interesting materials as far as the mechanical properties and the strength retention at high temperature are concerned. In the past few decades, higher tensile strength of this eutectic has been achieved by the significant improvements in the crystal-growth processing techniques (Mukhopadhyay *et al.* [1999]). Fig 8-1 (Sayir and Farmer [2000]) depicts the tensile strength of Al_2O_3/c-ZrO_2 from ambient temperature to elevated temperature plotted with c-axis sapphire data. Eutectic doesn't have the strength losses in low temperature which in part limit the usefulness of sapphire, also eutectic gradually decreases the tensile strength with temperature. Pastor *et al.* [2001] reported a similar strength behavior of eutectic Al_2O_3/c-ZrO_3.

The high strength and strength retention at elevated temperature of eutectic Al_2O_3/c-ZrO_2 are from its fine and interlocking microstructure, certainly also in part from its tolerance to defects, which is related to its fracture toughness. Ceramics are naturally brittle,

because of their mixed ionic-covalent bonding, which provides for only a limited number of independent slip systems that are necessary to achieve the homogeneous plastic deformation commonly observed for many metallic materials. The fracture under relatively low stress levels is a critical problem in the practical design of engineering structures using ceramics. From these aspects, the fracture toughness of eutectic Al_2O_3/c-ZrO_2 is an important property to understand its usefulness in structural application.

There are various experimental techniques to evaluate fracture toughness, including a wide variety of specimen geometries, crack dimensions from large macrocracks or macronotches to indentation induced microflaws. A review by Sakai and Bradt [1993] has presented a summary of most common techniques during the time. The macronotches approaches include the single edge notched bend (SENB) and compact tension (CT) specimens for metal systems at ambient temperature, and double cantilever beam (DCB), double torsion (DT), and chevron notch (CHV) specimen geometries for both metals and brittle ceramics. Among microflaws techniques, there are the controlled surface flaw (CSF) method, the indentation microfracture technique (IM) and determination of indentation strength in bending (ISB).

The indentation microfracture (IM) method has been frequently used in the past decade because of its relative ease of application, no extensive machining or preparation required for the test specimen, and that only a small specimen size is required (Evans and Charles [1976], Anstis *et al.* [1981], Niihara *et al.* [1982], Sakai and Bradt [1993], Quinn and Lloyd [2000], Pastor *et al.* [2001], Lude [2001], Lim and Muchtar [2002]). It can be readily carried out by 'sharp' hardness indenters. The two major indenter geometries have been the Knoop and Vickers configurations, because they are readily available commercially. At a critical indentation load a crack initiated below the contact point due to the generation of a tensile stress component. The subsurface crack which is formed is commonly referred to as a 'median crack', as seen in Fig 8-2a. When the load is removed and the indenter is retracted, the subsurface median cracks become unstable and expand towards the indented surface to result in the 'radial crack', as shown in Fig 8-2a and 8-2b. In some cases, shallow radial

surface cracks known as Palmqvist cracks, depicted in Fig 8-2c, can form at relatively low indentation loads before the subsurface median crack. These different crack geometries were detected by layer-by-layer removal and decoration techniques in some ceramics (Lude [2001]). Niihara *et al.* [1982], based on the dimensional analysis from Evans and Charles [1976], proposed a formal criterion on crack-length/indent-diagonal ratio to distinguish median/radial (or half-penny) cracks and Palmqvist cracks. This methodology of evaluating fracture toughness is relatively well accepted in many brittle materials studies. According to Niihara *et al.* [1982], for the Palmqvist crack ($0.25 \leq l/a \leq 2.5$) the data can be described by

$$(K_{\mathrm{Ic}}\phi/Ha^{1/2})(H/E\phi)^{2/5} = 0.035(l/a)^{-1/2} \tag{8.1}$$

For the median/radial cracks ($2.5 \leq c/a$), the corresponding expression is

$$(K_{\mathrm{Ic}}\phi/Ha^{1/2})(H/E\phi)^{2/5} = 0.129(l/a)^{-3/2} \tag{8.2}$$

where K_{Ic} is the critical stress intensity factor for Mode I fracture, ϕ is the constraint factor (≈ 3), H is the hardness, E is the Young's modulus, a is the half-diagonal of the Vickers indent, c is the radius of the surface crack and l is the length of the Palmqvist crack, as shown in Fig 8-2.

Pastor *et al.* [2001] measured fracture toughness of directionally solidified eutectic Al_2O_3/c-ZrO_2 as $7.8 \pm 0.3\mathrm{MPa}\sqrt{\mathrm{m}}$ together with its Young's modulus and flexure strength. They used two different techniques to measure the fracture toughness. A rod of 40mm in length was used where a straight notch of depth of $a = 0.34D$ was cut with a very thin diamond wire. The notch root radius was approximately 180μm. The rod was then mounted to a tensile loading machine by epoxy. The notched rod was tested in tension until fracture under stroke control at a cross-head speed of 2mm/min. The fracture toughness was computed from the fracture load and the rod section using the appropriate stress intensity factor. The fracture toughness was also determined by the indentation fracture method, which measures the length of the cracks nucleated at the corners of the impressions. The fracture toughness

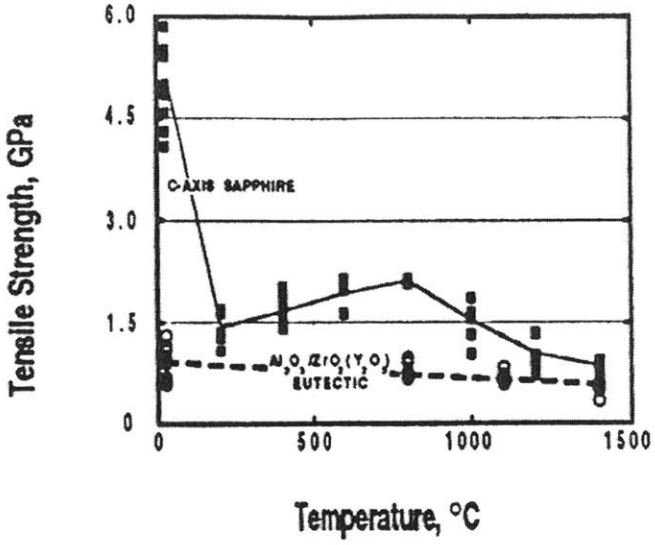

Figure 8-1: Tensile strength of eutectic Al_2O_3/c-ZrO_2 from ambient temperature to elevated temperature plotted with c-axis sapphire data. (Sayir and Farmer [2000])

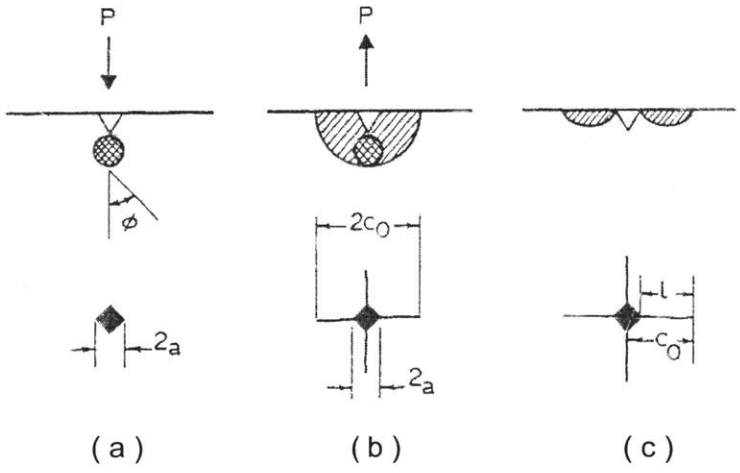

Figure 8-2: Schematic of indentation induced crack system (Sakai and Bradt [1993]) (a) median (b) median/radial (c) Palmqvist.

was computed using the equations 8.1 and 8.2, by Niihara *et al.* [1982].

In this thesis, the fracture toughness of directionally solidified eutectic ceramic Al_2O_3/c-ZrO_2 was not the major focus. However, several evaluating approaches were carried out and are presented here for the purpose of providing additional understanding on this eutectic's fracture toughness (Yi and Argon [2004]). They are evaluations using the size of internal pore or surface flaw, crack deflection, and a novel approach of open-crack shape analysis (COD).

8.1 Evaluation by Internal Pore and Surface Flaw

During this research, some eutectic specimens were prematurely fractured while the load was increased at the test temperature. A close examination of fracture surfaces (Fig 8-3) revealed large internal pores and surface flaws existing in the specimen. They are attributed to the incomplete wetting of component charges during sintering, and trapped gases with unstable crystal growth fronts during LFHZ processing. Examples of internal pores and surface flaws are shown in Fig 8-4.

Assuming the internal pores or surface flaws observed were the largest internal defects in the specimen, they can be seen as pre-existing cracks that trigger fracture under loads. In the case of Fig 8-4a, the evaluation can be simplified as an internal circular flaw in a large plate; while in the case of Fig 8-4b, the evaluation can be simplified as a semielliptical surface crack in a flat plate. The stress intensity factor for an internal circular flaw in a large plate (Suresh [1998]) is

$$K_{\mathrm{I}} = \frac{2}{\pi}\sigma\sqrt{\pi a} \tag{8.3}$$

where K_{I} is Mode I stress intensity factor, a is the radius of a circular (penny-shaped) crack. The stress intensity solution for a semi-elliptical surface crack at the mid-point (Suresh [1998]) is

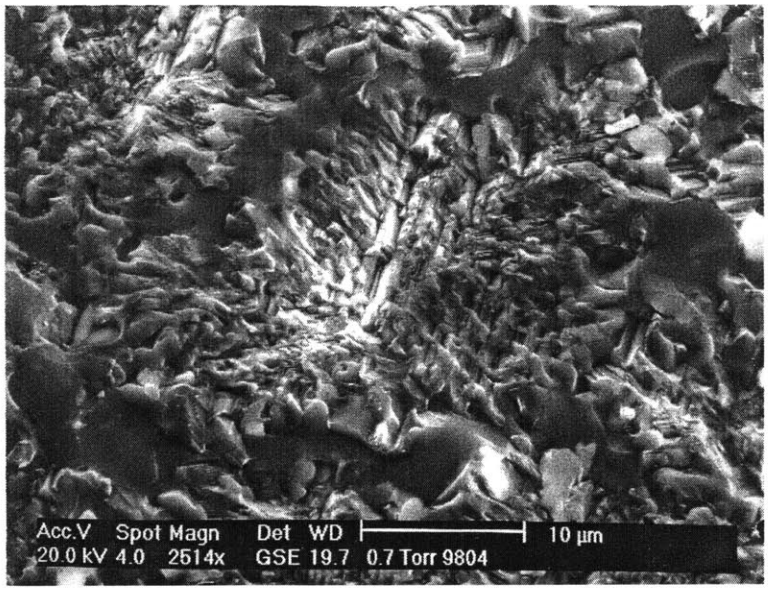

(a)

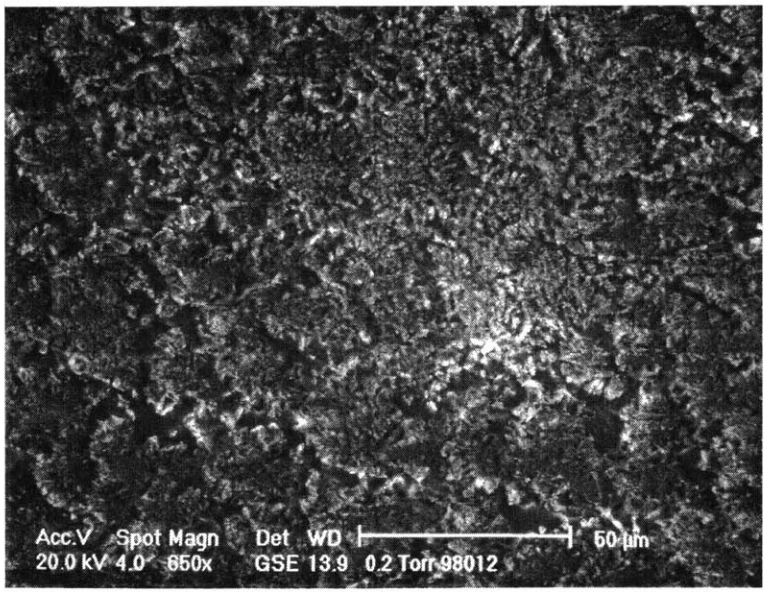

(b)

Figure 8-3: Fracture surfaces of prematurely fractured specimen while applying loading at test temperature at 1400°C.

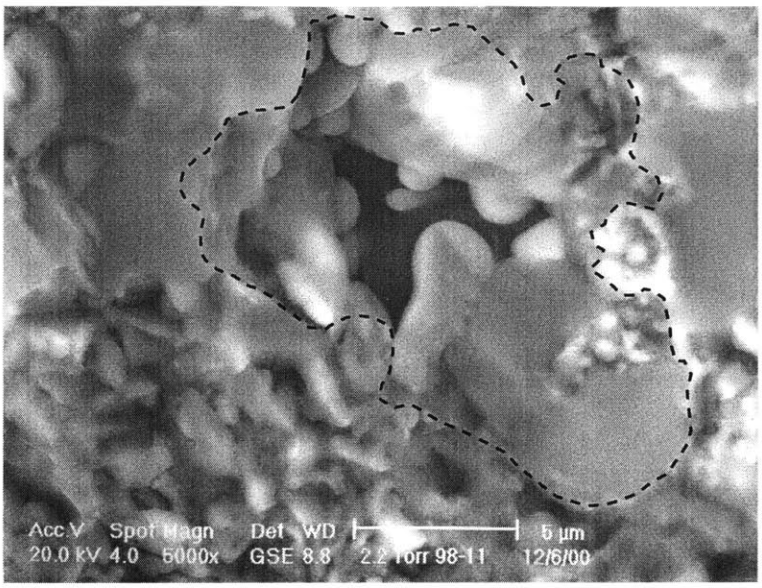

(a)

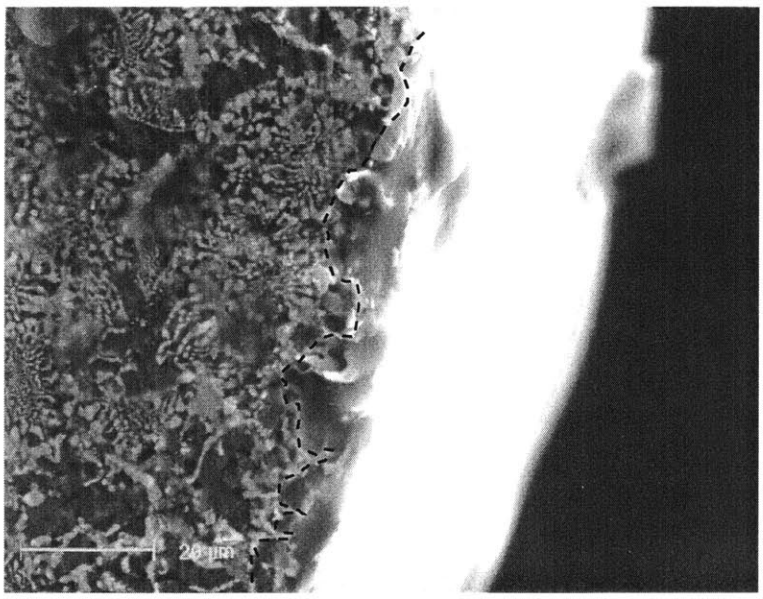

(b)

Figure 8-4: Internal pore (a) and surface flaw (b) observed at prematurely fractured specimen

$$K_{\mathrm{I}} = \frac{1.12\sigma\sqrt{\pi a}}{\sqrt{Q}} \tag{8.4}$$

where Q is the flaw shape parameter, $Q = \psi^2$ and

$$\psi \approx \frac{3\pi}{8} + \frac{\pi}{8}(\frac{a^2}{c^2}) \tag{8.5}$$

Table 8.1 gives an overview of estimated fracture toughness from the internal pore and surface flaw of Fig 8-4. The estimations based on the assumed internal pore and surface flaw are reasonably close. However, they are relatively small comparing to the measurements given by Pastor *et al.* [2001] and the value in the following sections. Clearly, the idealizations and approximations made in this approach make it to be not too exact.

8.2 Evaluation by Crack Deflection

The creep-fractured surfaces of directionally solidified eutectic Al_2O_3/c-ZrO_2 has very different characteristics comparing with those of single crystal Al_2O_3, as shown in Fig 8-5 (Firestone and Heuer [1976]), which is a tensile-creep-fractured surface of 0° single crystal Al_2O_3 tested at 1800°C. The commonly observed features of single crystal Al_2O_3 are mirror, mist, hackle and crack-branching patterns. For the directionally solidified eutectic Al_2O_3/c-ZrO_2, the fracture surfaces shown in Fig 8-3 do not have an obvious mirror area and large wave length of hackle area. This must be due to the eutectic's heterogeneous microstructure from its composite nature. The ZrO_2 domain forces the crack to be deflected by both cracking along the phase interface and cracking into the ZrO_2 fibers. The crack deflection governs the work of fracture locally as the representative crack front segment advances along a series of individual interfaces in a mixed mode, deviating substantially from the average plane of crack. The crack front has to twist and tilt to deflect around the c-ZrO_2 fibers. Features found to be important in determining the toughness increase include the volume fraction of seconde phase, the particle morphology and aspect ratio, and

the distribution of interparticle spacing. Faber and Evans [1983a], Faber and Evans [1983b] and Argon [2000] offered a detail account on the crack deflection processes.

Atomic Force Microscopy (AFM) was utilized here to characterize the profile of the eutectic fracture surface. Fig 8-7 is an AFM image of part of the fracture surface shown in Fig 8-3b. From multiple measurements from this image and AFM images on other fracture areas, the root main square surface roughness, h, can be found to be around 389~702nm, and mean surface wave length, λ, to be 320 nm.

Argon [2000] stated a simplified model to assess the crack deflection toughening mechanism based on the derivation of Faber and Evans [1983a]. In Faber and Evans' model, the principal toughing effect is the increased actual fracture surface area relative to its projection on the geometrical crack plane. Argon [2000] assumed that debonding at matrix-particle interfaces, ignoring additional complications arising from local rubbing and the independent cracking underneath the main crack, can account for much of the toughening effect. This will result in a work of fracture of

$$J_c = 2\Gamma_0 c\beta \tag{8.6}$$

where Γ_0 is the specific interface debonding energy, c is the volume fraction of heterogeneities, and β is the aspect ratio of these heterogeneities.

In the eutectic Al_2O_3/c-ZrO_2, the specific interface debonding energy is taken here as the basal plane surface energy of sapphire, 1.3 J/m^2 (Levi and Kaplan [2003]), volume fraction of c-ZrO_2 is 0.33 and aspect ratio, β, is taken as

$$\beta = \frac{L}{d} \approx \frac{4h}{\lambda} \tag{8.7}$$

where h and λ are the values measured above from AFM profiling, while L and d are the height and width of heterogeneity. Substituting the values of Γ_0, c, h and λ into Eq. 8.6 and 8.7, the enhanced work of fracture can be estimated as 4.17~7.52 J/m^2.

Table 8.1: Evaluation of Fracture Toughness by the Size of Internal Pore or Surface Flaw

	Internal Pore (Fig 8-4 a)	Surface Flaw (Fig 8-4 b)
Testing Temperature	1400°C	1400°C
Stress	200MPa	200MPa
Defect Size	$a \approx c \approx 1 \times 10^{-5}$m	$a = 1.5 \times 10^{-5}$m;$c = 4.5 \times 10^{-5}$m
Fracture Toughness	0.71MPa$\sqrt{\text{m}}$	1.26MPa$\sqrt{\text{m}}$

[a]Specimens were prematurely fracture during creep test.

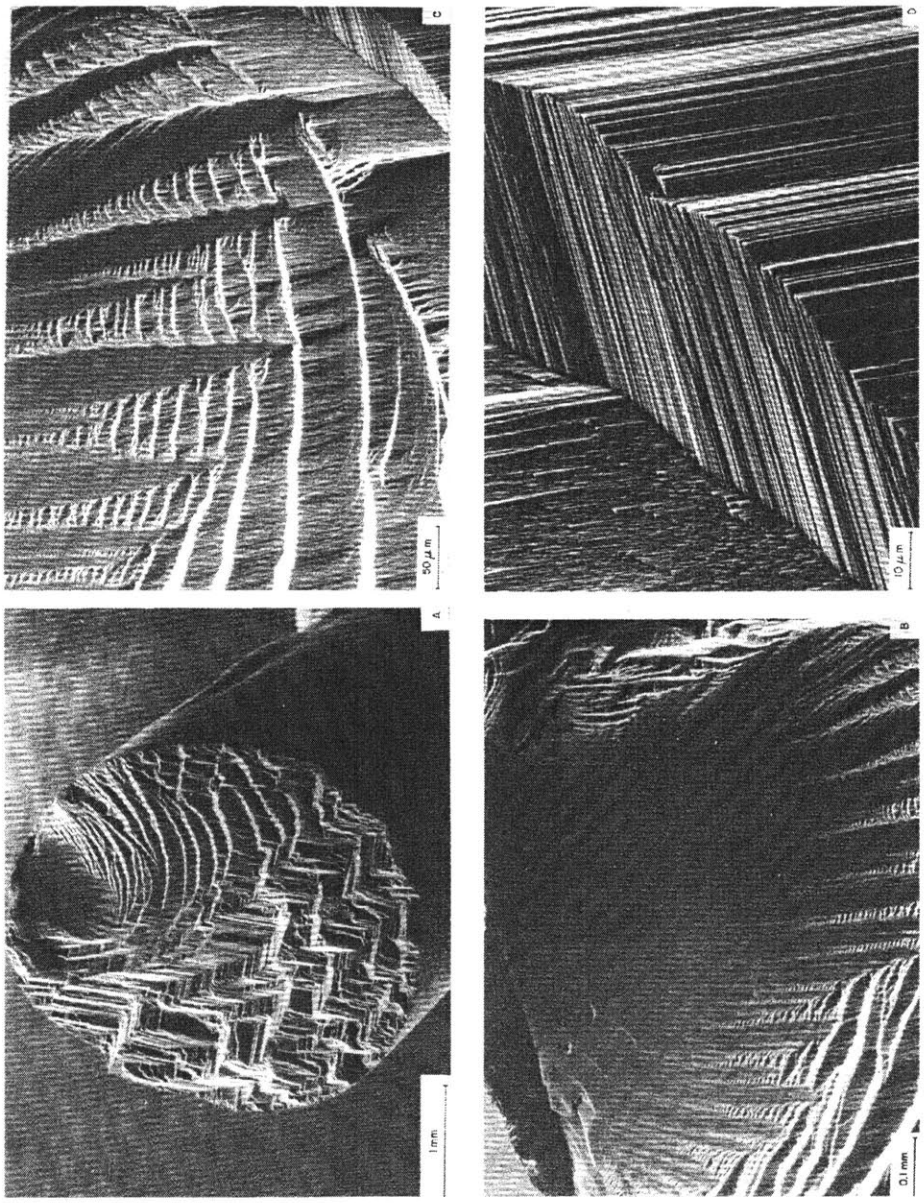

Figure 8-5: Scanning electron micrographs of 0° sapphire fracture surface during creep tests at 1800°C. A) Low magnification, entire cross section shown; B) mirror; C) fine hackle; and D) coarse hackle. (Firestone and Heuer [1976])

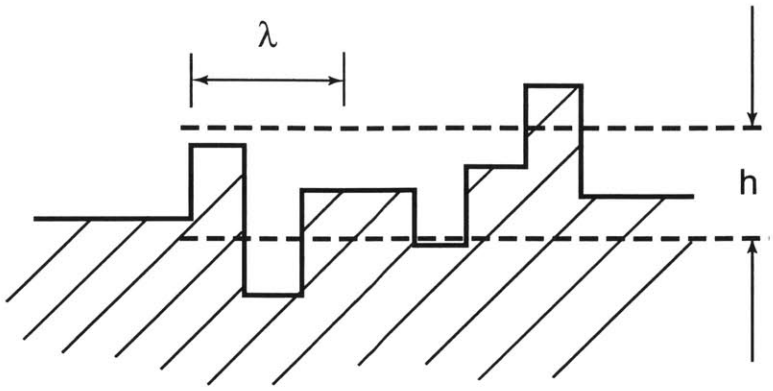

Figure 8-6: Schematic of the fracture surface showing deflection having two characteristic parameters, λ, mean surface wave length and, h, root mean square surface roughness.

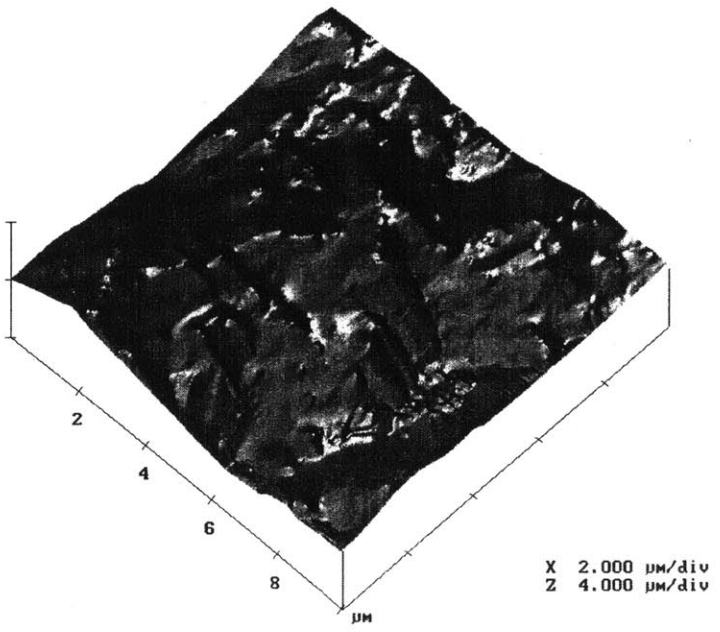

Figure 8-7: Atomic Force Microscopy image of part of fracture surface shown in Fig 8-3b

Under linear elastic Mode I loading condition, the fracture energy can be taken as (Anderson [1995])

$$J = \frac{K_I^2(1-\nu^2)}{E} \tag{8.8}$$

where E is Young's modulus and ν is Poisson's ratio. Taking E as 190GPa at 1400°C for Al_2O_3 (Wolfenden [1997]) and ν as 0.22 (Dowling [1998]), the K_{Ic} of the eutectic can be determined as 0.87~1.2MPa$\sqrt{m}$. This estimation is in the same range as the estimates determined from the size of internal pores and surface flaws given in section 8.1.

8.3 Evaluation by Open-Crack Shape Analysis

The last approach of evaluating fracture toughness of directionally solidified eutectic Al_2O_3/c-ZrO_2 is an indentation fracture testing procedure using a Vickers indenter with a novel approach of open-crack shape analysis (or COD) presented by Haubensak and Argon [1997]. This method has been shown to possess good accuracy with some chosen model materials with well-defined toughness values and has higher resolution than some previously discussed methods involving measurement of indentation crack lengths emanating from Vickers indentations, such as, Eq. 8.1 and 8.2 by Niihara *et al.* [1982].

On polished eutectic surface, a Vickers indentation was made with 400g load, as shown in Fig 8-8. There are cracks emanated from each corner of the indent. Along the cracks, crack deflection while the crack is crossing ZrO_2 domains, and crack bridging in the crack wake are clearly seen in Fig 8-9. These all are effective toughening mechanisms in this eutectic.

Instead of following the formula of Niihara *et al.* [1982], which evaluates the fracture toughness by the ratio of crack-length/indent-diagonal ratio, an open-crack shape analysis developed by Haubensak and Argon [1997] was carried out here. Haubensak and Argon [1997] assumed that the cracks keep their open-crack shapes after the indentation load is

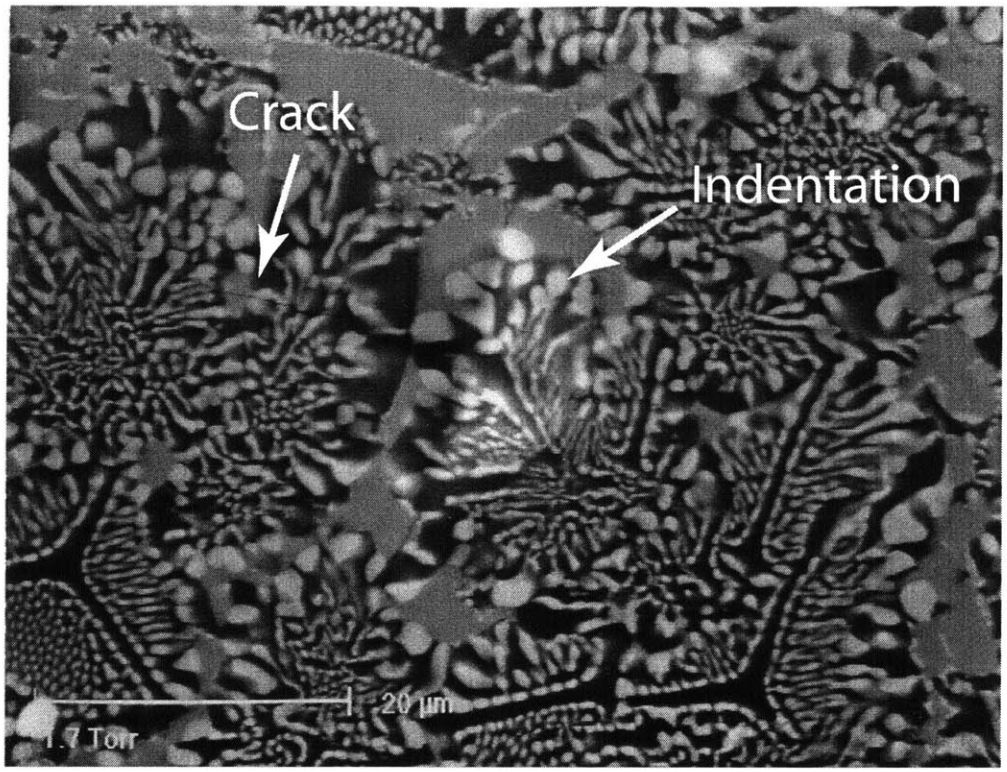

Figure 8-8: An indentation made by Vickers indenter with 400g load on the transversal section of eutectic Al_2O_3/c-ZrO_2.

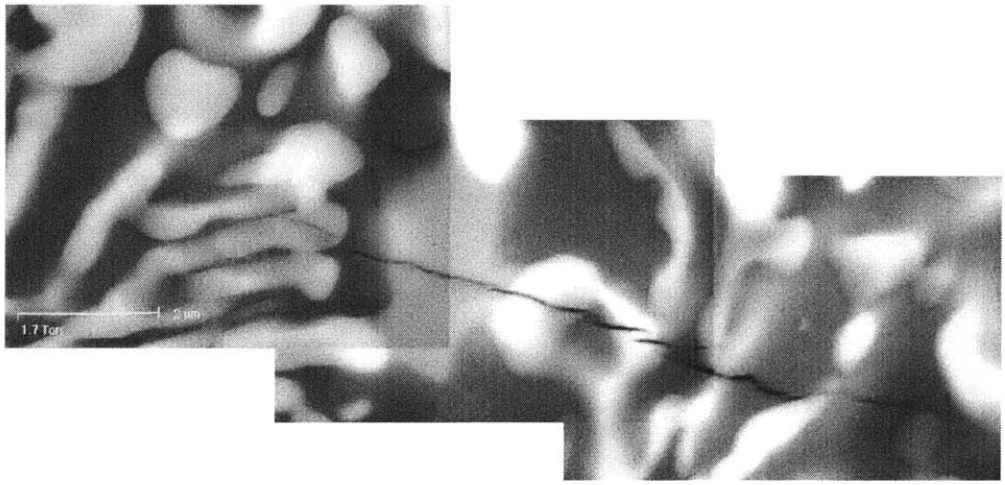

Figure 8-9: Scanning Electron Microscopy micrograph of one crack emanated from the corner of Vickers indent.

removed because of the crack bridgings and the residual ligaments along the crack. They stated that in a Mode I crack-tip field for a crack under impending motion, $K_{\mathrm{I}} = K_{\mathrm{Ic}}$ can be determined from

$$K_{\mathrm{Ic}} = \frac{(\mathrm{COD})E}{F(r/a)a^{1/2}} \tag{8.9}$$

where $F(r/a)$ is a non-dimensional characteristic crack-shape factor dependent on the geometry and the model of loading, a is the crack length, r is the distance from the crack tip as seen in Fig 8-10 and E is the Young's modulus. The function $F(r/a)$ was determined by finite element methods (FEM) for a crack with a given geometry and mode of loading under a unit K_{I}, $a^{1/2}$ and E. An example is given in Fig 8-10 cited from Haubensak and Argon [1997] in the case which will be used to evaluate fracture toughness of eutectic here.

The open-crack shape or crack opening displacement (COD) measurements are done primarily by scanning electron microscopy (SEM) technique. High resolution SEM micrographs were taken to ensure the accurate measurement of COD. Fig 8-9 is one example of these micrographs.

The multiple measurements over the crack length identifying the open-crack shape are substituted in Eq. 8.9 with the function $F(r/a)$ shown in Fig 8-10. The calculated K_{Ic} result for two cracks are presented in Fig 8-11a and 8-11b. Table 8.2 presents a comparison among three methods used to determine fracture toughness by indentation cracks, i.e., Haubensak and Argon [1997], Niihara *et al.* [1982] and Anstis *et al.* [1981]. The Anstis formula has the form of

$$K_{\mathrm{Ic}} = 0.016(E/H)^{1/2}P/c^{3/2} \tag{8.10}$$

where P is the load on the indenter, H is the Vickers hardness, c is the crack length measured from the crack tip to the center of the indentation. The estimation from Anstis *et al.* [1981] is relatively large. The cracks emanated from the indent corner here can be identified as Palmqvist type cracks. Anstis model assumes the crack is of median type, and it doesn't give good result for Palmqvist type cracks. The estimations from Niihara *et al.* [1982] and

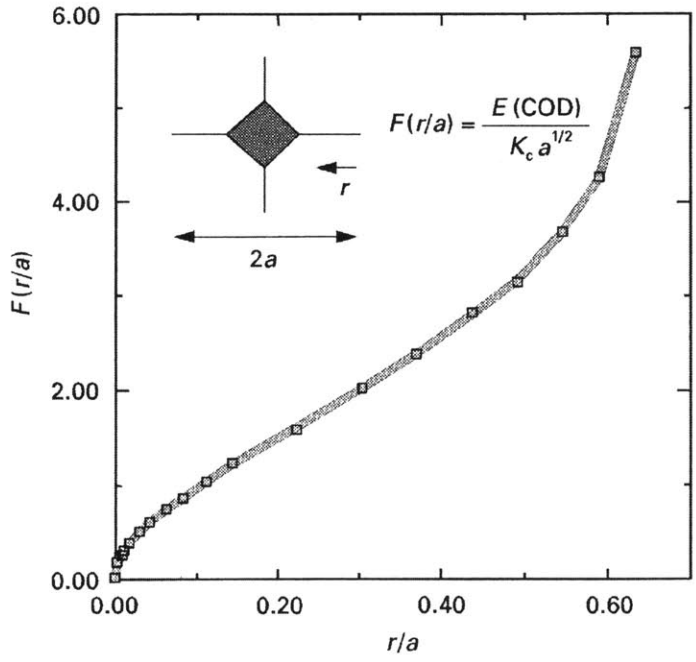

Figure 8-10: The non-dimensional open-crack displacement function for an isotropic elastic two-dimensional material from Haubensak and Argon [1997]. In this calculation, the application of the point load dipole occurs at $r/a = 0.65$.

Haubensak and Argon [1997] are reasonably close. However, in general, the Haubensak and Argon [1997] should give higher resolution of fracture toughness and the analysis is independent of the crack type, which offers additional advantage over previous methods.

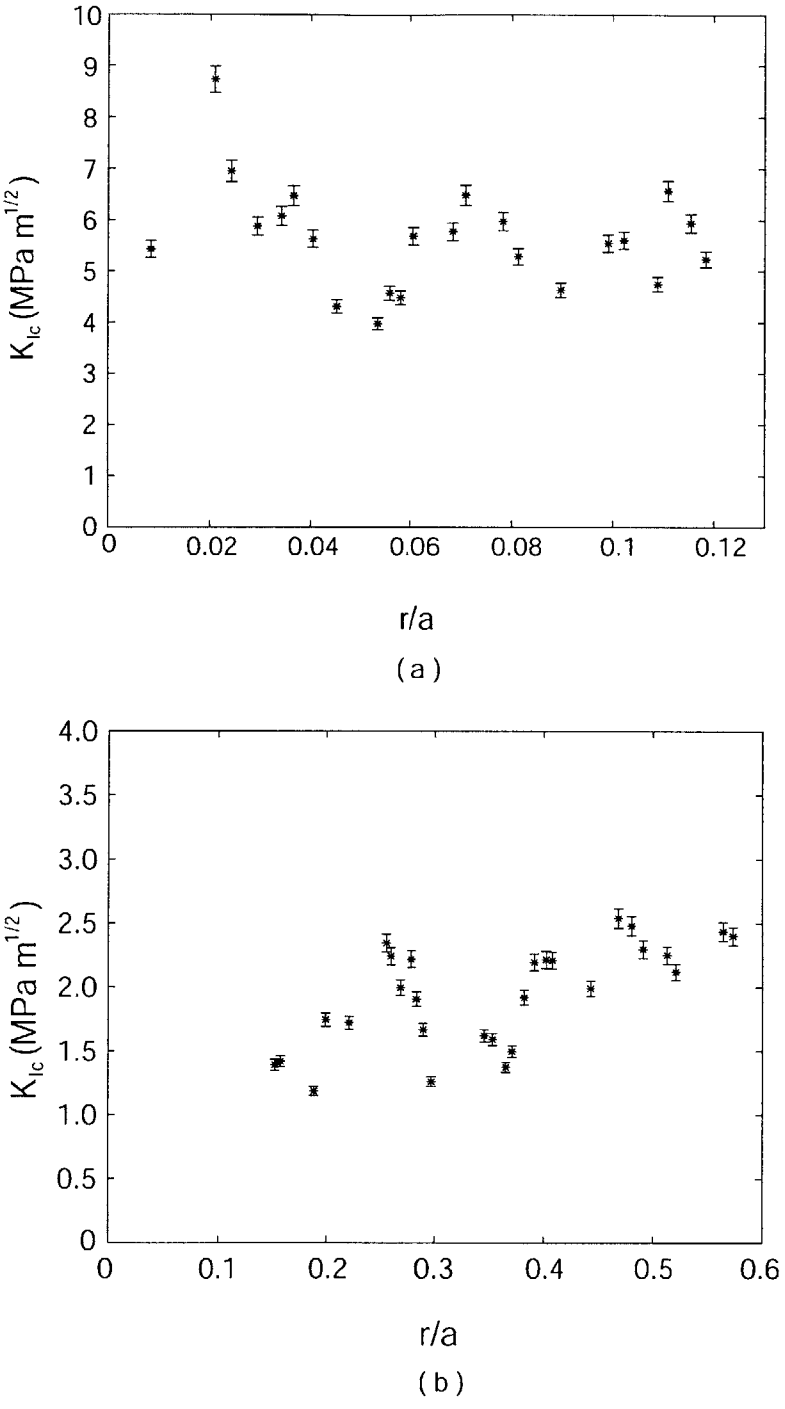

Figure 8-11: Fracture toughness estimations based on the open-crack shape method (a) crack0215 (b) crack0202.

Table 8.2: Fracture Toughness Estimation by Vickers Indentation

Crack #	crack0215	crack0220
Load	400 g	400 g
Indent Diagonal (μm)	17.14	17.14
Crack length (μm)	8.031	15.25
Vickers Hardness (HV, kg/mm^2)	2523	2523
K_{Ic} (by Anstis *et al.* [1981] method) (MPa$\sqrt{\mathrm{m}}$)	11.36	6.61
K_{Ic} (by Niihara *et al.* [1982] method) (MPa$\sqrt{\mathrm{m}}$)	4.08	2.96
K_{Ic} (by Haubensak and Argon [1997] method) (MPa$\sqrt{\mathrm{m}}$)	5.3	2.0

Chapter 9

Conclusions

In this thesis research, tensile creep experiments in the temperature range of 1200~1520°C have been conducted and a mechanistic dislocation model has been developed to understand the creep mechanism of directionally solidified eutectic Al_2O_3/c-ZrO_2. An potential application of this mechanism to improve the creep resistance of this eutectic has also been explored. Meanwhile, the fracture toughness of this eutectic has also been assessed. Here list the major conclusions in this thesis.

1. In the eutectic of Al_2O_3/c-ZrO_2(Y_2O_3) the majority phase Al_2O_3 is topologically continuous, has a nearly perfect texture of [0001] parallel to the growth direction and encapsulates everywhere the minority c-ZrO_2 phase which itself has a growth texture of $< 110 >$.

2. The interfaces separating the phases are well structured and have semi-coherent portions. However, they are incoherent over most of the area.

3. A large fraction of the c-ZrO_2 phase has a sub-micron oriented fibrillar morphology which often, but not always, aggregates into colonies. The remaining fraction, usually surrounding the colonies of oriented fibrils or platelets is of a coarser, micron size, and are often serrated.

4. The eutectic morphology is stable against coarsening over periods of the order of 168 hours at 1400°C. The presence of a stress 300MPa has also produced no measurable coarsening over the same length of time at 1400°C.

5. Upon first application of stress, transient creep is observed which is attributed to stress relaxation in the coarser fraction of the c-ZrO_2. The sub-micron fraction is considered to be too small to undergo deformation by crystal plasticity and is expected to be dormant.

6. In steady state creep, stress changes do not produce additional transients within the resolution of stress measurements.

7. The stress dependence of steady state creep rate is of power-law form with an exponent in the range between 4.5 to 5.0 with the given eutectic morphology. The activation energy of the creep rate is 299 kJ/mole in the 1400-1500°C range and is attributed to oxygen ion diffusion through the Al_2O_3 and along the interfaces.

8. Most of dislocations observed, by TEM, of crept specimen have the pyramidal type of dislocation with the Burgers vector of $1/3 < \bar{1}101 >$. There are also certain amount of basal dislocation presented in the crept specimen. This is similar with the observations in [0001] oriented sapphire by Firestone and Heuer [1976].

9. Low angle boundaries are found between the columnar colonies in the crept specimen. These boundaries are of asymmetrical tilt boundary and formed by two sets of pyramidal dislocations. These pyramidal dislocations could come from dislocation reaction between basal dislocations and nonbasal dislocation, and could also result from aggregation of climbing pyramidal edge dislocations. The low angle boundaries could be the mechanism to accommodate the rotation of the colony during creep deformation.

10. Because of the [0001] texture of the Al_2O_3 phase which must control the overall creep rate for topological reasons, the proposed steady state model is based on the climb of

the $(1/3) < 1\bar{1}01 >$ dislocations in Al_2O_3 since the latter are sessile in glide.

11. In the creep model which is a generalization of the steady state diffusional creep model of Nabarro [1967], the larger than 3 stress exponents are attributed to the necessity of repeated bowing and straightening of the climbing dislocations in Al_2O_3 as they circumvent the sub-micron c-ZrO_2 domains.

12. The predictions of the mechanistic dislocation creep model, which has no adjustable constants, agree quite well with experimental observations.

13. TEM observations were largely in support of the creep model and confirmed the presence of pyramidal dislocations in the crept samples.

14. A few creep experiments on [0001] oriented sapphire crystals demonstrated a stress exponent of 3.5 at 1500°C and showed creep rates very closely similar to those recorded in the eutectics.

15. A test of MgO doped sapphire crystal showed very significantly enhanced creep rates in comparison with undoped sapphire in support of expectations.

16. Three different methods have been carried out to evaluate the fracture toughness of this eutectic. While these values are not attractively large, they are higher than values measured for monolithic components of alumina and cubic zirconia. The evaluation by open crack shape analysis gave a high resolution and reasonable good result.

Appendix A

Nucleation of a pyramidal edge dislocation in Al_2O_3 from other dislocations

1. Nucleation from an edge dislocation in the c-ZrO_2 at the interface of Al_2O_3 and c-ZrO_2

   Consider a circular bulge shaped embryo of a pyramidal edge dislocation in Al_2O_3 of length λ emanating under a local shear stress τ from an edge dislocation in c-ZrO_2, pressed to the interface from the c-ZrO_2 side as depicted in Fig. A-1. The c-ZrO_2 dislocation might be followed by a small pile up in the zirconia which, if present, can amplify τ by the number n of dislocations in the pile up.

   In the circular bulge region of the embryo the bowed out segment of the pyramidal dislocation of Burgers vector $\mathbf{b_p}$, leaves at the interface an interface dislocation of Burgers vector $\mathbf{b_i}$ which is related to the Burgers vectors $\mathbf{b_p}$ and $\mathbf{b_z}$ of the zirconia dislocation by the relation

$$b_z^2 = b_i^2 + b_p^2 - 2b_i b_p \cos\phi \tag{A.1}$$

where ϕ is the angle between the vector $\mathbf{b_i}$ and $\mathbf{b_p}$. Then the free energy change ΔG of the bowed out configuration under the applied stress τ is, relative to the initial straight dislocation in zirconia,

$$\Delta G = 2R\theta\mathcal{E}_p + \lambda(\mathcal{E}_i + I_{ip} - \mathcal{E}_z) - \tau b_p \Delta A \tag{A.2}$$

where

$$\mathcal{E}_p \approx \frac{1}{2}\mu b_p^2 \tag{A.3}$$

$$\therefore \mathcal{E}_z = \frac{1}{2}\mu b_z^2 \tag{A.4}$$

$$\therefore \mathcal{E}_i = \frac{1}{2}\mu b_i^2 \tag{A.5}$$

are the line energies of the pyramidal dislocation in Al_2O_3, the edge dislocation in c-ZrO_2, and the interface dislocation. I_{ip} is the interaction energy between the interface dislocation and the pyramidal dislocation and is

$$I_{ip} = -\frac{\mu b_p b_i \cos\phi}{2\pi(1-\nu)} \ln\frac{\alpha\rho}{\bar{y}} \tag{A.6}$$

where α is a constant of order unity; ρ is the outer cut-off radius of the dislocation stress field that can be taken as Λ, the mean spacing between zirconia domains and $\bar{y}$ the averaged separation of the pyramidal dislocation from the interface dislocation at the nucleation stage, as shown in Fig A-1. The latter can be taken as $\Delta A/\lambda$ where $\Delta A \approx (2/3)R^2\theta^3$ for small bow out. In Eqs (A.3)-(A.6) the shear moduli of the Al_2O_3 and c-ZrO_2 are considered as qual which is close to reality.

Initially one has

$$\mathcal{E}_p + \mathcal{E}_i + I_{ip} - \mathcal{E}_z = 0 \tag{A.7}$$

over the length λ for $\bar{y} \rightarrow b$

The activation configuration is obtained from the extremal condition of

$$(\frac{\partial \Delta G}{\partial \lambda})_\tau = 0 \tag{A.8}$$

which gives

$$\lambda^* = 2\sqrt{\mathcal{E}_p \mathcal{E}_z}/\tau b_p \tag{A.9}$$

and from Eqs (A.2) and (A.7)

$$\Delta G^* = (\mu b_z^3)(\mu/3\tau) \tag{A.10}$$

2. As a variant of the above case one might consider the nucleation of a pyramidal edge dislocation from a basal edge dislocation in Al_2O_3 in a climb mode under high vacancy mobility. This gives an expression similar to Eq. (A.10) where however $\mathbf{b_z}$ is replaced with a basal dislocation Burgers vector $\mathbf{b_b}$ and the shear stress is replaced with the climb stress $\sigma_\perp$.

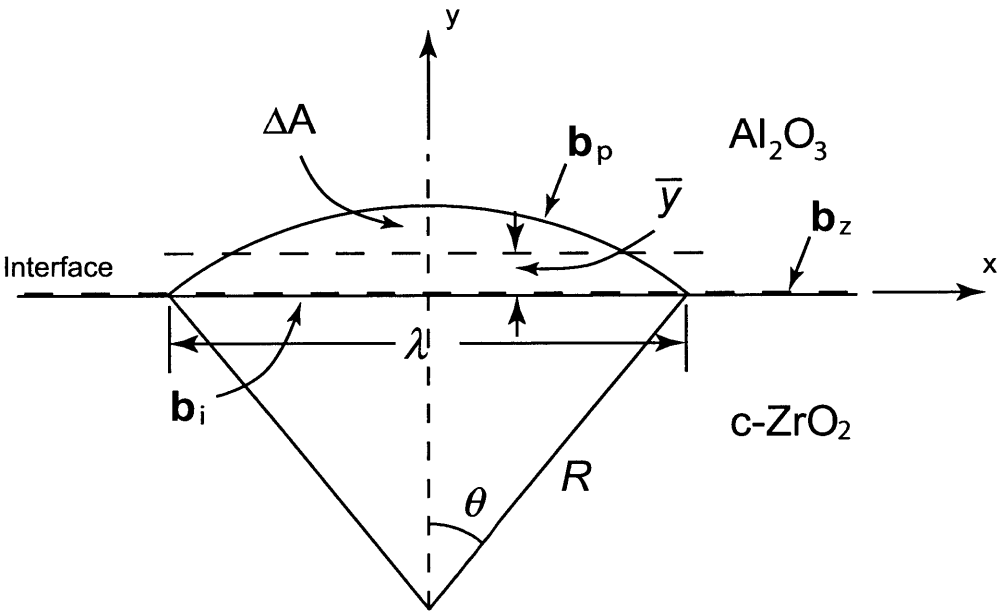

Figure A-1: Nucleation of a pyramidal edge dislocation from a c-ZrO_2 dislocation.

Appendix B

The kinematics of creep strain rate by climb

As presented in Section 6.2, if a single set of parallel edge dislocations of density ρ were to climb with a velocity v_c, a strain rate $\dot{\epsilon_0} = b\rho v_c$ would result in the direction perpendicular to the plane of the climbing dislocations.

Referring now to Fig. 6-1, consider the coordinate axis set 1, 2 ,3, of a pyramidal glide system in a round bar of Al_2O_3 where the 1 axis is parallel to the Burgers vector of the pyramidal edge dislocations and the 1,3 pyramidal plane makes an angle ϕ with respect to the bar axis z. Under a tensile stress σ_1 then, a density ρ of dislocations climbing in the 2 direction (positive edge dislocations in the negative 2 direction and negative edge dislocations in the positive 2 direction) a creep rate $\dot{\epsilon_0}$ in the 1 direction of would result. However, such climb requires extension of extra half planes which requires material fluxes to arrive to the dislocation from all directions and dispersal of vacancies into all directions, resulting in contractile strain rates $\dot{\epsilon}_{1c}, \dot{\epsilon}_{2c}, \dot{\epsilon}_{3c}$. For preservation of volume, it would be necessary that

$$\dot{\epsilon_0} + \dot{\epsilon}_{1c} + \dot{\epsilon}_{2c} + \dot{\epsilon}_{3c} = 0 \tag{B.1}$$

and since by symmetry

$$\dot{\epsilon}_{1c} = \dot{\epsilon}_{2c} = \dot{\epsilon}_{3c} \tag{B.2}$$

the net strain rates become

$$\dot{\epsilon}_1 = \frac{2}{3}\dot{\epsilon}_0 \tag{B.3}$$

and

$$\dot{\epsilon}_2 = \dot{\epsilon}_3 = -\frac{1}{3}\dot{\epsilon}_0 \tag{B.4}$$

Resolving these strain rates into the axes r, and z of the creep bar gives

$$\dot{\epsilon}_z = (\frac{2}{3} - cos^2\phi)\dot{\epsilon}_0 \tag{B.5}$$

therefore

$$\dot{\epsilon}_r = -(\frac{1}{3} - \frac{1}{2}cos^2\phi)\dot{\epsilon}_0 \tag{B.6}$$

Since there are three sets of pyramidal dislocations, all with equal capacity to contribute to axial strain rate, we take the total axial strain rate to be

$$\dot{\epsilon}_z = (2 - 3cos^2\phi)\dot{\epsilon}_0 \tag{B.7}$$

and

$$\dot{\epsilon}_r = -(1 - \frac{3}{2}cos^2\phi)\dot{\epsilon}_0 \tag{B.8}$$

where the dislocation velocity in $\dot{\epsilon}_0$ is still related to tensile stresses parallel to the Burgers vectors of the pyramidal dislocations. Resolving these tensile stresses to the axial tensile stress σ_z, then gives the climb-causing tensile stresses

$$\sigma_1 = q\sigma_z(1 - cos^2\phi) \tag{B.9}$$

where the factor q , was determined from a FEM boundary value problem, refers to the volume average of the climb producing stress in the Al_2O_3 component between the c-ZrO_2 components. This development is discussed in Section 6.3.

Appendix C

Geometry of RVE for FEM analysis of stress distribution in eutectic Al_2O_3/c-$ZrO_2(Y_2O_3)$

c-ZrO_2 phase is mostly of two forms of morphology in topologically continuous nearly-single-crystal Al_2O_3, as shown in Fig 2-3a. The nearly-uniform-distributed sub-micron fibrillar form, which acts as dispersoids during the creep deformation interacting with climbing pyramidal dislocations in Al_2O_3, is of interests in the mechanistic model. Those coarse c-ZrO_2 components are most likely fully relaxed during transient creep stage.

Inside the columnar colony, those c-ZrO_2 fibers are in elliptical shape within Al_2O_3 matrix. It is assumed that c-ZrO_2 fibers has a uniform distribution in the matrix, i.e., the distances between centers of the fibers are all equal on the transverse section. Fig C-1 presents a schematic drawing of this relationship.

Ellipse has the parameters of a, b and eccentricity

$$e = \frac{\sqrt{a^2 - b^2}}{a}, \tag{C.1}$$

with an area of $S = \pi ab$ and peripherial length

$$P = 4aE(e) = 4a\int_0^{\pi/2}\sqrt{1-e^2\sin^2 t\,dt} \tag{C.2}$$

where $\int_0^{\pi/2}\sqrt{1-e^2\sin^2 t\,dt}$ is the complete elliptical integral of the second kind. At point P shown in figure C-1, there have

$$\frac{x^2}{a^2}+\frac{y^2}{b^2} = 1 \tag{C.3}$$

$$\tan\phi = \frac{x}{y} = \frac{A}{2B}. \tag{C.4}$$

Eqn C.4 gives

$$x = \frac{A}{2B}y. \tag{C.5}$$

Substituting it to Eq. C.3, the equations become

$$x = \frac{\frac{A}{2B}}{\frac{1}{a}\sqrt{\frac{A^2}{4B^2}+\frac{b^2}{a^2}}} \tag{C.6}$$

$$y = \frac{a}{\sqrt{\frac{A^2}{4B^2}+\frac{a^2}{b^2}}}. \tag{C.7}$$

So that,

$$\begin{aligned}\Lambda &= \sqrt{\frac{A^2}{4}+B^2}-2L \\ &= \frac{1}{2}\sqrt{A^2+4B^2}-\frac{2a\sqrt{\frac{A^2}{4B^2}+1}}{\sqrt{\frac{A^2}{4B^2}+\frac{a^2}{b^2}}}.\end{aligned} \tag{C.8}$$

Also, the distance between c-ZrO_2 fiber is

$$\Lambda = A - 2a. \tag{C.9}$$

Volume fraction of c-ZrO_2 can be represented as

$$c = \frac{\pi ab}{AB}, \tag{C.10}$$

by which a relation can be written as

$$\frac{A^2}{B^2} = \frac{A^4 C^2}{\pi^2 a^4 (1 - e^2)} \tag{C.11}$$

where e is the eccentricity of Eq. C.1. Substituting Eqs C.9, C.11 into C.8 and defining $x = 2a/A$, a final equation can be written as

$$\frac{1}{2}\sqrt{1 + \frac{\pi^2(1-e^2)}{c^2}\frac{x^4}{4}} - \frac{x\sqrt{\frac{c^2}{\pi^2(1-e^2)}\frac{4}{x^4} + 1}}{\sqrt{\frac{c^2}{\pi^2(1-e^2)}\frac{4}{x^4} + \frac{1}{1-e^2}}} = 1 - x. \tag{C.12}$$

The equation can be solved numerically to get $x = 2a/A$. Then,

$$a = \frac{xA}{2} \tag{C.13}$$

$$b = a\sqrt{1 - e^2} \tag{C.14}$$

$$B = \frac{\pi ab}{Ac} = \frac{\pi a^2\sqrt{1 - e^2}}{Ac} \tag{C.15}$$

The table C.1 lists some results from Eq. C.12 as an example while volume fraction $c = 0.3$.

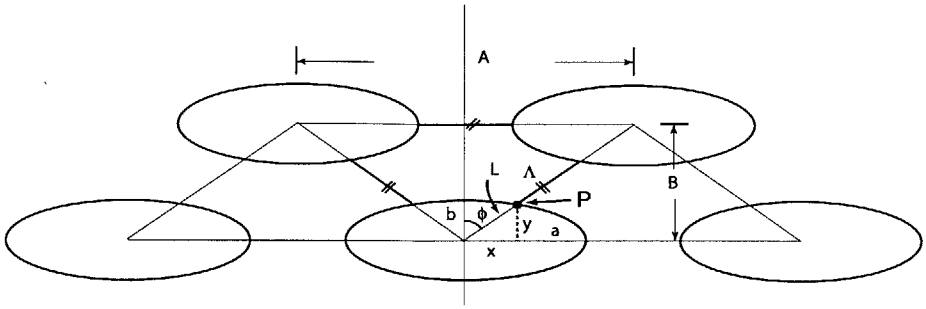

Figure C-1: Schematic drawing of c-ZrO_2 elliptical fibers in Al_2O_3 phase.

Table C.1: Parameters of RVE

Volume Fraction	c=0.3		
	a/b=0.3	a/b=0.4	a/b=0.5
a	0.3432 A	0.3525 A	0.3581 A
b	0.1144 A	0.0882 A	0.0716 A
B	0.4112 A	0.3256 A	0.2685 A

Appendix D

FEM analysis of stress distribution in eutectic Al_2O_3/c-$ZrO_2(Y_2O_3)$

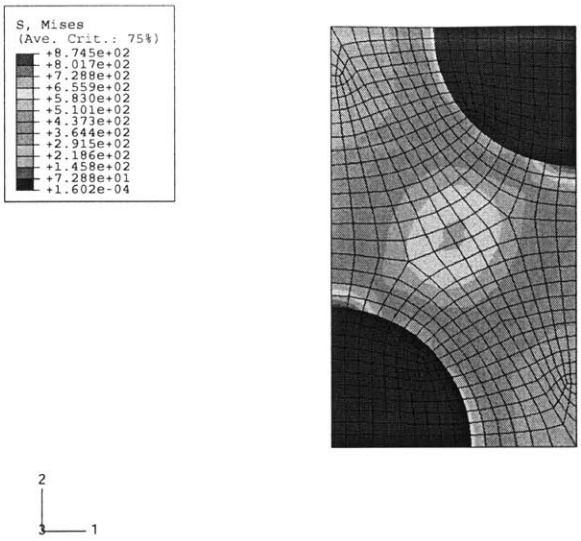

Figure D-1: Mises stress distribution under applied stress of 300 MPa at 1400°C (c-ZrO_2 fiber aspect ratio = 1).

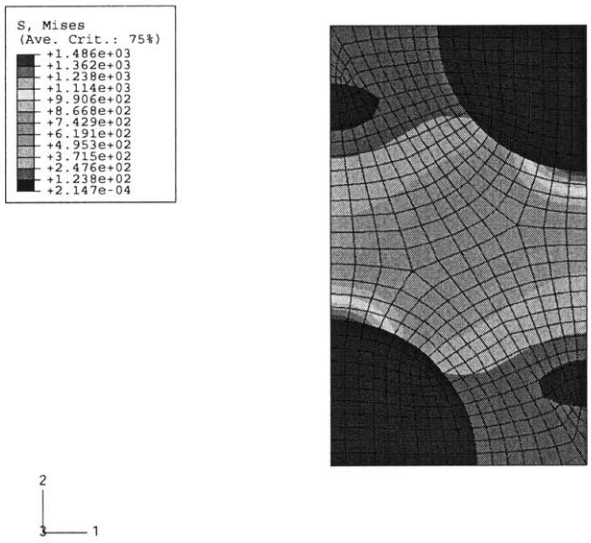

Figure D-2: Mises stress distribution under applied stress of 300 MPa at 1400°C, and thermal stress caused by the temperature drop from 1875°C to 1400°C (c-ZrO_2 fiber aspect ratio = 1).

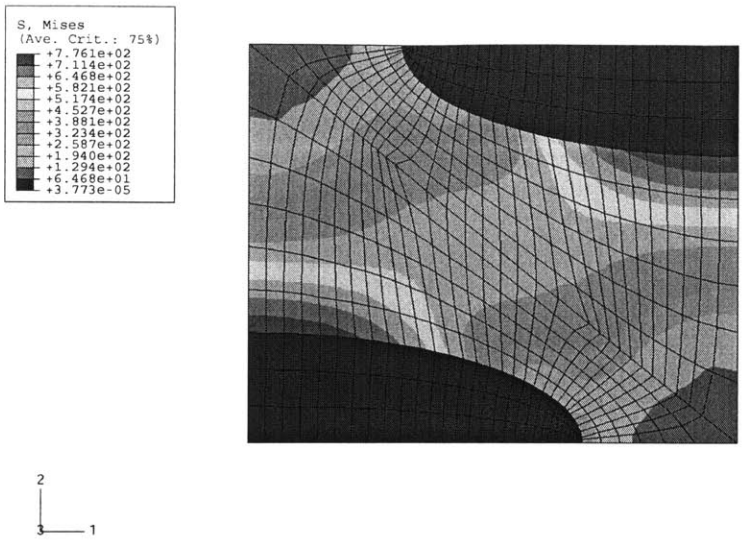

Figure D-3: Mises stress distribution under applied stress of 300 MPa at 1400°C (c-ZrO_2 fiber aspect ratio = 3).

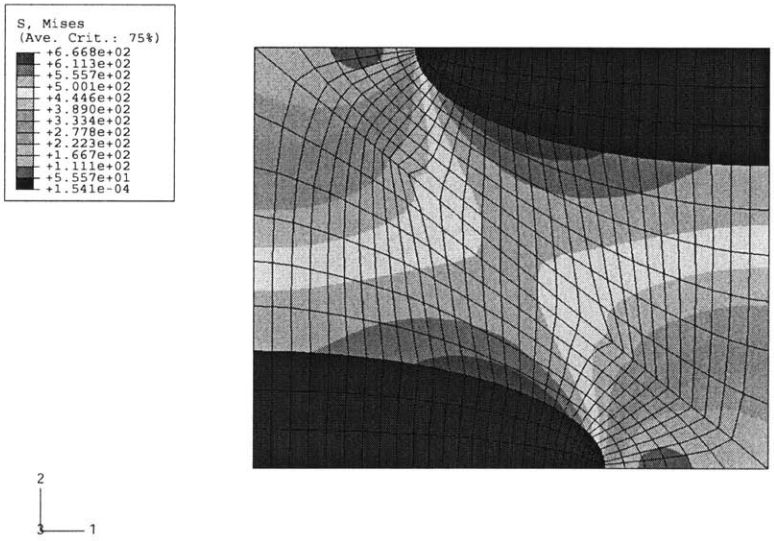

Figure D-4: Mises stress distribution under applied stress of 300 MPa at 1400°C, and thermal stress caused by the temperature drop from 1875°C to 1400°C (c-ZrO_2 fiber aspect ratio = 3).

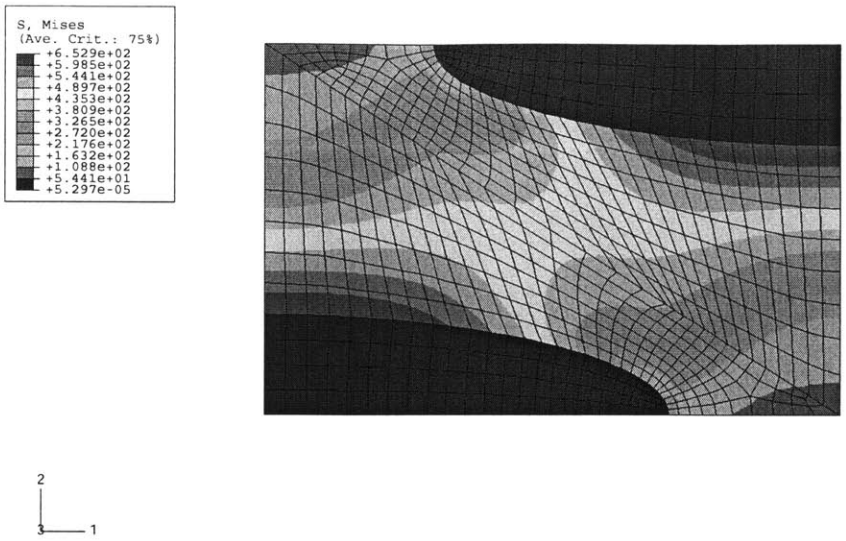

Figure D-5: Mises stress distribution under applied stress of 300 MPa at 1400°C (c-ZrO_2 fiber aspect ratio = 4).

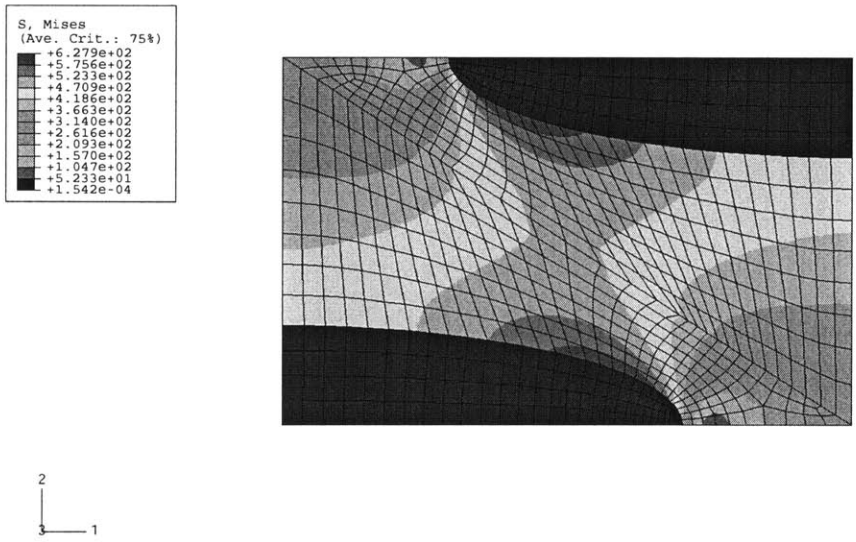

Figure D-6: Mises stress distribution under applied stress of 300 MPa at 1400°C, and thermal stress caused by the temperature drop from 1875°C to 1400°C (c-ZrO_2 fiber aspect ratio = 4).

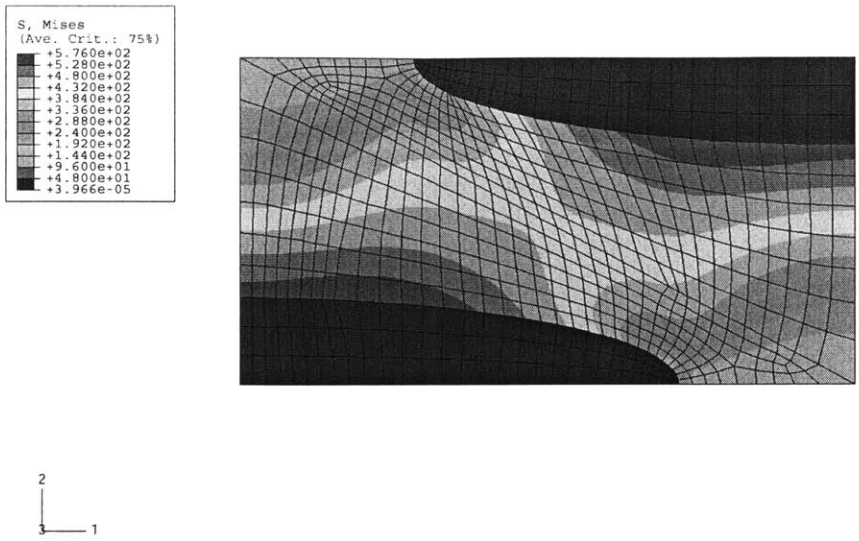

Figure D-7: Mises stress distribution under applied stress of 300 MPa at 1400°C (c-ZrO_2 fiber aspect ratio = 5).

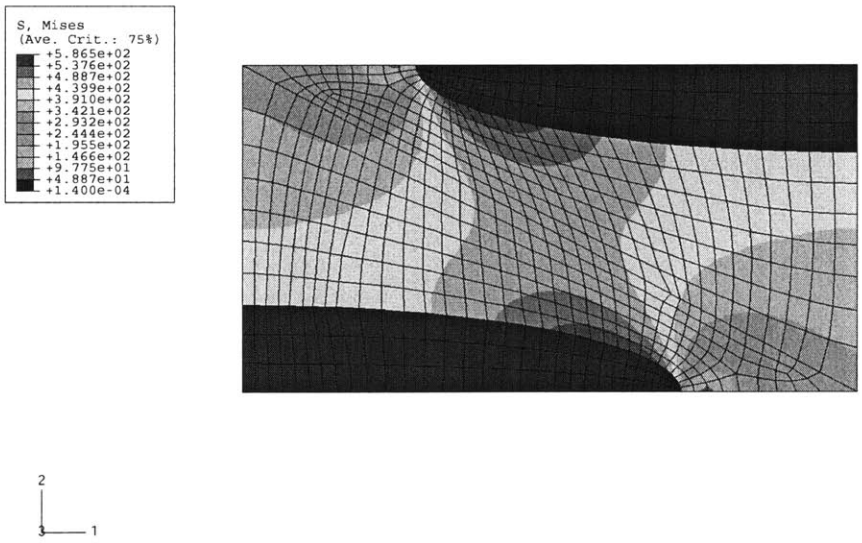

Figure D-8: Mises stress distribution under applied stress of 300 MPa at 1400°C, and thermal stress caused by the temperature drop from 1875°C to 1400°C (c-ZrO_2 fiber aspect ratio = 5).

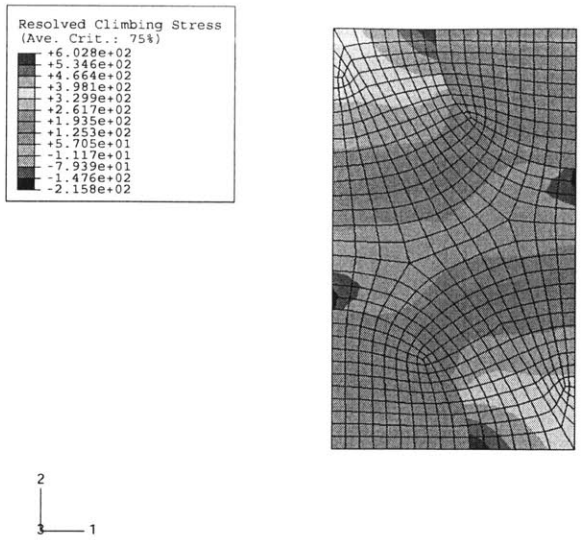

Figure D-9: Resolved climb stress distribution in pyramidal system under applied stress of 300 MPa at 1400°C (c-ZrO_2 fiber aspect ratio = 1).

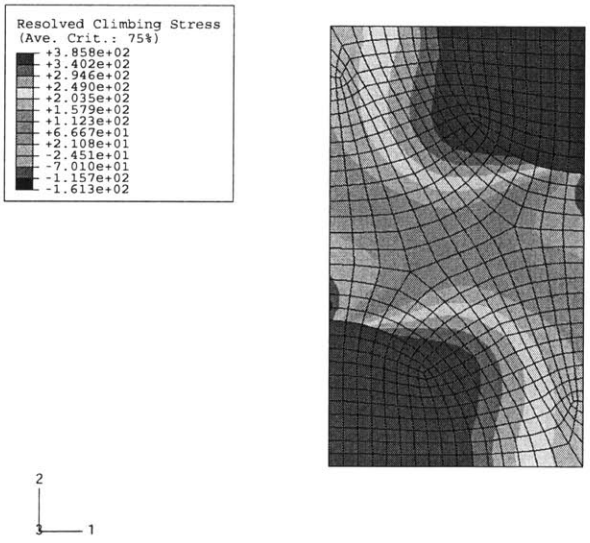

Figure D-10: Resolved climb stress distribution in pyramidal system under applied stress of 300 MPa at 1400°C, and thermal stress caused by the temperature drop from 1875°C to 1400°C (c-ZrO_2 fiber aspect ratio = 1).

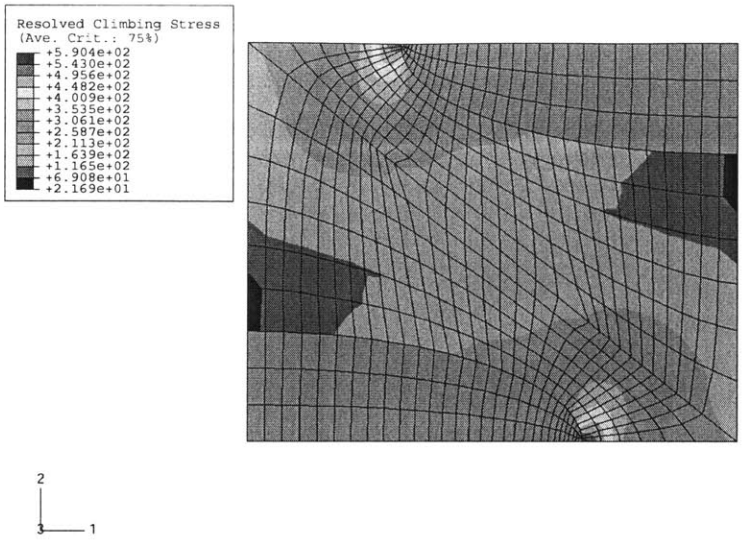

Figure D-11: Resolved climb stress distribution in pyramidal system under applied stress of 300 MPa at 1400°C (c-ZrO_2 fiber aspect ratio = 3).

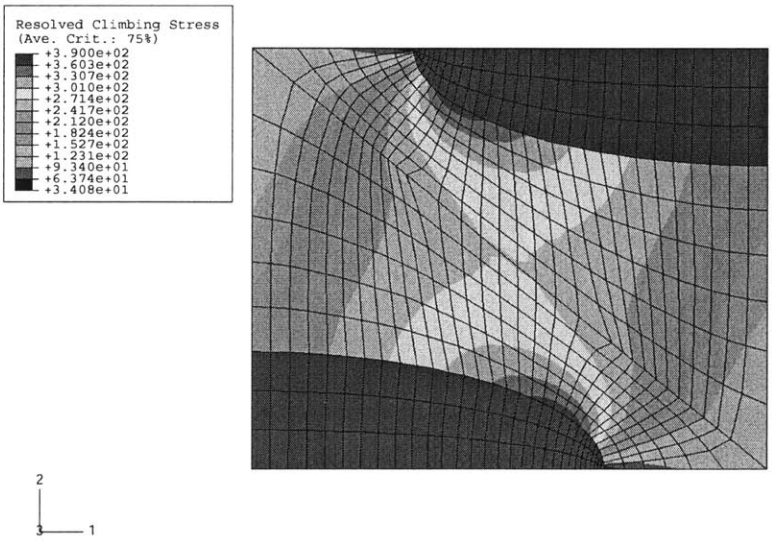

Figure D-12: Resolved climb stress distribution in pyramidal system under applied stress of 300 MPa at 1400°C, and thermal stress caused by the temperature drop from 1875°C to 1400°C (c-ZrO_2 fiber aspect ratio = 3).

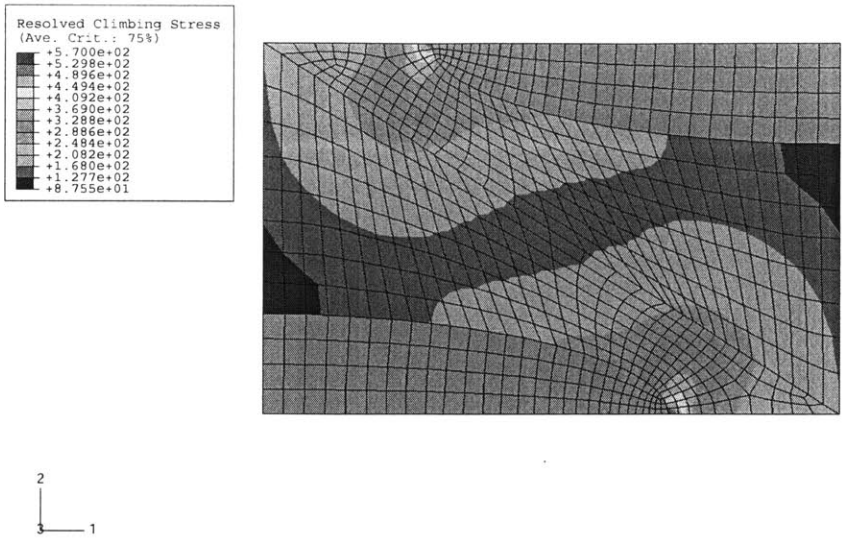

Figure D-13: Resolved climb stress distribution in pyramidal system under applied stress of 300 MPa at 1400°C (c-ZrO_2 fiber aspect ratio = 4).

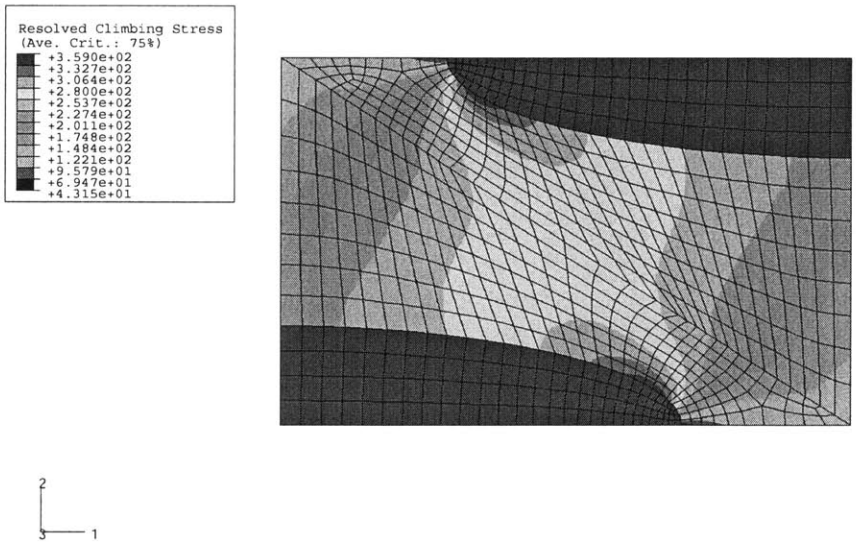

Figure D-14: Resolved climb stress distribution in pyramidal system under applied stress of 300 MPa at 1400°C, and thermal stress caused by the temperature drop from 1875°C to 1400°C (c-ZrO_2 fiber aspect ratio = 4).

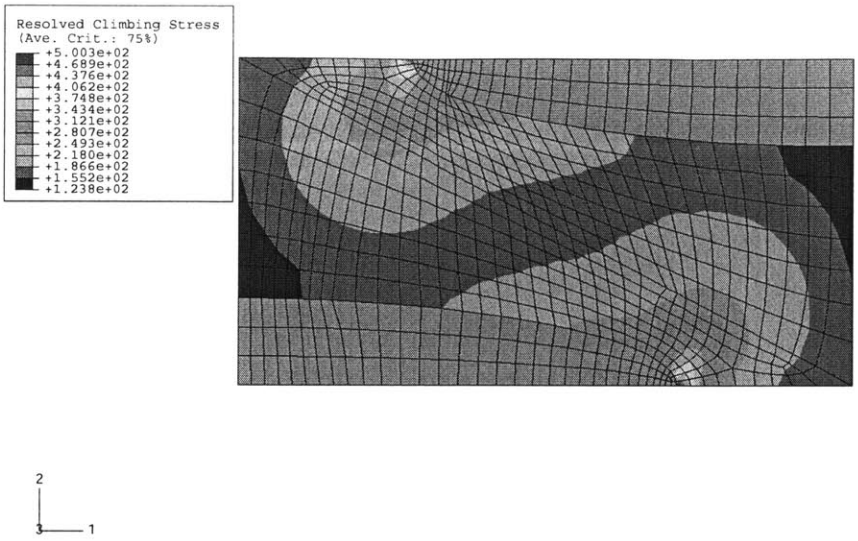

Figure D-15: Resolved climb stress distribution in pyramidal system under applied stress of 300 MPa at 1400°C (c-ZrO_2 fiber aspect ratio = 5).

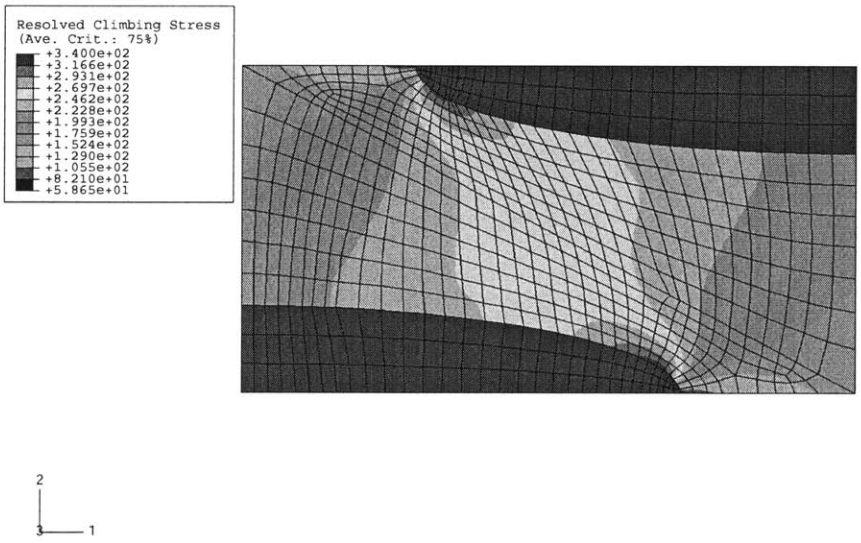

Figure D-16: Resolved climb stress distribution in pyramidal system under applied stress of 300 MPa at 1400°C, and thermal stress caused by the temperature drop from 1875°C to 1400°C (c-ZrO_2 fiber aspect ratio = 5).

Appendix E

Diffusion-controlled Climbing Dislocation Velocity

In principle, dislocation climb occurs by point-defect emission or annihilation. As a simple example of a diffusion-controlled climb process, consider the case of an edge dislocation near the center of a cylinder and the dislocation line direction being parallel to its axis (Hirth and Lothe [1968]), as shown in Fig E-1. The concentration of vacancies in local equilibrium with the surface is c^0. The triaxial component of external stress σ, σ_T, doesn't promote equilibrium climb and doesn't effect on the local equilibrium vacancy concentration. So, near the core the local equilibrium vacancy concentration is given by (Hirth and Lothe [1968])

$$c = c^0 \exp\left(\frac{\sigma' b_e \Omega}{b_e kT}\right) = c^0 \exp\left(\frac{\sigma' \Omega}{kT}\right) \tag{E.1}$$

where $\sigma' = \sigma - \sigma_T$. Thus a vacancy chemical-potential gradient exists between the dislocation and the surface because of non-zero deviatoric stress acting on the dislocation.

The diffusion flux $\mathbf{J}$ is given by the product of the vacancy of concentration c and the drift velocity, $\mathbf{V_D}$,

$$\mathbf{J} = c\mathbf{V_D} \tag{E.2}$$

The drift velocity is given by

$$\mathbf{V_D} = \frac{D_v}{kT}\mathbf{F} \tag{E.3}$$

where D_v is the vacancy diffusivity; $\mathbf{F}$ is the constant force which creates the drift, and equals to the negative gradient of the chemical potential $\bar{\mathbf{G}}$,

$$\mathbf{F} = -\boldsymbol{\nabla}\bar{G} \tag{E.4}$$

Substituting Eq. E.3 into E.4, then into Eq. E.2, the diffusion flux $\mathbf{J}$ is

$$\mathbf{J} = -\frac{D_v c}{kT}\boldsymbol{\nabla}\bar{G} = -D_v c \nabla \ln\left(\frac{c}{c^0}\right). \tag{E.5}$$

The steady-state condition is that the divergence of $\mathbf{J}$ vanishes, yielding

$$\boldsymbol{\nabla}\cdot\mathbf{J} = -\boldsymbol{\nabla}\cdot\left(Dc\boldsymbol{\nabla}\ln\frac{c}{c^0}\right) = 0 \tag{E.6}$$

Here, it assumes that c^0 and D_v are constant to make the problem simple. The assumption is good enough except in the region near the dislocation core. The equation E.6 then reduces to

$$\nabla^2 c = \frac{1}{r}\frac{\partial}{\partial r} r \frac{\partial c}{\partial r} = 0 \tag{E.7}$$

The boundary conditions are

$$\begin{aligned} c - c^0 &= 0 && \text{at } r = R \\ c - c^0 &= c' = c^0 \exp\left(\tfrac{\sigma\Omega}{kT}\right) - c^0 \approx \tfrac{\sigma'\Omega}{kT} c^0 && \text{at } r = b. \end{aligned} \tag{E.8}$$

The solution to Eq. E.7 which satisfies these boundary conditions is

$$c - c^0 = c' \frac{\ln(R/r)}{\ln(R/b)} \tag{E.9}$$

The net vacancy current per unit length away from the dislocation is

$$\begin{aligned} I &= -2\pi r D_v \frac{\partial}{\partial r}(c - c^0) \\ &= \frac{2\pi D_v c'}{\ln(R/b)} = \frac{2\pi D_v \sigma' \Omega c^0}{kTln(R/b)} \end{aligned} \tag{E.10}$$

The velocity of climb of the dislocation is

$$v_y = \frac{I\Omega}{b_e} \tag{E.11}$$

Considering the definition of the atomic self-diffusion conefficient

$$D_s = \Omega c^0 D_v \tag{E.12}$$

and substituting Eq. E.10 into E.11, one obtains

$$v_y = \frac{2\pi D_s \Omega \sigma'}{b_e kT \ln(R/b)} = \frac{2\pi D_s \sigma' b_e^2}{kT \ln(R/b)} \tag{E.13}$$

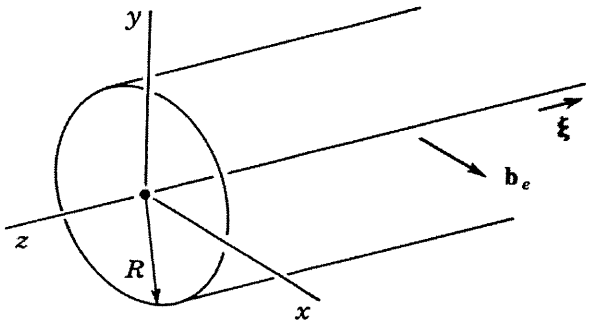

Figure E-1: An edge dislocation lying along the axis of a cylinder and the dislocation line direction being parallel to its axis (Hirth and Lothe [1968]).

Appendix F

Self-adjusting Mobile Dislocation Density

The derivation here is based on the discussion by Argon [1970]. Consider a total mobile edge dislocation density of ρ having a mean spacing of $\rho^{-1/2}$. Half of these dislocations move one way through the other half moving in the opposite direction. As the dislocations of the opposing flux components encounter each other as shown in Fig. F-1, momentary internal stresses develop and mobile dislocations are retarded.

Consider half the dislocation population at rest and the other half moving through the stationary half. The shear stress σ_{xy} which dislocation 3 feels as it passes through 1 and 2 is

$$\sigma_{xy} = \frac{\mu b_e}{8\pi(1-\nu)}\left(\frac{\sin 4\theta_1}{\frac{\lambda}{2}+y} + \frac{\sin 4\theta_2}{\frac{\lambda}{2}-y}\right) \tag{F.1}$$

where $\lambda = \sqrt{2/\rho}$ is the mean spacing between the half dislocation population who is moving in one direction, and $\tan\theta_1/(\frac{\lambda}{2}+y) = \tan\theta_2/(\frac{\lambda}{2}-y)$. Taking the approximate for the maximum resistance which dislocation 3 encounters, the expression is

$$\sigma_{xy_{max}} = \frac{\mu b_e}{8\pi(1-\nu)}\left(\frac{1}{\frac{\lambda}{2}+y} + \frac{1}{\frac{\lambda}{2}-y}\right) = D\frac{\lambda}{\left(\frac{\lambda}{2}\right)^2 - y^2} \tag{F.2}$$

where $D = \frac{\mu b_e}{8\pi(1-\nu)}$. Dislocation 3 can encounter dislocations 1 and 2 at any distance y from zero to $y_c = (\lambda/2)\sqrt{1-(4D/\lambda\sigma)}$ where the maximum internal stress σ_i given by Eq. F.1 is just equal to the applied stress σ. If the encounter occurred at $y > y_c$, where the effective stress $\sigma - \sigma_i$ is negative, the mobile dislocation would be trapped and ceases to be mobile. The velocity of a diffusion-controlled climbing dislocation, in the case of this thesis research, has the form of Eq. E.13, and can be presented as

$$v = B_1\sigma' \tag{F.3}$$

where $B_1 = \frac{2\pi D_s b_e^2}{kT\ln(R/b)}$. If the only internal stress the mobile dislocations are subjected to comes from their own kind, the strain rate is given by the expression

$$\dot{\gamma} = b_e\rho\int_0^{y_c}\bar{v}(y)\frac{dy}{y_c} = \frac{b_e\rho}{y_c(\sigma')}\int_{\sigma_i=\frac{4D}{\lambda}}^{\sigma_i=\sigma'}\bar{v}(y(\sigma_i))\frac{dy}{d\sigma_i}d\sigma_i \tag{F.4}$$

where average velocity of the ensemble is used because at any particular time there are equal numbers of mobile dislocations in each strip dy, having an average velocity $\bar{v}(y)$, and contributing to the total strain rate in proportion to their velocity. Eq. F.4 can be evaluated as (see Argon [1970] for detail)

$$\dot{\gamma} = \frac{2.18b_e^2\rho\sigma'}{b_e/B_1}\sqrt{1-\sqrt{\frac{\rho}{2}}\frac{4D}{\sigma'}} \tag{F.5}$$

This is plotted as a function of ρ for constant stress σ' in Fig. F-2. The strain rate reaches a maximum value of

$$\dot{\gamma} = 0.078\frac{b_e B_1\sigma'^3}{D^2} \tag{F.6}$$

when the mobile dislocation density is

$$\rho = \rho_1 = \frac{2\sigma'^2}{25D^2} = \frac{2\sigma'^2}{25\left(\frac{\mu b}{8\pi(1-\nu)}\right)^2} \approx \left(\frac{2\pi\sigma'}{\mu b}\right)^2 \tag{F.7}$$

which is the Eq. 6.6 considering ν=0.22 for Al_2O_3 and

$$\sigma' = \sigma_1 - \sigma_T = \frac{2}{3} q \sigma_z (1 - cos^2 \phi) \tag{F.8}$$

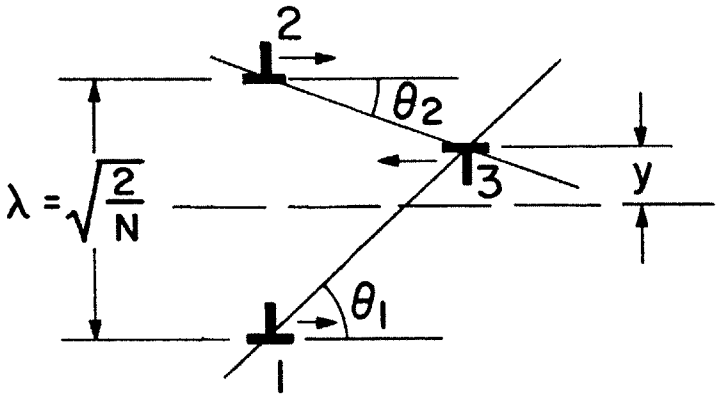

Figure F-1: Interactions of three mobile dislocations with one another (Argon [1970]).

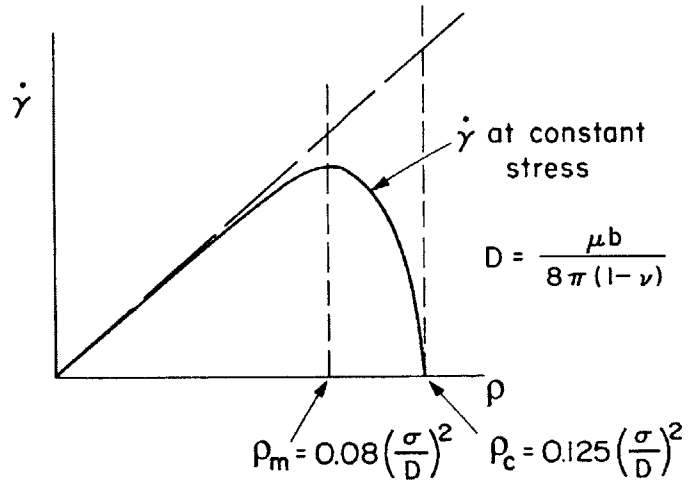

Figure F-2: Dependence of strain rate on mobile dislocation density at constant stress (Argon [1970]).

References

Anderson, T. (1995). *Fracture Mechanics: Fundamentals and Applications.* CRC Press LLC, Boca Raton, Florida, 2nd edition.

Anstis, G., Chantikul, P., Lawn, B., and Marshall, D. (1981). A critical evaluation of indentation techniques for measuring fracture toughness: I. direct crack measurements. *J. Am. Ceram. Soc.*, **64**(9), 533–38.

Argon, A. (1970). Internal stresses arising from the interaction of mobile dislocations. *Scripta Metallurgica*, **4**, 1001–1004.

Argon, A. (1982). Mechanics and mechanisms of fracture in creeping alloys. In B. Wilshire and D. Owen, editors, *Recent Advances in Creep and Fracture of Engineering Materials and Structures*, page 1. Pineridge Press, Swansee, U.K.

Argon, A. (2000). Fracture: Strength and toughness mechanisms. In A. Kelly and C. Zweben, editors, *Comprehensive Composite Materials*, volume 1 (edited by T.-W. Chou), pages 763–802. Pergamon Press, Oxford, UK.

Argon, A., Chen, I.-W., and Lau, C. (1980). Intergranular cavitation in creep: Theory and experiments. In R. Pelloux and N. Stoloff, editors, *Creep-Fatigure-Environmental Interactions*, page 46. A.I.M.E., New York.

Argon, A., Yi, J., and Sayir, A. (2001). Creep resistance of directionally solidified ceramic

eutectics of Al_2O_3/c-ZrO_2 with sub-micron columnar morphologies. *Mater. Sci. Engrg.*, **A319-321**, 838–842.

Bardeen, J. and Herring, C. (1952). Diffusion in alloys and the kirkendall effect. In W. Shockley, J. Hollomon, R. Maurer, and F. Seitz, editors, *Imperfections in Nearly Perfect Crystals*, pages 261–288. J. Wiley Sons, New York.

Bilde-Sørensen, J., Lawlor, B., Geipel, T., Pirouz, P., Heuer, A., and Lagerlöf, K. (1996). On basal slip and basal twinning in sapphire (α-Al_2O_3)-I. basal slip revisited. *Acta metall.*, **5**, 2145–2152.

Bodur, C., Chiang, J., and Argon, A. (2004). Molecular dynamics simulations of basal and pyramidal system edge dislocation cores in sapphire and their role in creep of ceramic eutectics. *J. European Ceram. Soc.* in the press.

Brochard, S., Beauchamp, P., and Grilhé, J. (2001). Simulations of dislocation nucleation from atomic size surface steps and grooves. *Materials Science and Engineering*, **A309-310**, 456–462.

Brown, L. and Stobbs, W. (1975). Modeling structural changes in deformed dispersion strengthened crsytals. In A. Argon, editor, *Constitutive Equations in Plasticity*, pages 387–429. M.I.T. Press, Cambridge, MA.

Cadoz, J., Castaing, J., Phillips, D., Heuer, A., and Mitchell, T. (1982). Work hardening and recovery in sapphire (α-Al_2O_3) undergoing prism plane deformation. *Acta metall.*, **30**, 2205–2218.

Chang, J., Bodur, C., and Argon, A. (2003). Pyramidal edge dislocation cores in sapphire. *Philosophical Magazine Letters*, **83**, 659–666.

Chiang, Y.-M., Birnie, D. P., and Kingery, W. D. (1997). *Physical Ceramics*. John Wiley & Sons, Inc, New York.

Cho, J., Wang, C., Chan, H., Rickman, J., and Harmer, M. (1999). Role of segregating dopants on the improved creep resistance of aluminum oxide. *Acta mater.*, **47**(15), 4197–4207.

Cho, J., Wang, C., Chan, H., Rickman, J., and Harmer, M. (2001). Improved tensile creep properties of yttrium- and lanthanum-doped alumina: a solid solution effect. *J. Mater. Res.*, **16**(2), 425–429.

Dickey, E. (2001). private communication.

Dickey, E. (2002). Fundamental structure-property relationships for high-temperature ceramic composites. In *AFOSR Joint Metallic and Ceramic Materials Programs Review, 2002.*

Dickey, E., Frazer, C., Watkins, T., and Hubbard, C. (1999). Residual stresses in high temperature ceramic eutectics. *J. European Ceram. Soc.*, **19**, 2503–2509.

Dowling, N. (1998). *Mechanical Behavior of Materials.* Prentice-Hall, Inc., Upper Saddle River, New Jersey.

Edelin, G. and Poirier, J. (1973). A study of dislocation climb by means of diffusional creep experiments in magnesium I. deformation mechanism. *Phil. Mag.*, **28**, 1203–1210.

Evans, A. and Charles, E. (1976). Fracture toughness determinations by indentation. *J. Am. Ceram. Soc.*, **59**(7-8), 371–372.

Faber, K. and Evans, A. (1983a). Crack deflection processes - I. Theory. *Acra metall.*, **31**(4), 565–576.

Faber, K. and Evans, A. (1983b). Crack deflection processes - II. Experiment. *Acra metall.*, **31**(4), 577–584.

Firestone, R. and Heuer, A. (1976). Creep deformation of 0° degree sapphire. *J. Amer. Ceram. Soc.*, **59**, 24–29.

Fleischer, R. (1987). High-strength, high-temperature intermetallic compounds. *J. Mater. Sci.*, **22**, 2281–2288.

Fraser, C., Dickey, E., and Sayir, A. (2001). Crystallographic texture and orientation variants in $Al_2O_3/Y_3Al_5O_{12}$ directionally solidified eutectic crystals. *J. Cryst. Growth*, **233**, 187–195.

Friedel, J. (1964). *Dislocations*, page 104. Addison-Wesley, Reading, MA.

Gooch, D. and Groves, G. (1973). Nonbasal slip in sapphire. *Phil. Mag.*, **28**, 623.

Groves, G. and Kelly, A. (1969). Change of shape due to dislocation climb. *Phil. Mag.*, **19**, 977–986.

Haneda, H. and Monty, C. (1989). Oxygen self-diffusion in magnesium- or titanium-doped alumina single crystals. *J. Am. Ceram. Soc.*, **72**(7), 1153–57.

Haubensak, F. and Argon, A. (1997). A new method of fracture toughness determination in brittle ceramics by open-crack shape analysis. *Journal of Materials Science*, **32**, 1473–1477.

Head, A., Loretto, M., and Humble, P. (1967). The influence of large elastic anisotropy on the determination of burgers vectors of dislocations in β-brass by electron microscopy. *phys. stat. sol.*, **20**, 505.

Heuer, A. and Lagerlöf, K. (1999). Oxygen self-diffusion in corundum (α-Al_2O_3): a conundrum. *Philosophical Magazine Letters*, **79**, 619.

Hirth, J. and Lothe, J. (1968). *Theory of Dislocations*. McGraw-Hill, Inc., New York.

Kronberg, M. (1957). Plastic deformation of single crystals of sapphire: basal slip and twinning. *Acta metall.*, **5**, 507.

Lagerlöf, K. and Grimes, R. (1998). The defect chemistry of sapphire (α-Al_2O_3). *Acta mater.*, **46**(16), 5689–5700.

Lagerlöf, K., Mitchell, T. E., and Heuer, A. H. (1989). Lattice diffusion kinetics in undoped and impurity-doped sapphire (α-Al_2O_3): a dislocation loop annealing study. *J. Am. Ceram. Soc.*, **72**(11), 2159–2171.

Lev, L. and Argon, A. (1995). Oxide-fiber/oxide-matrix composites. *Mater. Sci. Engrg.*, **A195**, 251–261.

Levi, G. and Kaplan, W. (2003). Aluminium-alumina interface morphology and thermodynamics from dewetting experiments. *Acta. meter.*, **51**, 2793–2802.

Li, J. (1963). Petch relation and grain boundary sources. *Transaction of the Metallurgical Society of AIME*, **227**, 239.

Li, J. (1968). Kinetics and dynamics in dislocation plasticity. In A. Rosenfield, G. Hahn, J. A. Bement, and R. Jaffee, editors, *Dislocation Dynamics*, pages 87–116. McGraw-Hill, New York.

Lim, L. and Muchtar, A. (2002). Micro- and macro-indentation fracture toughness of alumina. *J. Mater. Sci. Lett.*, **21**, 1145–1147.

Lude, T. (2001). Indentation crack profiles in silicon nitride. *Journal of European Ceramic Society*, **21**, 211–218.

Mazerolles, L., Michel, D., and Portier, R. (1986). Interfaces in oriented $Al_2O_3/ZrO_2(Y_2O_3)$ eutecitcs. *J. Amer. Ceram. Soc.*, **69**, 252–255.

Messerschmidt, U., Baufeld, B., and Baither, D. (1998). Plastic deformation of cubic zirconia single crystals. *Key-Engineering Materials*, **153-154**, 143–182.

Michel, D., Mazerolles, L., Dallas, J., Stucky, M., and Portier, R. (1984). Oriented eutectic Al_2O_3-$ZrO_2(Y_2O_3)$ obtained from directional solidification. In P. Lacombe, editor, *Physical Chemistry of the Solid State: Application to Metals and their Compounds.*

Morgan, P.-E.-D. and Marshall, D. (1995). Ceramic composites of monazite and alumina. *J. Amer. Ceram. Soc.*, **78**, 1553–1563.

Mukhopadhyay, A., Datta, S., and Chakraborty, D. (1999). Fracture toughness of structrual ceramics. *Ceramics International*, **25**(2), 447–454.

Nabarro, F. (1967). Steady state diffusional creep. *Phil. Mag.*, **16**, 231–238.

Niihara, K., Morena, R., and Hasselman, D. (1982). Evaluation of K_{Ic} of brittle solids by the indentation method with low crack-to-indent ratios. *J. Mater. Sci. Lett.*, **1**, 13.

Oishi, Y. and Kingery, W. (1960). Self-diffusion of oxygen in single crystal and polycrystalline aluminum oxide. *J. Chem. Phys.*, **33**, 480–486.

Paladino, A. and Coble, R. (1963). Effect of grain boundaries on diffusion-controlled processes in aluminum oxide. *J. Am. Ceram. Soc.*, **46**(3), 133–136.

Pastor, J., Poza, P., Llorca, J., Pena, J., Merino, R., and Orera, V. (2001). Mechanical properties of directionally solidified $Al_2O_3/ZrO_2(Y_2O_3)$ eutectics. *Mater. Sci. Engrg.*, **A308**, 241–249.

Pollock, T. (1990). *Creep deformation in nickel base superalloy single crystals.* Ph.D. thesis, MIT.

Pollock, T. and Argon, A. (1994). Directional coarsening in nickle-base singel crsytals with high volume fractions of coherent precipitates. *Acta metall. mater.*, **42**(6), 1859–1874.

Pollock, T. M. and Argon, A. S. (1992). Creep resistance of CMSX-3 nickel base superalloy single crystals. *Acta Metall.*, **40**, 1–30.

Price, P. (1960). Pyramidal glide and the formation of dislocation loops in nearly perfect zinc crystals. *Phil. Mag.*, **5**, 873–886.

Quinn, J. B. and Lloyd, I. K. (2000). Comparison of methods to determine the fracture toughness of three glass-ceramics at elevated temperatures. *J. Am. Ceram. Soc.*, **83**(12), 3070–76.

Reddy, K. and Cooper, A. (1982). Oxygen diffusion in sapphire. *J. Am. Ceram. Soc.*, **65**(12), 634–638.

Sakai, M. and Bradt, R. (1993). Fracture toughness testing of brittle materials. *International Materials Reviews*, **38**(2), 53–78.

Sayir, A. (1998). Directional solidification of eutectic ceramics. *unpublished report: NASA Glenn Research Center.*

Sayir, A. and Farmer, S. (2000). The effect of microstructure on mechanical properties of directionally solidified $Al_2O_3/ZrO_2(Y_2O_3)$ eutectic. *Acta Mater.*, **48**, 4691–4697.

Snow, J. and Heuer, A. (1973). Slip systems in Al_2O_3. *J. Amer. Ceram. Soc.*, **56**, 153–157.

Socrate, S. and Parks, D. (1993). Numerical determination of the elastic driving force for diractional coarsening in Ni-superalloys. *Acta metall. mater.*, **41**(7), 2185–2209.

Suresh, S. (1998). *Fatigue of Materials.* Cambridge University Press, Cambridge, UK.

Wang, C., Cargill, G., Chan, H., and Harmer, M. (2000). Structure of Y and Zr segregated grain boundaries in alumina. *Interface Science*, **8**, 243–255.

Williams, D. and Carter, C. (1996). *Transmission Electron Microscopy: A Textbook for Materials Science.* Plenum Press, New York.

Wolfenden, A. (1997). Measurement and analysis of elastic and anelastic properties of alumina and silicon carbide. *J. Mater. Sci.*, **32**, 2275–2282.

Yi, J. and Argon, A. (2004). Fracture toughness of directionally solidified eutectic ceramics: Al_2O_3/c-$ZrO_2(Y_2O_3)$. to be published.

Yi, J., Argon, A., and Sayir, A. (2004a). Creep resistance of the directionally solidified ceramic eutecitc of Al_2O_3/c-$ZrO_2(Y_2O_3)$. In *Mat. Res. Soc. Symp. Proc.*, volume 791, page 221. Materials Research Society.

Yi, J., Argon, A., and Sayir, A. (2004b). Creep resistance of the directionaly solidified ceramic eutectic of Al_2O_3/c-$ZrO_2(Y_2O_3)$: experiments and models. *J. European Ceram. Soc.* in the press.

Yi, J., Argon, A., and Sayir, A. (2004c). Internal stresses and the creep resistance of the directionally solidified ceramic eutectics. *Materials Science and Engineering.* submitted for publication.